Design of a Wind Tunnel Force Balance

João Tiago Pinheiro Fernandes

Thesis to obtain the Master of Science Degree in

Aerospace Engineering

Supervisor: Prof. André Calado Marta

Examination Committee

Chairperson: Prof. Filipe Szolnoky Ramos Pinto Cunha
Supervisor: Prof. André Calado Marta
Member of the Committee: Prof. João Manuel Gonçalves de Sousa Oliveira

June 2018

Dedicated to my family and friends.

Acknowledgments

Firstly, I would like to thank to my supervisor, Professor André Marta, for the wise guidance and patience during the last months, even when things seemed to fail to go as planned.

This thesis is the milestone of a period of hard-work and dedication that started a few years ago. Throughout this path, I've met extraordinary people without whom this trajectory would not have been as bright as it was. I would like to thank to my friends Marta for all the support and advices and Rute for the working spot and all the helpful writing tips, with whom I share the adventures of working in a demanding master thesis.

I also want to express my gratitude to my special friends Cláudia and Rita for the coffee breaks and for the moments of laughter and joy that kept me prepared for another round of intensive work.

All this work would not have have been possible without the unconditional support of my loving family. Especially to my mother, for being truly understanding and for showing support in the moments when I needed it the most, to my father that supported my work with his technical expertise and for always having a solution and to my brother and grandparents for the love and care.

Resumo

Os túneis aerodinâmicos são usados para simular o comportamento de modelos na presença de um escoamento, permitindo obter as componentes que melhor definem essa interação, as forças e os momentos. Para tomar total partido do túnel aerodinâmico presente no Laboratório de Engenharia Aeroespacial do Instituto Superior Técnico, revelou-se necessário projetar uma balança de forças e momentos.

Em primeiro lugar, o dimensionamento da balança baseou-se-se na possibilidade de realização de testes em modelos de aeronaves e de meia asa montados na secção de teste, recorrendo a um *software* de simulação (XFLR5) que permitiu obter a gama máxima de carregamento a que a balança estará sujeita para cada uma das hipóteses.

O modelo da balança foi selecionado utilizando um conjunto de critérios comparativos e recorrendo ao Processo Hierárquico Analítico que permitiu definir, de entre as arquitecturas de balanças de forças mais comuns, a que se revelou mais adequada (balança externa em plataforma). Uma vez definido o modelo que constitui o "esqueleto" da balança de forças, foi necessário projetar, criteriosamente, cada um dos seus componentes mecânicos e verificar a sua integridade, através do uso do *software* de modelação *SolidWorks*. Seguiu-se a seleção de todos os componentes eletrónicos como os extensómetros e o sistema de aquisição de dados que permitirão averiguar a deformação da balança causada por um dado carregamento. Foram feitas, ainda, algumas considerações acerca do processo de montagem e foi apresentado o custo total estimado da balança de forças. Por fim, sugere-se um procedimento de calibração que permite tornar a balança operacional.

Palavras-chave: Balança aerodinâmica de seis componentes, Ensaios experimentais, Projeto mecânico, Sensores e instrumentação, Procedimento de calibração

Abstract

Wind tunnels are used to simulate the behaviour of models in the presence of an airflow thus allowing to obtain the components that better define this interaction, forces and moments. In order to take full advantage of the Aerospace Engineering Laboratory's wind tunnel at Instituto Superior Técnico, it has proved necessary to design a balance to measure forces and moments.

Firstly, the force balance dimensioning was based in the possibility of testing both aircraft and half-wing models that fit the wind tunnel test section, using a simulation software (*XFLR5*) to obtain the maximum load range the force balance has to be able to support in each of the situations.

The Analytic Hierarchy Process and a set of comparison criteria allowed the selection of the most adequate force balance architecture from the most widely used, the external platform balance. Once the "skeleton" of the force balance was defined, it was necessary to carefully define each of its mechanical components and guarantee that its integrity was fulfilled using the software *SolidWorks*. This is followed by the selection of all the electronic components like strain gauges and data acquisition system that will assess the deformation of the balance for a certain loading condition. Several considerations on the mechanical assembly were made and a cost analysis was presented. Finally, it is suggested a calibration procedure to make the force balance fully functional.

Keywords: Six components aerodynamic balance, Experimental testing, Mechanical design, Sensors and instrumentation, Calibration procedure

Contents

List of Tables

List of Figures

Nomenclature

Greek symbols

α	Angle of attack; *Stewart* platform parameter.
β	Angle of side-slip; *Stewart* platform parameter.
ϵ	Strain.
λ	Quality Index.
μ	Dynamic viscosity.
ρ	Density.
σ_Y	Yield strength.

Roman symbols

AR	Aspect ratio.
b	Span.
c	Chord.
C_D	Coefficient of drag.
C_F	Force coefficient.
C_L	Coefficient of lift.
C_M	Coefficient of moment.
I	Current.
J	Jacobian matrix.
k	Strain gauge sensibility.
R	Air constant; Strain gauge resistance.
Re	*Reynolds* number.
T	Temperature.

U	Voltage.
X_w, Y_w, Z_w	Wind axis components.
p	Static pressure.
p_0	Stagnation pressure.
V	Airflow velocity.

Subscripts

x, y, z	Cartesian components.

Superscripts

T	Transpose.

Glossary

AHP	Analytic Hierarchy Process
CAD	Computer Aided Design
CFD	Computational Fluid Dynamics
CNC	Computer Numerical Control
DAQ	Data Acquisition System
DLR	*Das Deutsche Zentrum für Luft- und Raumfahrt*
EDM	Electrical Discharge Milling
IMU	Inertial Measurement Unit
ISAE	*Institut Supérieur de l'Aéronautique et de l'Espace*
MAV	Micro Air Vehicle
MRC	Moment Reference Centre
NACA	National Advisory Committee for Aeronautics
SAE	Society of Automotive Engineers
SSL	Standard Sea Level

Chapter 1

Introduction

1.1 Motivation

The market demand in the aeronautical industry has driven its continuous development during the last decades. This fact is due not only to the increasing needs of the society but is also made possible because of the development of science and technology that we have assisted in the past decades.

In the aerodynamics field, in particular, the existing theory along with better experimental conditions allowed a better understanding of the aeronautical specifications and made more efficient and high-performing aircrafts possible. Among the many tools available to fulfil those purposes, the one we will be analysing through this document is the wind tunnel.

Wind tunnel testing is one of the most important experimental tests to assess the aerodynamic performance of different parts not only in aircraft but also in rockets, cars or even in buildings. By subjecting the model in test to an airflow, we can determine forces and torques acting along the structure. It is also important to note that, usually, because of the available dimensions of the wind tunnel test sections, it is used a model that is smaller than the original one.

Since this is a topic of interest, any possible development or advantage will be very welcomed. For this reason, it will be carried out a full analysis of wind tunnel testing mainly regarding the devices used to measure forces and torques: the force balances. In general terms, this device can present several configurations depending on its purpose.

We will be addressing this last topic and designing a force balance to be used in the Aerospace Engineering Laboratory's wind tunnel and so, detailing the theoretical background as well as the chosen approach to do so.

1.2 The Role of Experimental Aerodynamic Testing

With the development of CFD (Computational Fluid Dynamics), some decades ago a few scientists have said that experimental testing would not be needed in a near future because everything could be explained using CFD. However, as time went by, it was possible to notice that CFD was not a replacement of experimental testing but, instead, they can complement each other, as shown in figure 1.1 [1].

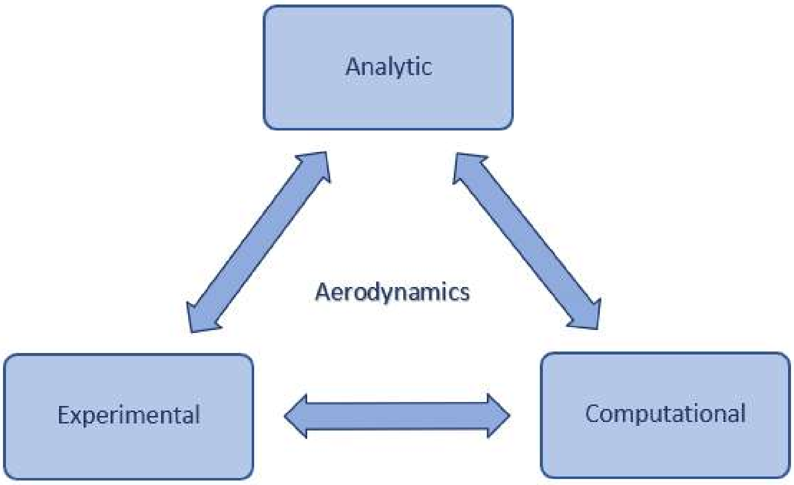

Figure 1.1: Aerodynamic analysis models

In fact, aerodynamic experimental testing is carried out in many fields from aeronautics to construction and wind tunnels along with measuring devices play a crucial role in doing so. The need for this kind of tests is explained based on the fact that, first, theoretical and computational methods are not sufficient to assess all the results needed to perform rigorous aerodynamic analysis and, second, because of their use in practical aerodynamic problems. They are also widely used because they provide a fast and economical way to perform aerodynamic research and obtain results to support design decisions [1].

We can state some examples of experimental tests performed using wind tunnels and evaluate their necessity. Specifically, when it comes to aircraft design, there are several applications for wind tunnels as they can be used to assess and predict aerodynamic parameters such as lift and drag coefficients or pitch, roll and yaw moments. Moreover, wind tunnel experiments can be used to improve aircrafts performance, reduce fuel consumption and emissions and achieve greater acceleration and speed. Figure 1.2 shows a wind tunnel set-up to measure both lift and drag of the scaled wing using an external force balance. This specific experiment is supposed to test the use of multi-tip corona actuators in the wing and analyse their stall delay capabilities. These devices ionize air molecules that accelerate in the process, transferring torque to neutral air molecules and thus energizing the boundary layer [2].

Figure 1.3 represents an experimental setup of a tilt-body *Micro Air Vehicle* (MAV) developed by the *Institut Supérieur de l'Aéronautique et de l'Espace* (ISAE), in Toulouse. This specific model, the *MAVion*, is supposed to fly in both hover (stationary) and forward flight. The experiment was supposed to assess the use of passive twist control as an adaptive way to maximize the overall efficiency of a proprotor developed for this specific type of air vehicles [3].

As for figure 1.4, it represents a model of the DLR F-19 being tested at the *Low Speed Wind Tunnel Braunschweig* (DNW-NWB) that is located at the DLR (*Das Deutsche Zentrum für Luft- und Raumfahrt*) site in Germany. In this specific case, the influence of the use of control surfaces at the trailing edge on the aircraft behaviour (namely pitch and roll moments) is being evaluated at different pitch angles for a

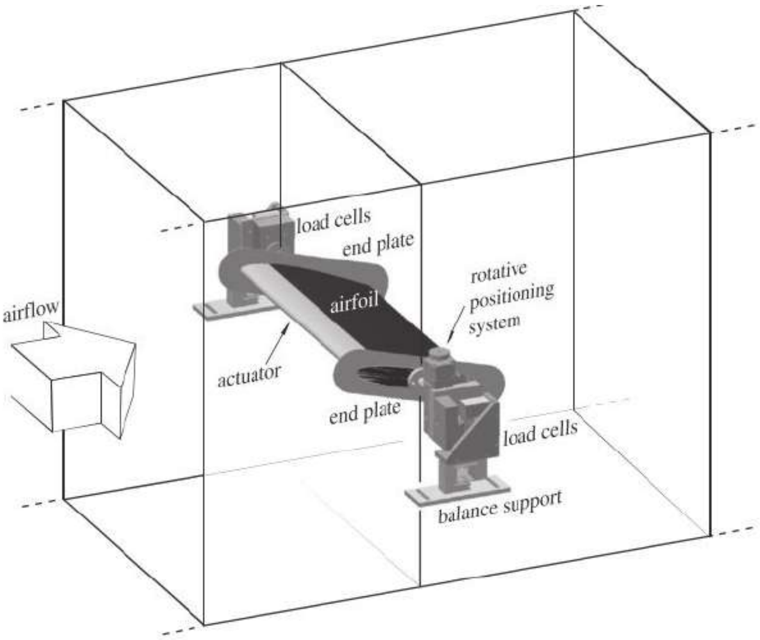

Figure 1.2: Schematic representation of the airfoil experimental set-up [2]

Figure 1.3: Wind tunnel model of MAVion [3]

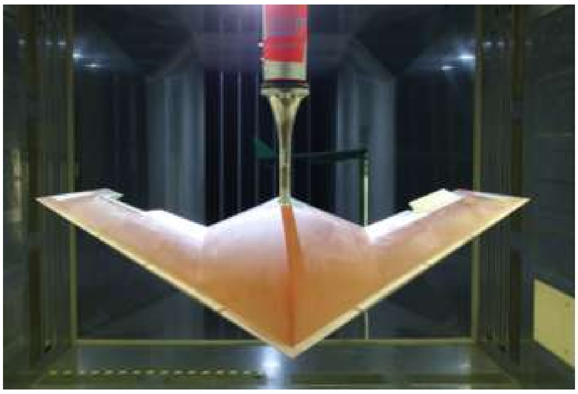

Figure 1.4: Wind tunnel model of the DLR-F19 [4]

certain aileron deflection. The experimental results were used to validate the computational simulations and to analyse the flow physics. The main purpose was to assess the differences between the model with and without control devices [4].

Regarding the automotive field and similarly to what happens in the aircraft field, several studies can be carried out to quantify aerodynamic loads acting on vehicles and be used to improve their shape and thus obtain better fuel efficiency and performance. Moreover, several aspects like comfort and visibility can be improved by, for instance, reducing wind noise and studying splash and spray effects on windows, respectively [5].

Figure 1.5 represents an academic experimental set-up of a Formula SAE (Society of Automotive Engineers) vehicle. This simplified model is a 25% scale of the real car and the purpose of the experience was to evaluate the influence of different design options in the performance of the vehicle. In this specific case, the differences were the use of a planar or diffused floor and the use of wings [5].

Wind tunnels play an important role, not only in the aeronautical and automotive field but also in civil

Figure 1.5: Experimental set-up of a scaled Formula SAE car [5]

engineering. For instance, it is possible to use wind tunnel tests to study the aerodynamic boundary layer, analysing its velocity and turbulence in complex terrains, in order to install wind turbines. In fact, both field and wind tunnel experiments play an essential role when it comes to study wind turbines behaviour in the atmosphere. To do so, it is necessary to build the scaled 3D model of the place where the wind turbines are to be installed and simulate its roughness [6]. An example of this kind of test is shown in figure 1.6.

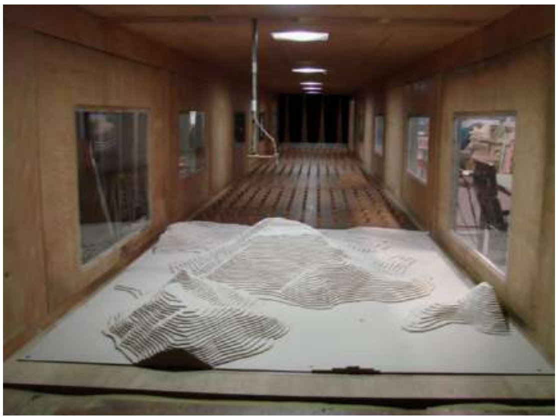

Figure 1.6: Realistic scaled model of the terrain for wind tunnel testing at Construction Aerodynamic Laboratory, Brazil [6]

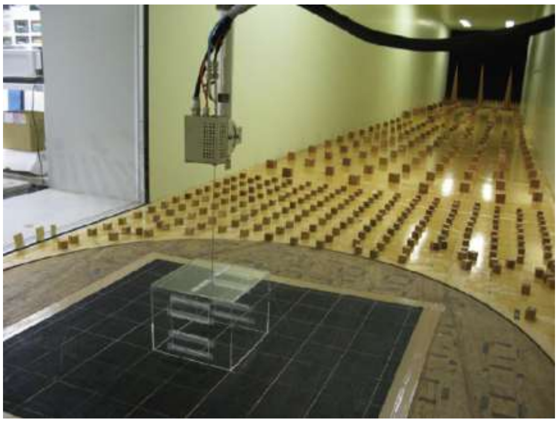

Figure 1.7: Wind tunnel set-up for concentration and velocity measurements (Niigata Institute of Technology) [7]

Wind tunnel testing is also frequently used alongside with CFD analysis as the former consists in a validation for the latter. In fact, it is usual to confirm both accuracy and reliability of CFD simulations by performing experimental tests, for example, using wind tunnels. Figure 1.7 represents the wind tunnel set-up of a model tested to validate CFD results. Particularly, a set of blocks (representing buildings), opened on two sides was carefully placed in the tunnel. Each block was submitted to a certain concentration of a traced gas and the purpose of the experiment was to assess the cross-ventilation effect (by analysing the traced gas concentration and flow velocity) and compare it with CFD predictions.[7]

1.3 Objectives and Deliverables

As referred in the previous section, it is a given fact that experimental testing plays an important role when it comes to study aerodynamics and, as seen, this study is performed in several domains of interest, not only to assess aircrafts aerodynamic performance but also, for instance, to evaluate building stability or meteorological phenomena. Given so, wind tunnel testing is of significant importance as it represents the main driver on performing this kind of analysis and is extensively used. For these reasons, any improvements in this area will have a great impact. Because of this fact, many different solutions have been accomplished during the last few years in order to answer to these challenges, resulting in more efficient wind tunnels and more advanced measuring solutions. The solution of the wind tunnel force balance arises from these needs.

The purpose of this thesis is to design a force balance to be installed in the Aerospace Engineering Laboratory's wind tunnel.

This force balance has to measure six components of aerodynamic forces (drag, lift and side) and moments (pitching, rolling and yawing) and it is supposed to be fully adapted to our measuring reality. It is, for this reason, necessary to conduct a full analysis regarding not only the solutions already available along with our measuring objectives but also the new possible developments that can bring some value and innovation to this project. First of all, it is necessary to identify the measuring requirements of the force balance in order to select the most adequate concept. After that, its mechanical and electrical design has to be performed that will result in a set of components that have to be design and purchased. Finally, this set of components will result in a manufacturing and assembly plan that has to be followed. After that, a possible calibration process for the force balance will also be outlined.

Given this, the project deliverables of this project are the following:

- to come up with detailed design of the force balance to be installed in the Aerospace Engineering Laboratory's wind tunnel at Instituto Superior Técnico;

- to obtain a list of all the parts needed, being them off-the-shelf components or made to specification parts;

- to present a manufacturing and assembly plan;

- to present a calibration plan.

1.4 Thesis Outline

This thesis is structured as follows:

Chapter 2 State of The Art describes the devices used in experimental testing, like wind tunnels, force balances and necessary sensors and systems of data acquisition;

Chapter 3 Requirements and Conceptual Analysis presents an analysis to define the requirements of the force balance in terms of loads and maximum displacement. A conceptual study is also carried out to determine the basic shape of the structure;

Chapter 4 Mechanical Design shows the properties of each of the mechanical components of the force balance supported by the results of finite element simulations;

Chapter 5 Sensors and Instrumentation defines the set of electronic devices necessary to obtain the results of the force balance;

Chapter 6 Manufacturing, Cost and Assembly presents a set of details about the manufacturing process and selection of mechanical components as well as essential aspects concerning the assembling process. A cost analysis of the whole force balance is also conducted;

Chapter 7 Calibration presents a calibration methodology to guarantee that the force balance can present the real values of forces and torques;

Chapter 8 Conclusions presents the overall points that were fulfilled and suggests some improvements to the force balance itself and to the user experience.

Chapter 2

State of The Art

2.1 Wind Tunnels

In general terms, we can divide all types of wind tunnels in two major groups: open circuit wind tunnels and closed circuit wind tunnels.

Regarding open circuit wind tunnels, the airflow follows a straight path and flows from the entrance to the contracted zone where the test section is located and then passes through a diffuser, a fan section and an exhaust. Regarding the boundaries, that is, the “limit” of the wind tunnel, they may be solid or not.

As the name suggests, closed circuit wind tunnels (also known as closed return, Prandtl or Göttingen wind tunnels) are characterized by the recirculation of the air flow. In fact, the exchange of air with the exterior is very small. This kind of wind tunnel usually has a single return, meaning that the air flows through one specific path. Like the ones stated before, the test section of these wind tunnels can be open or closed.

We can state some advantages and disadvantages of each configuration however, the decision is made according to the purpose of the wind tunnel and the funds available for its construction [1].

2.1.1 Open Circuit Wind Tunnels

Having succinctly described both types of wind tunnels, we can point out some advantages and disadvantages of each type of configuration.

Starting with the open circuit wind tunnels, represented in figure 2.1, we can highlight its lower construction cost, mainly due to the inherent simplicity in terms of components. Given the fact that both the entrance and the exit are open to the atmosphere, there is no problem to run tests with internal combustion engines or using smoke for flow visualization as purging is not needed.

However, we can point out some disadvantages owing to its simplicity. In the case of open circuit wind tunnels, outer conditions may affect the operation, because it may require considerable protection at the inlet to obtain high quality flow. On the other hand, if opened directly to the atmosphere, the exhausting zone can be widely affected by changes of temperature or wind phenomena. This kind of wind

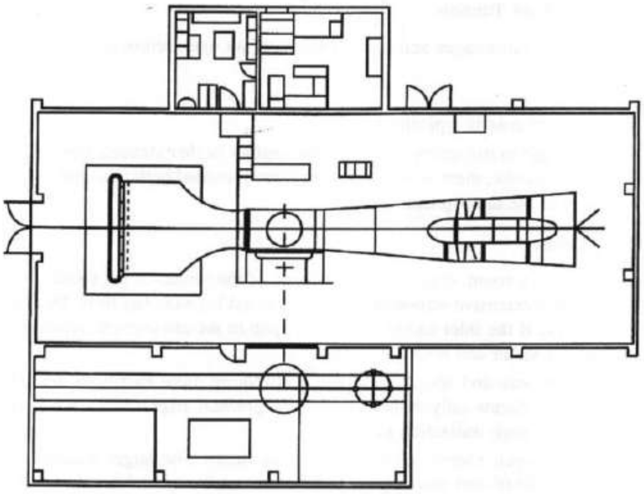

Figure 2.1: Open circuit wind tunnel of Diamler-Benz Aerospace Airbus [1]

tunnel is also associated with higher operation costs since the fan has to be continuously accelerating flow through the tunnel. They tend to be noisier when compared to the closed ones: this fact forced the implementation of legislation to limit the time of operation, protecting human beings and avoiding environmental problems.

Due to its lower construction cost, this kind of wind tunnel is suited for schools or universities, for academic purposes [1].

2.1.2 Closed Circuit Wind Tunnels

Analogously, it is possible to infer the main advantages and disadvantages of this type of wind tunnel.

Since the model is closed, it is possible to control the parameters of the flow and hence its quality which is, in this case, independent of meteorological conditions or other activities taking place in the vicinity of the tunnel that could affect the environment around it. At the same time, and unlike the open circuit wind tunnels, for some given dimensions, this type of tunnel requires less energy to operate since the airflow recirculates in the tunnel and the fan needs only to overcome eventual losses along the tunnel and turning vanes. It is also quitter when compared to the open wind tunnel. A schematic representation of this kind of wind tunnel is shown in figure 2.2.

Regarding its disadvantages, a closed circuit wind tunnel presents high initial costs due to its complexity, namely the return ducts and the corner vanes. The use of internal combustion engines or smoke for flow visualization forces the existence of a purging mechanism to expel products that otherwise would accumulate inside the tunnel. It might also be required to have a cooling device to reduce the temperature inside the tunnel [1].

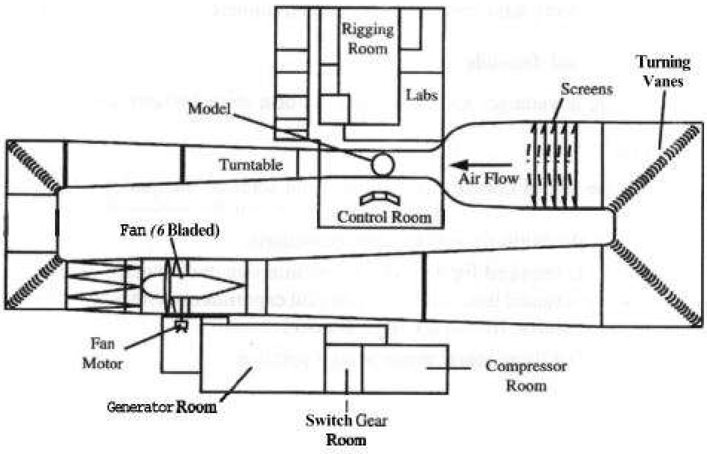

Figure 2.2: Closed circuit wind tunnel of Defense Establishment Research Agency (DERA) [1]

2.2 Force Balances

In a simple way, we can say that a force balance is a device used to directly measure forces and torques acting on the model that is being tested in the wind tunnel. Desirably, a good force balance should be able to provide separated values of force and torque components. Additionally, we can say that any force balance rises from the necessity of having maximum load capability in all measuring components along with the accuracy for measuring minimum loads [1].

The are some aspects in the development of a wind tunnel force balance that need to be taken into account and can be seen as requirements. First of all, the range of the balance must be chosen to match the conditions of the tests to be performed. Secondly, its geometrical properties have to be adequate to fit in the test section of the wind tunnel [8].

A model to be tested can be mounted by struts to the balance which lays outside the wind tunnel test section, in this case we have an external wind tunnel force balance. On the other hand, we can have the balance inside the model itself connecting the model to the support structure, in this case we have an internal force balance [1]. Both configurations present advantages and disadvantages and their suitability depends mainly on the model to be tested and the wind tunnel to be used.

Besides the structure of the force balance itself, there are several systems that are necessary to obtain the desired results. Coupled to the frame of the force balance, there are extensometers that will measure the strain of the loaded structure. The output voltage of these sensors is then post-processed in a data acquisition system which is associated with a specific software that will return the correspondent strain values. After a previous and careful calibration process that concludes the construction of the force balance, it is possible to come up with the loading state of the model, in terms of force and torque components, based on the obtained values of strain. The schematic represented in figure 2.3 explains the overall process. A detailed explanation on the referred components will be carried out in the next sections.

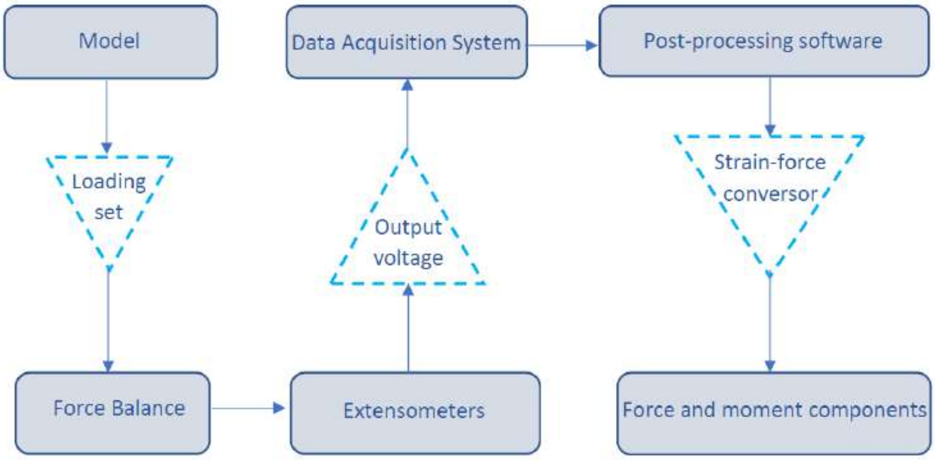

Figure 2.3: Schematic representation of data acquisition procedure using a force balance

2.2.1 External Configuration

Regarding external force balances, we can highlight four types whose designation depends on the main load-carrying members: wire, platform, yoke and pyramidal [1].

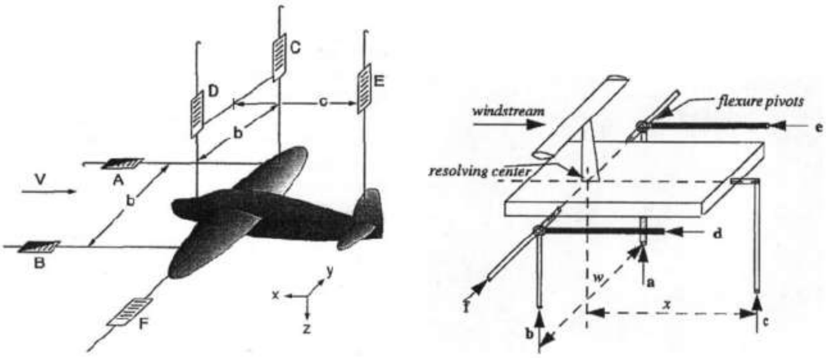

(a) Wire (b) Platform

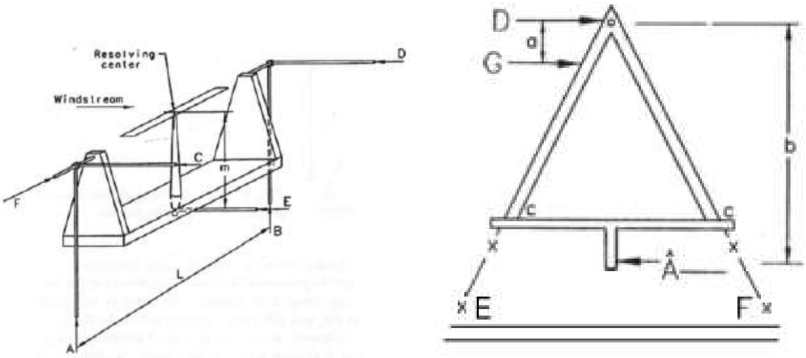

(c) Yoke (d) Pyramidal

Figure 2.4: Typical configurations for external force balances

In the wire balance, the model is suspended by wires, each of them connected to extensometers. The main problem concerning the wire balance is the large tare drag caused by the wires, difficult to quantify. These balances are not used nowadays since they are not robust nor versatile enough compared with the available alternatives [1].

Regarding the remaining types of external force balances (platform, yoke and pyramidal), they allow a strut-mounting of the model to be tested and are distinguished based in the way they are assembled.

Platform balances are relatively easy to construct and assemble as well as instrument however the main problem lies on the fact that forces and torques are coupled and the balance resolving center does not coincide with the center of the tunnel. This last issue was resolved with the yoke configuration. However, this type of force balance presents some structural deflections given the large span of the measuring and supporting arms.

To overcome the problems of the presented configurations, it was constructed a new type of external force measuring device: the pyramidal balance. It is capable of measuring six components of forces and torques separately and without coupling. However, to provide this sort of capabilities, the assembly of the balance has to be carefully performed as well as the calibration since a small deflection can greatly affect the measured values of forces and torques.

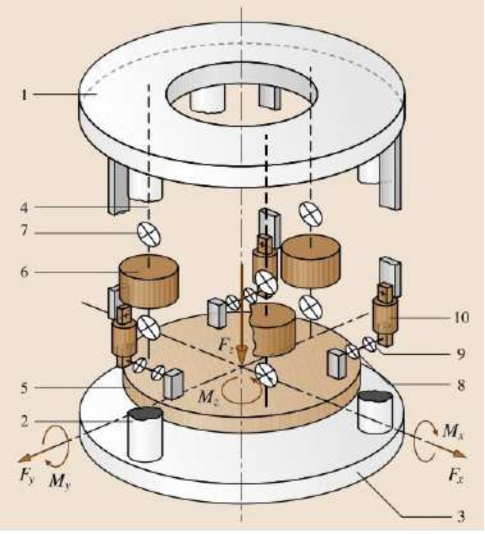

Figure 2.5: Typical configuration of a platform force balance [9]

Figure 2.5 schematically represents a typical configuration of an external platform force balance. The nonmetric part of the balance consists of the numbers 1, 2 and 3, represented in white, that form the main frame. The metric part is the weighbridge represented by number 5. It is connected to the load cells (6 and 10) by rods (4 and 8). Numbers 7 and 9 represent flexible knuckles that avoid unwanted torques on load cells [9].

2.2.2 Internal Configuration

When it comes to internal force balances, while the main purpose of this device is also to measure forces and torques acting on the model, the balance has to perform its task with very specific requirements in terms of shape and volume.

The distinction between the different kinds of internal balances can be made based on the type of transducer: strain gauges or piezoelectric element. Since the first type is the most common, the designation for this type of balance can also be internal strain gauge balance.

Regarding the shape, we can divide internal force balances in two types: box balances and sting balances. The former presents a cubic shape and the loads are transferred from the top to the bottom, as represented in figure 2.6(a). It can either be constructed from a solid piece of material or assembled parts.

The latter, shown in figure 2.6(b), presents a cylindrical shape and the loads are transferred from one end to the other in the longitudinal direction; it can be used to measure forces or torques.

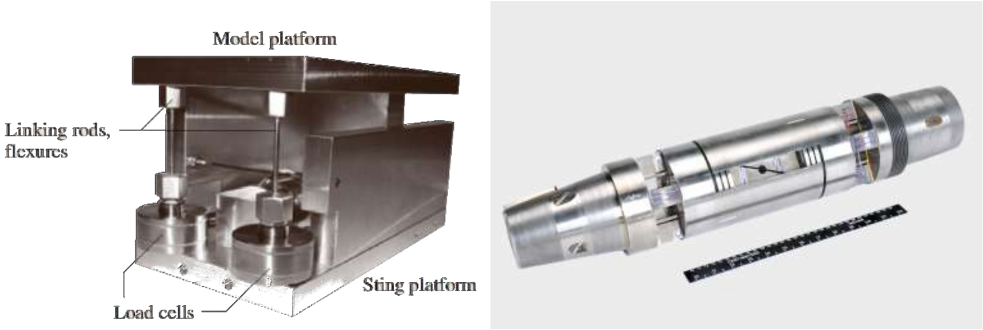

(a) Box [9]

(b) Sting

Figure 2.6: Typical internal force balance types

Nowadays, these balances are constructed using EDM (Electrical Discharge Milling) which allows them to be made out of just one piece of material; this is very important since eliminates hysteresis effect and eventual misalignments [1].

One of the advantages of the internal force balances is that they are able to minimize the interference caused by the supporting bars in the flow [10].

2.3 Sensors and Data Acquisition Systems

Besides the main structure of the force balance, several devices have to be connected in order to measure and obtain the results and so making it fully operational.

One important factor regarding wind tunnel testing is the way forces and torques are measured. There are several methods available in the market that we can apply to a force balance, however there are advantages and disadvantages that lead to a choice that will be dependent on the force balance to be used.

Another important quantity that has to be monitored is the air stream velocity. There are many techniques to measure it, although some are more adequate and present more advantages than the others, regarding this specific application.

Finally, in order to control the position of the models that are going to be tested, it is necessary to use devices that provide the attitude, since the forces and torques acting on the object are greatly dependent on its orientation.

2.3.1 Load Sensors

There are several ways to measure forces and torques in a force balance but, in general, they can be divided in two major groups: hydraulic measuring devices and electrical measuring devices. The former is a device that measures force values through the pressure exerted on pistons that have a certain known value of area. This pressure is a function of the load and is measured using pressure gauges. As for the latter, there are many options to measure forces and torques electrically, being the most widely used the strain gauges, that can present a wide range of different properties, and piezoelectric force transducers. Usually, in force balances applications, the electric load measurement techniques are preferred.

A strain gauge is an electromechanical device which electrical resistance changes are directly related with the strain in the component and the most basic is the wire strain gauge. This wire is typically very thin (around $20\,\mu m$ to $30\,\mu m$ in diameter) ans is bonded to a substrate.

More recently, this type of strain gauges has been replaced by foil strain gauges, shown in figure 2.7, and basically the main difference is that there is a metal foil pattern ($2\,\mu m$ to $5\,\mu m$ thick) bonded to an insulating backing sheet ($10\,\mu m$ to $30\,\mu m$ thick) using a construction technique similar to the one used in integrated circuits manufacturing. This type of strain gauge can provide more precise strain values.

In general, we can relate strain gauge resistance with its strain by

$$\frac{dR}{R} = k\varepsilon, \tag{2.1}$$

where ε stands for strain, k for strain gauge sensibility and $\frac{dR}{R}$ for the relative change on the strain gauge resistance.

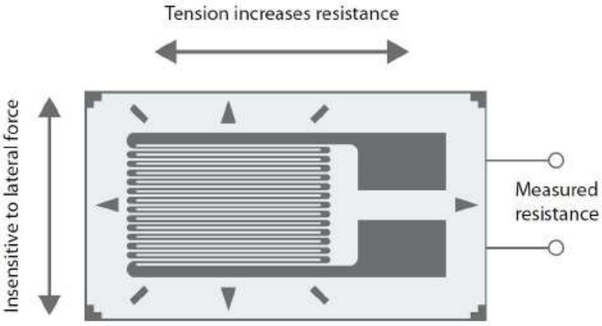

Figure 2.7: Metal-foil strain gauge

It is necessary, however, to consider some important aspects: since the relative changes on electric resistance of the strain gauge are so small it was necessary to develop an effective method to measure them because each strain gauge would require extremely accurate signal measurements. The solution is to have a set of strain gauges coupled in order to minimize the required accuracy, forming a force transducer. The *Wheatstone bridge*, also called full bridge (schematically represented in figure 2.8), consists of two parallel pairs of resistors in series and the output of the bridge relates all values of resistance keeping in mind that one of the pairs is in compression and the other in tension. For instance, in figure 2.8, when resistors R_1 and R_3 are in tension, resistors R_2 and R_4 are in compression, and vice versa. In this case we can adopt the relation

$$\frac{U}{U_e} = \frac{1}{4}\left(\frac{\Delta R_1}{R_1} - \frac{\Delta R_2}{R_2} + \frac{\Delta R_3}{R_3} - \frac{\Delta R_4}{R_4}\right), \tag{2.2}$$

where U represents the output signal, U_e the excitation voltage and $\frac{\Delta R}{R}$ the change on the resistance, as we can see in figure 2.8 [9].

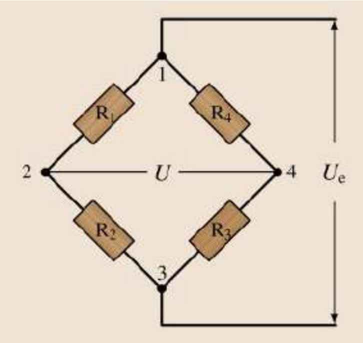

Figure 2.8: *Wheatstone* bridge circuit [9]

Another type of strain gauge can be made by using semiconductors of silicon. In this case, the output is non-linear with strain but mechanically they present attractive features like the absence of creep and hysteresis and have a long fatigue life.

Regarding piezoelectric force transducers, they are formed by crystals (composed of ions) that, when loaded, deform mechanically. This deformation generates electric charges at the surface that result in a polarization of the entire crystal. This effect is represented in figure 2.9. Generally, materials like quartz (SiO_2) or special ceramics are used, provided they have the adequate physical properties.

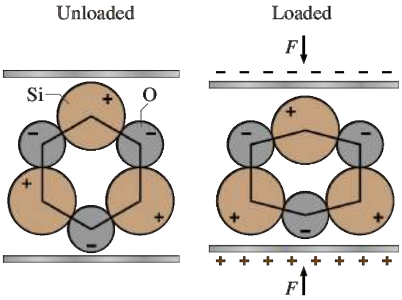

Figure 2.9: Piezoelectric force transducer behaviour [9]

Considering a three-component force transducer, that can be arranged in order to measure the six components of forces and torques, it consists of three stacked quartz rings: two of them are shear sensitive and are aligned to the measurements of both orthogonal components of an arbitrary shear force in a certain direction and the remaining ring senses the pressure and measures the compression on the transducer. A scheme of this type of force transducer is shown in figure 2.10.

To obtain a signal proportional to the applied force, a charge amplifier is used.

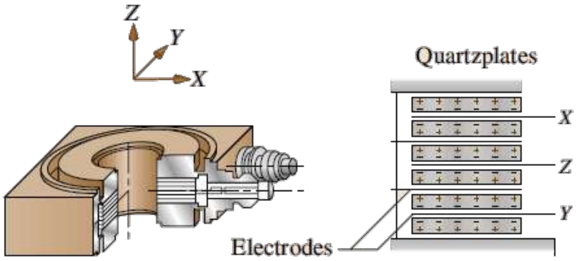

Figure 2.10: Piezoelectric three-component force transducer [9]

2.3.2 Velocity Sensors

In order to monitor the airflow velocity inside the wind tunnel test section, a measuring technique has to be selected. There are many ways to measure the velocity of the air inside the wind tunnel and they can be distinguished in three main groups: thermal anemometry, particle-based techniques and pressure-based measurements [9].

Regarding thermal anemometry, it is used to measure changing velocities with good spatial and time resolution. To do so, a small heated sensor, made of a material whose electric resistivity depends on the temperature, is placed in the fluid in motion being possible to quantify the changes in heat transfer. Considering a steady flow, equating the heating and the cooling rates as

$$R_w I_w^2 = (T_w - T_a)\phi_{conv}(U), \tag{2.3}$$

where R_w is the sensor resistance when heated, I_w is its current, T_w is the temperature of the wire when heated and T_a the temperature of the wire when cooled, it is possible to obtain the airflow velocity.

Considering the particle-based techniques, they can be regarded as optical measurement techniques as the purpose is to visualize the behaviour of certain particles that lie within the airflow. Some tracer or seed particles are placed in the flow, following its velocity fluctuations and providing the spatial and temporal distribution of the flow velocity.

Pressure-based measurement techniques are the most widely used ways of measuring the velocity of a certain airflow. They rely on pressure measurements to obtain the airflow velocities. When it comes to pressure measurements, an important device has to be presented: the Pitot tube. Pitot tubes are devices that are widely used in airflow measurements as they can be used to measure flow pressure and so obtain the air stream velocity. In order to comprehend the working principles of Pitot tubes, it is important to present and clarify some aspects about air flow pressure distribution.

Considering a streamline and assuming that the flow is incompressible so that the air density (ρ) is constant, it is possible to apply Bernoulli's equation as

$$p + \frac{1}{2}\rho V^2 = p_0, \tag{2.4}$$

where p_0 represents the total pressure at a point where the air velocity is 0, the so-called stagnation point, p represents the static pressure that is the pressure at all points in stationary air and the remaining term is the dynamic pressure caused by the moving air stream [11].

Applying this concept to the Pitot tubes is simple: in this case, a streamline is brought to rest, resulting in a stagnation point ($V = 0$), at which a manometer is placed in a small orifice being possible to obtain the total pressure at this point (p_0). Connected to the other extremity of the manometer, there is a static-pressure tube that measures p. The difference between these two quantities results in the dynamic pressure thus being possible to obtain the air stream velocity, as long as the density of the air is known.

The previous relation is only true if the following conditions are fulfilled:

- the tube is as narrow as possible so that only one streamline is stopped;
- the effects of viscosity can be neglected;
- the airflow does not pass through the tube; this is done by connecting the end to the manometer.

In practice, only the last of the items above is achieved. Regarding viscosity effects, they can be neglected except for very small tubes operating at very low speeds that is not the case of the operating conditions often found in practice [12].

A schematic representation of a Pitot tube is shown in figure 2.11 or, more accurately, static-Pitot tube as it measures both static and total pressures. The orifice at A senses the total pressure while the orifice at B senses the static pressure. Conjugating both results, it is possible to obtain the velocity, provided the density is known. This last quantity can be calculated by measuring temperature, static pressure and applying the equation

$$p = \rho RT, \tag{2.5}$$

where p is the static pressure, in Pa, ρ is the density of the air, in kg/m^3, R is the air constant and is equal to $287.06\ Jkg^{-1}K^{-1}$ and T is the air temperature, in K [1].

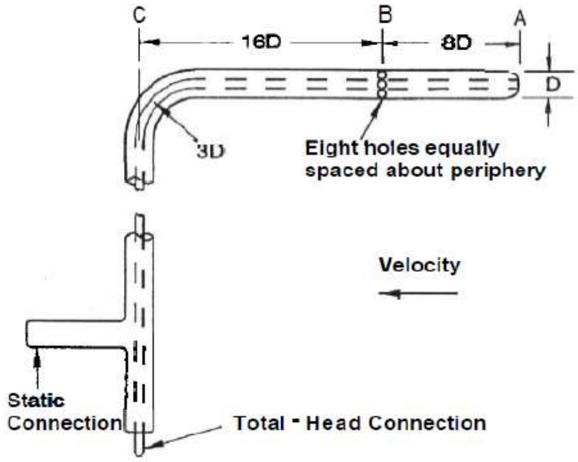

Figure 2.11: Schematic representation of a static-Pitot tube [1]

2.3.3 Attitude Sensors

Another important factor in wind tunnel measurements is related with the position of the objects that are to be tested. Sometimes, we want to test a certain model with a specific angle of sideslip (β) or angle of attack (α).

The first one (β) is the angle between the longitudinal axis of the model and the direction of the flow on the horizontal plane (figure 2.12). As for the angle of attack (α), it is measured between the longitudinal axis of the model and the direction of the flow on a vertical plane (figure 2.13).

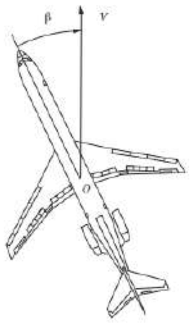

Figure 2.12: Sideslip angle (β) [13]

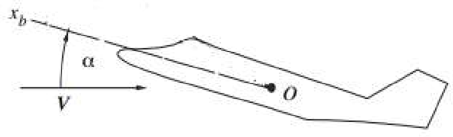

Figure 2.13: Angle of attack (α) [13]

It is important to define the desired aerodynamic angles and to guarantee that they are measured accurately in relation to the air stream, as the components of aerodynamic forces and torques directly depend on the orientation of the model. For this reason, specific devices that provide the attitude should be implemented in order to improve the precision of the results.

Inertial Measurement Units (IMU)

IMU's are sensors that usually combine an accelerometer, a gyroscope and, sometimes, a magnetometer being widely used due to their small size and low cost. The gyroscope is used to measure the sensor's angular velocity and the accelerometer is used to measure the external force acting on the sensor which is not only due to its acceleration but also to the gravity. The gyroscope measurements can provide the change in pitch, roll and yaw by integrating the values of angular velocities along the three axis, but to calculate absolute values of these angles, reference data is needed. This data can be obtained from the accelerometer or the magnetometer. It is possible to obtain pitch and roll angles from the accelerometer, considering the existence of the gravitational acceleration. However, yaw angle cannot be obtained directly from the results of the accelerometer as it is in the same direction as the gravity. For calculating yaw, the data from the magnetometer as reference and then integrates the gyroscope information [14].

Figure 2.14 shows an IMU (MPU 6050) constituted by a 3-axis gyroscope and a 3-axis accelerometer. This type of sensor can be easily connected to an Arduino board that, in turn, is connected to a computer allowing us to easily obtain the measured results. Another advantage of this type of device is its reduced dimensions as it consists of a small and thin electronic plate. The small dimension prevents flow caused

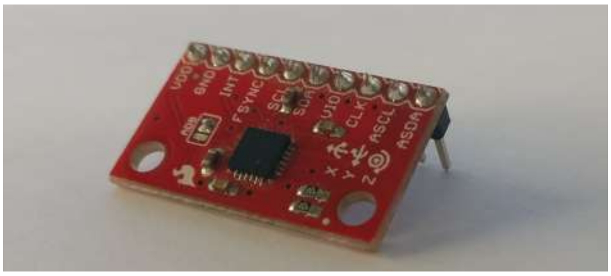

Figure 2.14: Inertial Measurement Unit

interferences in the forces and torques measurement. On the other hand, these sensors are relatively cheap and easy to find.

Digital Measuring Device

Another possibility for measuring the aerodynamic angles is to use specific digital devices, the so-called, digital protractors. The advantage of this type of sensor is that it does not require the use of additional devices to read the data as it immediately displays the values of the angles.

On the other hand, when compared to IMU sensors, these devices are larger and thicker being harder to eliminate its interferences in the loading measurement caused by its interaction with the air stream. Another disadvantage is the lack of versatility as they only measure one angle that corresponds to the inclination of the device.

2.3.4 Data Acquisition Systems (DAQ)

As said previously, extensometers are sensors that produce an electrical output when submitted to a load and deform. However, one is interested in assessing not the correspondent electrical signal due to the variations on the resistors but, instead, the load that is acting on the structure. For this reason, it is necessary to, after having converted the structure deformations to an electrical signal by means of extensometers, decode this signals to obtain the correspondent deformations and forces.

DAQ hardware plays an important role as an interface between a computer, where the results are to be analysed, and the loads that act on the system being tested. This device is fundamental as without it, it would not be possible to interpret the output from the sensors. This happens because the electrical output from the extensometers is an analogical signal while the computer requires a digital input. This leads to conclude that an important component of a DAQ device is, precisely, an analogue-to-digital converter.

Besides this device, we also need a signal conditioning unit that will diminish or cancel the noise from the electrical signal, making it an adequate input to the analogue-to-digital converter referred previously.

The same can be said about the other sensors whose output is also an electrical signal.

Chapter 3

Requirements and Conceptual Analysis

3.1 Wind Tunnel Specifications

The wind tunnel that we will be using to perform our analysis and develop our force balance is the one located in the Aerospace Engineering's Laboratory at Instituto Superior Técnico, that is a closed circuit wind tunnel. This means that it is necessary to adopt the features of the force balance to the specifications of the referred wind tunnel, namely, to the dimension of the test section and flow velocity.

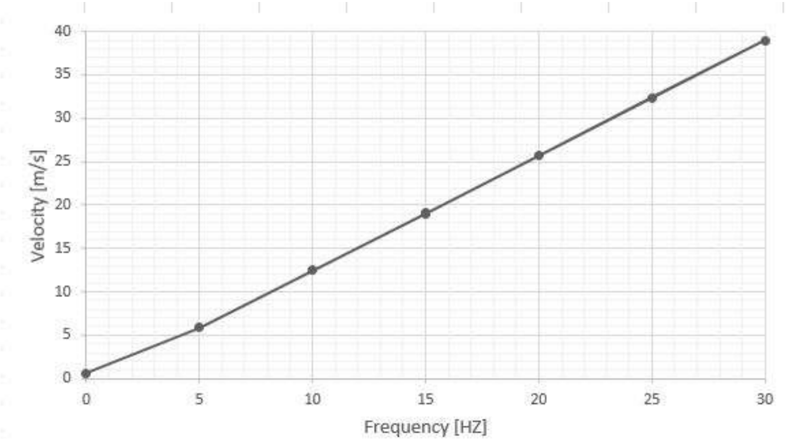

Figure 3.1: Linear relation between inverter frequency and airspeed

We can state a few features that characterize this wind tunnel: it has a maximum airspeed velocity of $40\,m/s$ associated with a frequency of $30\,Hz$ of the fan motor, as seen in figure 3.1, flowing through the test section. The graphic shows a linear relation between the inverter frequency and the airspeed obtained from dynamic pressure both measured during a calibration test.

In order to dimension the force balance, it is important to know the internal dimensions of the wind tunnel, in particular the ones that refer to the test section. A schematic representation of the wall that contains the nozzle is shown in figure 3.2, along with its characteristic dimensions (in centimetres).

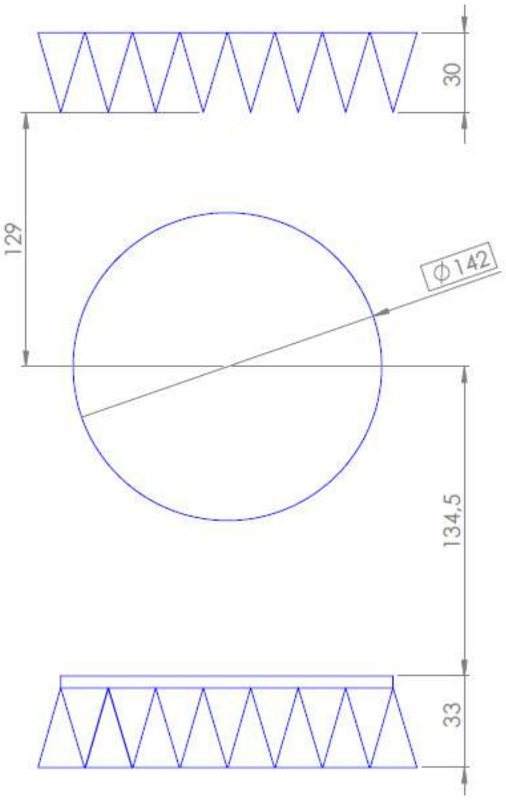

Figure 3.2: Schematic representation of the wind tunnel - internal dimensions of the nozzle section

Given the nozzle dimension and taken into account the growth of the mixing layer of the jet, it is expected a test section with no more than $100\,cm$ of diameter.

The triangle shaped structure at the bottom and the top is part of the anechoic chamber and works as an insulator. Above this structure, at the bottom, and fixed to the ground there is a metallic net that offers support for objects and a path to walk on. This is represented by the rectangle above the triangular structure, in the figure. The nozzle is represented by a circle in the scheme.

3.2 Testing Scenarios

The aim of this project is to develop a six-component force balance to be used in the wind tunnel stated above. This device should be capable of measuring lift, drag and side forces as well as pitching, rolling and yawing moments.

In order to accurately measure all of these components, it is mandatory to define the reference axis on the wind tunnel. There are many groups of reference axis, as they can be defined according to different objects, like the balance itself, the model to be tested or, for instance, the wind direction. It is important, however, to select a reference frame that is independent of the experiment. For this reason, in wind tunnel applications, it is common to define the wind axis as the reference frame. Its origin is fixed at the model moment reference centre (MRC), which coincides with the attachment point of the model to the balance. Figure 3.3 represents the three components of the wind axis in a simplified scheme of the wind tunnel test section and the subscript *w* stands for *wind*. X_w is the wind longitudinal axis which is parallel to the wind tunnel flow but is defined in the opposite direction. Y_w is the wind lateral axis which is perpendicular to the wind x-z plane and positive defined by a right-handed system, being the Z_w the vertical wind axis.

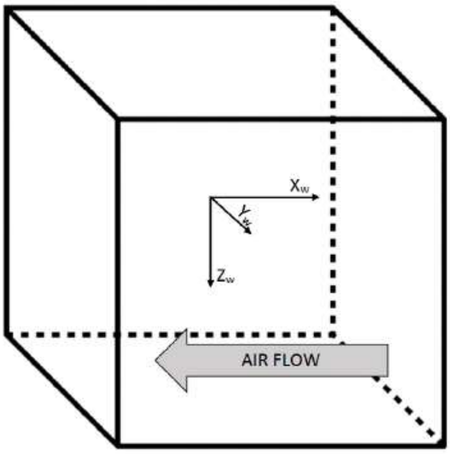

Figure 3.3: Schematic representation of the wind tunnel test section and of the adopted reference axis

If the coordinate system is defined in this way, the aerodynamic components acting on the model are perfectly aligned with the axis and, moreover, each aerodynamic load is positive in the positive direction of each axis. The adopted nomenclature is depicted in table 3.1. The positive directions for M_X, M_Y and M_Z were found using the right-hand rule.

Table 3.1: Matching between aerodynamic loads and correspondent wind axis components

Aerodynamic Force	Designation	Aerodynamic Moment	Designation
Drag	F_X	Rolling	M_X
Side	F_Y	Pitching	M_Y
Lift	F_Z	Yawing	M_Z

There are several types of forces balances to be used in wind tunnels and its suitability depends not only of the type of wind tunnel but also of the tests to be made, as mentioned in section 2.2. We will further conduct a detailed conceptual study on all advantages and disadvantages in order to come up with the best solution for the problem.

In this domain, one of the most important issues is related to the range of loads that are to be measured as the balance has to be designed under these requirements. Since the force balance is to be used for academic purposes, it is hard to predict the type of models to be tested and thus the related range of forces and torques. However, it is possible to describe some hypothetical situations that would correspond to a limit situation.

Based on these predictions, two main options arise when it comes to the models being tested: a) we can study the aerodynamic forces and torques distributions on an isolated wing, in this case, it is common to test half wing models and extrapolate the results to the full wing model; b) another option is to use a complete model of an aircraft with wing, fuselage and stabilizers.

3.2.1 Half Wing Model

Considering the case of a wing, it will be assumed to have a low aspect ratio, calculated as

$$AR = \frac{b^2}{S}, \tag{3.1}$$

, where AR is the aspect ratio, b is the wing span and S is the wing area, since the lower the aspect ratio the more the span approaches the mean aerodynamic chord as one is considering the use of rectangular wings where $S = b \times c$ and c is the chord.

Moreover, it is difficult to conclude which value can be said to correspond to a low aspect ratio but it can be affirmed that an aspect ratio of 4 is a good compromise.

On the other hand, in order to get the maximum lift coefficient in the wing, an airfoil with high camber has to be chosen. This property quantifies the asymmetry between top and bottom sides of the airfoil. Regarding this, a good choice can be the NACA 4412 airfoil, that has a maximum camber of 4% located at 40% from the leading edge and the maximum thickness is 12% of the chord. These physical characteristics are represented, schematically, in figure 3.4 and the NACA 4412 airfoil is depicted in figure 3.5.

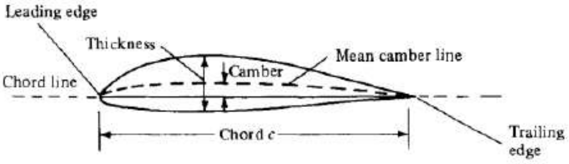

Figure 3.4: Airfoil physical properties

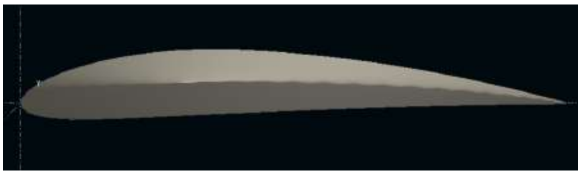

Figure 3.5: *NACA 4412* airfoil

Regarding the dimensions of this wing model and giving the fact that we will be testing half wing models, it is important to guarantee that the maximum length, in this case the half of the wingspan, is shorter than the maximum diameter of the test section. Giving this, we can assume a limit situation of a half-wingspan of $1\,m$. This dimension has to be smaller than the diameter of the test section since one is interested in having a non-disturbed flow far from the influence of the boundary layer.

If we consider the wing to be rectangular, the simpler case, and considering an aspect ratio of 4, the chord was found to be $0.5\,m$.

Having established the main design aspects of the model, the flow velocity must be considered too. In this case, the air stream exits the nozzle with a maximum velocity of around $40\,m/s$, considering the results presented in section 3.1. For the sake of simplicity and to obtain a more critical solution, let us consider a maximum air flow velocity of $50\,m/s$.

Now that the airfoil is selected and the design is defined, it is possible to use a simulation software to estimate aerodynamic loads that will be acting on the model. The range of simulations to be performed gives us the aerodynamic coefficients of the wing model, namely, lift and drag forces and pitching moment coefficients, thus allowing us to obtain an approximate range of aerodynamic forces and torques.

In this case, *XFLR5, v6.40* [15] software was used and, by creating the semi-wing model using the referred airfoil, it was possible to predict its aerodynamic behaviour by analysing C_L, C_D and C_M

coefficients and thus obtain lift and drag forces and pitch moment. Another property that has to be considered, since the aerodynamic simulation directly depends on it, is the *Reynolds* number

$$Re = \frac{\rho u L}{\mu}, \tag{3.2}$$

where ρ represents the air density in kg/m^3, u is the velocity of the fluid with respect to the object in m/s, L is a characteristic dimension in m and μ is the dynamic viscosity of the air in $kg/(m \cdot s)$. This non-dimensional quantity relates the inertia forces with the viscous forces and is a very important dimensionless quantity in fluid dynamics [16].

Considering the referred wind tunnel to be at sea level and using standard sea level (SSL) properties, let us assume that $\rho = 1.225\, kg/m^3$ and $\mu = 1.8 \times 10^{-5}\, kg/(m \cdot s)$. On the other hand, as said before, u is assumed to be equal to $50\, m/s$ and, in this case, the characteristic dimension is the chord that is equal to $0.5\, m$ for an aspect ratio of 4. In these conditions, we obtain a *Reynolds* number of 1.7×10^6.

Having determined all these properties, it is possible now to perform the aerodynamic analysis and investigate the expected loads to give us the order of magnitude that the balance has to be able to support and measure.

Giving the airfoil analysis performed *a priori* and the associated Reynolds number, stall phenomena occurs at an angle of attack of around $16°$. For this reason, we will be considering a maximum angle of attack of $16°$ for the wing analysis. Having discovered α, it is possible to obtain the maximum C_L value for the wing, graphically, that is shown in figure A.3(a). The plot of C_L against C_D gives us the maximum expected C_D and the plot of C_M against α allows us to infer the maximum value of C_M, both represented in figures A.3(b) and A.3(c), respectively.

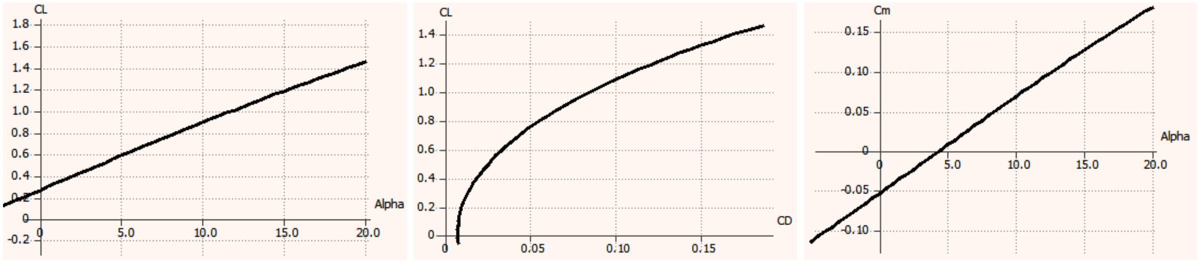

(a) C_L versus α (b) C_L versus C_D (c) C_M versus α

Figure 3.6: *XFLR5* simulation results for a wing with an aspect ratio of 4

Given the aerodynamic coefficients, the correspondent values of force and torque can be obtained using expressions (3.3) and (3.4), respectively

$$C_F = \frac{F}{\frac{1}{2}\rho u^2 S}, \tag{3.3}$$

$$C_M = \frac{M}{\frac{1}{2}\rho u^2 S c}, \tag{3.4}$$

where F and M represent a given force and torque component. Table 3.3 represents the wing aerodynamic coefficients alongside with the correspondent loads and torques.

If we consider the wing model to be flapped, some considerations have to be taken into account, like the size of the flap and its position in the wing. In this case, we considered it to be placed in the trailing edge, with an angle of $10°$, and to be positioned around 65% of the chord, as shown in figure 3.7. Considering the new resultant airfoil, stall phenomena occurs now for an angle of attack of around $14°$, for the same Reynolds number, as shown in appendix A. Table 3.3 shows the analogous values for this case, whose plots are also represented in appendix A.

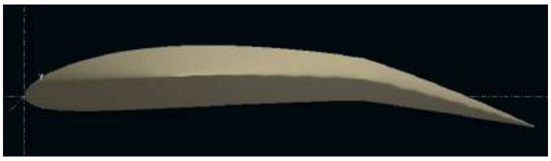

Figure 3.7: *NACA 4412* airfoil with 10° trailing edge flap

Table 3.2 sums up the main properties of the wing model that will be considered in the simulation.

Table 3.2: Wing and flow properties

	Wing Model
Aspect ratio (AR)	4
Span (b_w) $[m]$	2
Chord (c_w) $[m]$	0.5
Area (S_w) $[m^2]$	1
Flow velocity (u) $[m/s]$	50
Air density (ρ) $[kg/m^3]$	1.225
Dynamic viscosity (μ) $[kg/(m \cdot s)]$	1.8×10^{-5}
Reynolds number (Re)	1.7×10^{6}

The results relative to the previously described airfoils are shown in table 3.3, for the full wing and in table 3.4, for the half wing to be tested in the wind tunnel.

Table 3.3: Wing aerodynamic coefficients and loads

Airfoil	AR	α_{stall} [°]	C_D	C_L	C_M	Area $[m^2]$	F_X $[N]$	F_Z $[N]$	M_Y $[Nm]$
NACA 4412	4	16	0.131	1.233	0.165	1	201	1887	126
NACA 4412 - TE flap (10°)	4	14	0.221	1.529	0.144	1	338	2341	110

Regarding the components of force and torque, it is possible to verify that certain components are not considered, namely side force (F_Y), roll moment (M_X) and yaw moment (M_Z). The reason for this lies on the fact that, in this case, we are considering a full symmetric wing, attached to the wind tunnel in its aerodynamic center. This symmetry condition eliminates the components of yaw and roll moments. Giving the fact that the airflow is perpendicular to the wing, the side force is also zero.

As referred before, we will be testing half wing models and so it is necessary to convert the results from the complete model to the half model. Considering the loads (lift - F_Z and drag - F_X) the values of the semi-wing will be half of the original one, however the relation is not that simple as the matching is not direct. It is quite common to test half wing models attaching the root of the semi-wing and placing

Table 3.4: Half wing aerodynamic loads

Airfoil	AR	$F_X\ [N]$	$F_Y\ [N]$	$M_X\ [Nm]$	$M_Y\ [Nm]$	$M_Z\ [Nm]$
NACA 4412	4	101	944	472	50	63
NACA 4412 - TE flap (10°)	4	169	1171	585	84	55

it vertically which corresponds to rotate the wing $90°$ in the X-axis. In this case, the value of F_Y for the half-wing will correspond to half of the value of F_Z for the total wing and the value of F_Z for the half-wing will correspond to half of the value of F_Y for the total wing.

Considering the torques, in addition to the pitch moment (M_Y) that is also half of the full wing and now will correspond to M_Z, we have to consider the torques in the other two axis created in the support of the wing (in the middle of the full wing) by F_Y and F_X, that correspond, respectively, to M_X and M_Y. To calculate them it is necessary to know the center of pressure location along the span. Although we do not know exactly its position, it is located between the middle of the semi wing and the fuselage. In this case, we will consider the limit situation of it being located in the middle of the semi wing for it is the critical situation. These torques are given by the product of the force and the distance between the neutral axis that corresponds to the support of the semi wing and its center of pressure that corresponds, in this case, to the middle point that is located at a distance of $0.5\ m$ to the attachment point. Given so, we can complete the data from before and obtain the results presented in table 3.4. The presented values show that the components of torque generated by the support of the structure (M_X and M_Y) are greater than the torque created by the flow itself in the wing (M_Y).

Summing up these results, it is possible to come up with table 3.5 that shows the maximum loads and torques that the force balance is expected to carry. These results correspond to the NACA 4412 with a flap deflection at the trailing edge of $10°$. Assuming that the referred model is tested with a sideslip angle (figure 2.12) of $20°$, one can update the results with an expected value for the side force (in this case F_Z), as shown in the second row of the table 3.5.

Table 3.5: Expected maximum loads and torques

	β [°]	$F_X\ [N]$	$F_Y\ [N]$	$F_Z\ [N]$	$M_X\ [Nm]$	$M_Y\ [Nm]$	$M_Z\ [Nm]$
NACA 4412 - TE flap (10°)	0	169	1171	0	585	84	55
NACA 4412 - TE flap (10°)	20	213	1025	45	524	115	60

3.2.2 Full Aircraft Model

Another simulation can be performed to evaluate the behaviour of an aircraft model composed of main wings, tail and fuselage. The fuselage measures $1.1\ m$ and the leading edge of the wing is placed $0.3\ m$ after the fuselage nose. The wing has an aspect ratio of 4 which means that the chord is $0.25\ m$, as the span is equal to $1\ m$. The tail is located at the end of the fuselage. The vertical fin has a NACA 0012 airfoil and the horizontal stabilizer has a NACA 4412, the same used in the wings presented before. The resultant model is depicted in figure 3.8. In this case, an analysis on both the airfoils for wing and tail, NACA 4412 and NACA 0012, respectively, and considering the Reynolds number associated with the analysis that is shown in table 3.6, stall phenomena was found to occur at an angle of attack of $14°$, in the tail, as shown in appendix A.

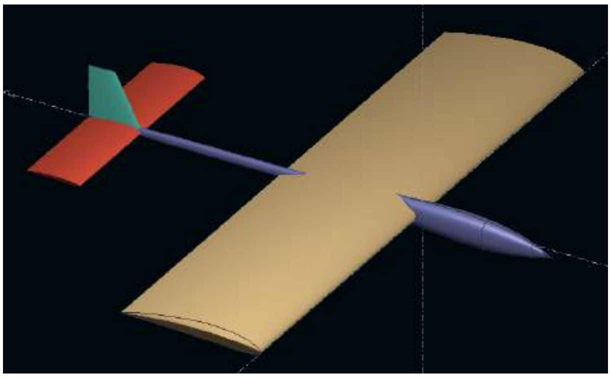

Figure 3.8: Schematic representation of the aircraft model

Similarly to what was done with the half wing models, a table with the main design properties can be presented (table 3.6).

Table 3.6: Full plane model design properties

	Wing	Horizontal Stabilizer	Vertical Stabilizer
Aspect ratio (AR)	4	4	2.5
Span (b) [m]	1	0.4	0.1
Chord (c) [m]	0.25	0.1	0.1 - root 0.06 - tip
Area (S) [m^2]	0.25	0.04	0.01
Flow velocity (u) [m/s]	50		
Air density (ρ) [kg/m^3]]	1.225		
Dynamic viscosity (μ) [$kg/(m \cdot s)$]	$1.8{\times}10^{-5}$		
Reynolds number (Re)	$0.85{\times}10^{6}$		

For the case of the full model represented in figure 3.8 and using a similar method as the one adopted for the half-wing, it was possible to obtain lift, drag and moment coefficient, by analysing their distribution, as represented in figure 3.9.

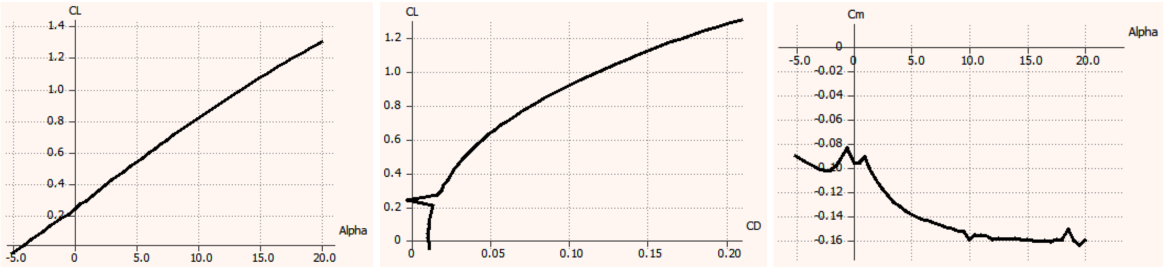

(a) C_L versus α (b) C_L versus C_D (c) C_M versus α

Figure 3.9: *XFLR5* simulation results for the full aircraft model

The set of results that were obtained are presented in table 3.7. In this case, the software uses the wing area as a reference for the full model to obtain the set of loads and torques represented in table 3.8.

Table 3.7: Aircraft model aerodynamic coefficients

	β [°]	C_D	C_L	C_Y	C_{M_X}	C_{M_Y}	C_{M_Z}
Aircraft model	0	0.125	1.019	0	0	0.159	0
Aircraft model	20	0.196	0.897	0.062	0.006	0.147	0.013

Table 3.8: Aircraft model aerodynamic forces and torques

	β [°]	F_X $[N]$	F_Y $[N]$	F_Z $[N]$	M_X $[Nm]$	M_Y $[Nm]$	M_Z $[Nm]$
Aircraft model	0	48	0	390	0	15	0
Aircraft model	20	75	24	343	1	14	1

3.2.3 Limit Loads and Displacements

The set of results presented before is, as said, a tool to analyse the possible limits of the force balance and to be aware of the order of magnitude of forces and torques to be measured.

Assuming, for both half-wing and aircraft models, an hypothetical situation that results from considering the greatest components of loads and torques of all testing scenarios, it is possible to come up with the worst loading scenario for the half-wing model, represented in table 3.9, and for the full aircraft model, shown in table 3.10.

Table 3.9: Limit loading situation for the half-wing model

	F_X $[N]$	F_Y $[N]$	F_Z $[N]$	M_X $[Nm]$	M_Y $[Nm]$	M_Z $[Nm]$
Half-wing model	213	1171	45	585	115	60

Table 3.10: Limit loading situation for the full aircraft model

	F_X $[N]$	F_Y $[N]$	F_Z $[N]$	M_X $[Nm]$	M_Y $[Nm]$	M_Z $[Nm]$
Aircraft model	75	24	390	1	15	1

Now that the range of maximum expected loads and torques is defined, it is important to guarantee that the force balance does not deform past a certain pre-defined limit. For instance, it is necessary that the point where the model is to be attached does not suffer significant angular displacements as they can induce different aerodynamic angles from the ones that are being tested and, therefore, different aerodynamic loads. These limits have to be defined not only in terms of rotation, but also in terms of translation. Considering the fact that half-wing models are placed vertically in the wind tunnel, limiting the rotation in the Y-axis corresponds to restrict variations in the sideslip angle (β) and, similarly, limiting the rotation in the Z-axis corresponds to narrow the angle of attack (α) variation. As for the full aircraft model, a rotation in Y-axis will change the angle of attack (α) and a rotation in Z-axis will affect the sideslip angle (β). It is also important, in order to guarantee the integrity of the force balance structure, to limit the linear displacement. The selected limits for angular and linear displacements are represented in table 3.11.

Table 3.11: Maximum admissible displacements

θ_Y [°]	θ_Z [°]	Linear displacement [mm]
0.5	0.5	10

3.3 Concept Selection

The previous analyses were important to know the range of load values that the force balance has to be able to support. However, as discussed in section 2.2, there are many types of force balances which application depends on many factors, mainly the testing conditions.

In this specific case, given the fact that the force balance will be used in an academic environment and to test models of different shapes, it is important to guarantee both versatility and simplicity of construction that are only possible to achieve with external balances. In fact, internal balances are greatly dependent on the model shape and for this reason they are not adequate for our purpose. The balance is expected to be used in tests for a wide variety of models, such as wings and scaled planes.

As described in section 2.2.1, there are different types of external force balances and for this reason it is important to analyse and discuss the advantages and disadvantages of each configuration. The most appropriate manner to do so is to carefully compare different existent solutions, highlighting their pros and cons and quantitatively assess some of their main features.

The most widely adopted configuration is the platform type given its robustness, orthogonality and simplicity of construction.

Figures 3.10(a) and 3.10(b) show two examples of platform-type external force balances that are very similar, the first is capable of measure 5 components (lift and drag forces and pitching, rolling and yawing moments) while the second also measures side forces [20]. Another difference is that the first one has only one arm to support the model, while the latter has three. This last configuration is very common when the model in test is a scaled plane since two arms support the wings and the third supports the tail [21]. Although, at a first glance, they may appear very different, their construction and operating modes are very similar. Both force balances present an issue related with a false pitching moment induced by drag forces that has to be taken into account during calibration process.

Another possible architecture is shown in figure 3.10(c). In this case, there is a rotating frame, which is the equivalent of the main structure described above, and also a fixed frame used to measure the yaw component [22]. Comparatively to the usual platform balances, shown in figures 3.10(a) and 3.10(b), it allows to increase measurement accuracy, however its greater complexity can become an issue when it comes to construction.

On the other hand, we have pyramidal force balances as exemplified in figure 3.10(d). Although this is a commercial solution thus presenting greater complexity, pyramidal force balances present a

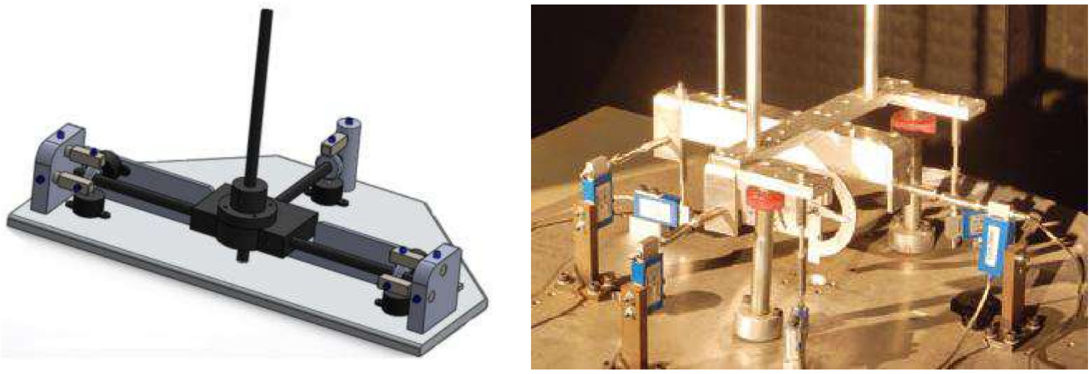

(a) Platform simple (AEROLAB)

(b) Platform with triple support

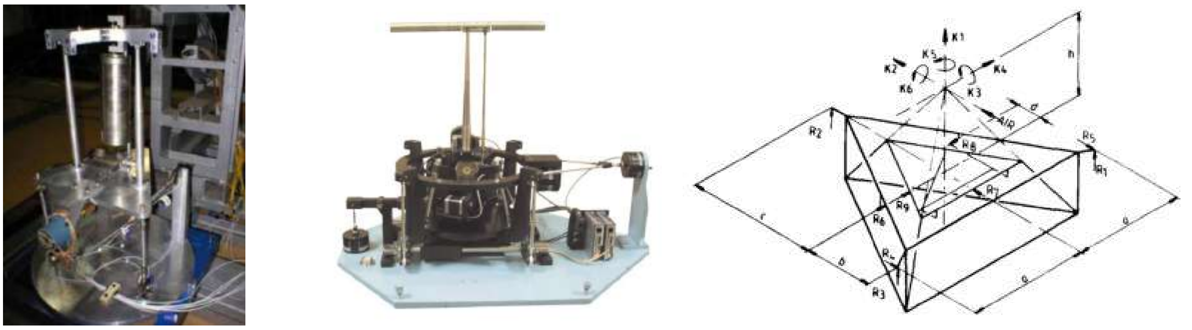

(c) Rotating-platform (Military Technical Institute, Belgrade)

(d) Pyramidal (Aerolab)

(e) Pyramidal-platform [17]

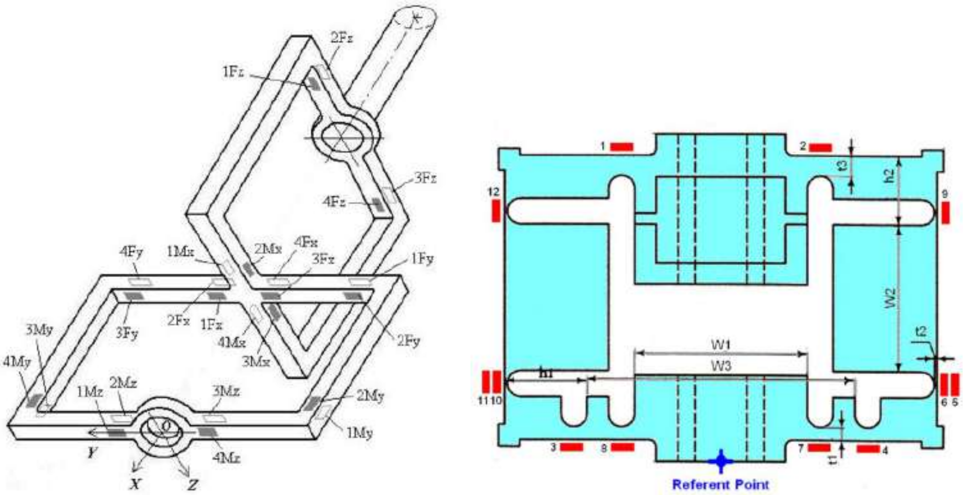

(f) Innovative design 1 (and *Wheatstone* bridges placement) [18]

(g) Innovative design 2 [19]

Figure 3.10: Typical architectures for external force balances

larger number of components when compared to platform force balances. This complexity is necessary to diminish the associated errors and to eliminate some interferences between load components. This balance has two main parts: the “spider”, where torques are measured and the “cradle” where forces are measured. Torques are converted to forces through lever arms and directed to the load cells and the forces are directly transferred to load cells. There are six loads cells each of which is used to measure one load component [23].

It is possible to merge both the previous force balance concepts in order to come up with an innovative solution that combines the advantages from platform and pyramidal force balances that were stated previously, namely decoupling of forces and torques and positioning of the model in the test section. When compared to a platform balance, this kind of approach allows to diminish error amplifications by a factor of 10. It also presents good versatility as it can be used as platform, pyramidal or both and its design reduces the number of load cells from 15 to 9 which represents a great advantage in the instrumentation phase [17]. This innovative solution is shown in figure 3.10(e).

Other creative and innovative concepts have been developed over the past few years. Two of these examples are represented in figures 3.10(f) and 3.10(g). Figure 3.10(f) represents a force balance that was constructed by machining a single piece of material, for this reason it can be called a monolithic structure. The main advantages of this balance are related with its simple geometry that allows to have a low cost manufacturing price and, also, its versatility since its shape is suitable for use as internal or external balance. Maximum coupling error occurs for force in *x* direction and torque in *Z* direction and is about 5% [18]. Similarly, figure 3.10(g) also represents a monolithic structure. In this case, this balance is only able to measure lift, drag and pitching moment which is a disadvantage since it is required a six-component force balance. It is possible to highlight the major advantages of this concept: since it is made of one piece of material, there is no assembly operation, it is only necessary to attach the *Wheatstone* bridges each of which measures one load component. However, its machining may not be easy to perform [19].

3.3.1 Selection Methodology

Having presented this set of concepts and discussed some of their advantages and disadvantages, it is important now to compare them and evaluate which one is the best option to apply to our testing conditions. The best way to perform this analysis is to define categories and requirements and assess each design in each category. These requirements have to meet wind tunnel specifications, testing conditions and guarantee a user-friendly operation. The set of force balance types to be compared are platform (figures 3.10(a) and 3.10(b)), rotating platform (figure 3.10(c)), pyramidal (figure 3.10(d)), pyramidal-platform (figure 3.10(e)) and innovative designs (figures 3.10(f) and 3.10(g)). The use of Analytic Hierarchy Process (AHP) [24] is the best way to gather all the information, evaluate categories and obtain the best solution since it is adequate for complex decision making by reducing them to sets of pairwise comparisons. The decisions are based on both evaluation criteria and types of force balance. The AHP generates a weight for each criterion, based on decision maker's pairwise comparisons, that reflects its importance. Then, for a certain criterion, all of the options are compared and a score is assigned to each option. At the end, the option scores are combined with the criteria weights and the global score for each option is determined. This process is important in the sense that it allows to decrease the personal bias associated with this type of comparative analysis.

First, it is important to introduce and define the criteria that is going to be considered. It is possible to highlight two main categories: construction and operation that are worth around 40% and 60% in terms of the total force balance assessment, respectively.

Regarding construction, among the set of criteria that one can find to be important, there are some of greater relevance:

- **Robustness (A)** It evaluates the strength and integrity of the force balance when submitted to different types of testing conditions;
- **Simplicity (B)** It gives an insight about the number of parts, their shape and the assembling process;
- **Fabrication (C)** This criterion evaluates manufacturing processes of the balance components, namely machining processes and materials to be used;
- **Instrumentation (D)** It is related with the strain gauges, namely the number and their attachment in the force balance;
- **Structurally adaptable (E)** This feature allows the force balance to, after his construction, suffer some replacements on its components being it because of damages or to implement some fittings;
- **Innovative design (F)** Although there are specific common types of external force balances, as described in section 2.2.1, one can find some variations as seen in figures 3.10(f) and 3.10(g). This criterion assesses eventual creative and innovative characteristics;
- **Cost (G)** It evaluates the overall fabrication, assembling and instrumentation costs.

In a similar manner, when it comes to operation, it is possible to highlight some more important criteria:

- **Wind tunnel attachment (H)** It evaluates the easiness of installation of the force balance in the wind tunnel;
- **Support versatility (I)** This criterion is related with the ability of the force balance to measure different types of models with different shapes since some force balances are designed to test specific types of models, like aircraft and some others are so versatile that can be used either as an internal or external force balance;
- **Measurement accuracy (J)** It evaluates the validity of the experimental results;
- **Force and torque decoupling (K)** The shape of the force balance simplifies the processing of the results by separating force and torque components;
- **Results processing (L)** It assesses the way the results are treated until they reach the final user.

Table 3.12 represents the pairwise comparison matrix, where criteria A to L are the ones stated above, in the same order. The values a_{jk} of the matrix can be interpreted in the following manner: 1 if *j* and *k* are equally important, 3 if *j* is slightly more important than *k*, 5 if *j* is more important than *k*, 7 if *j* is strongly more important than *k* and 9 if *j* is absolutely more important than *k* and all the integers in-between can be considered. In general, if $a_{jk} > 1$, *j* is more important than *k* and if $a_{jk} < 1$, *k* is more important than *j*. The last column shows the weight vector that represents the percentage of each criterion for the final score.

Table 3.12: Criteria pairwise comparison and weight vector

	A	**B**	**C**	**D**	**E**	**F**	**G**	**H**	**I**	**J**	**K**	**L**	**Weight Vector**
A	1	2	1/3	1/2	1/2	5	1/6	1/4	1/2	1/7	1/2	1/7	0.032
B	1/2	1	1/3	1/4	1/2	5	1/5	1/4	1/3	1/6	2	1/7	0.031
C	3	3	1	3	2	5	1/3	1/2	1/2	1/5	2	1/5	0.065
D	2	4	1/3	1	1/3	4	1/5	1/2	1/3	1/5	2	1/6	0.044
E	2	2	1/2	3	1	5	1/4	1/3	1	1/2	4	1/3	0.068
F	1/5	1/5	1/5	1/4	1/5	1	1/6	1/6	1/5	1/7	1/3	1/7	0.015
G	6	5	3	5	4	6	1	1/2	1/2	1/3	3	1/4	0.110
H	4	4	2	2	3	6	2	1	1	1/3	4	1	0.114
I	2	3	2	3	1	5	2	1	1	1/3	5	1/3	0.092
J	7	6	5	5	2	7	3	3	3	1	6	2	0.215
K	2	1/2	1/2	1/2	1/4	3	1/3	1/4	1/5	1/6	1	1/6	0.029
L	7	7	5	6	3	7	4	1	3	1/2	6	1	0.187

After creating this matrix, it is necessary to compare all the options with respect to each criterion. To do so, twelve matrices, shown in appendix B, are created, one for each criterion, in which pairwise comparisons are made for all the options using the same methodology used to obtain the matrix represented in table 3.12. After that, one can obtain the correspondent score matrix whose columns are the weight vectors of the twelve matrices, in order. The vector of final scores, for each type, is obtained by multiplying the score matrix with the criteria weight vector represented in table 3.12.

The validity of this method is guaranteed by checking the consistency of the whole process. The two factors used to do so are the *Consistency Index (CI)* and *Random Index (RI)* and the ratio $\frac{CI}{RI}$ must be smaller than 0.1, that is the limit of tolerance for inconsistencies. The *Consistency Index (CI)* can be obtained as

$$CI = \frac{x-m}{m-1}, \tag{3.5}$$

where m represents the number of criteria and x is a scalar that represents the average of the elements of the vector whose j^{th} element is the ratio of the j^{th} element of the vector $A \cdot w$ to the corresponding element of the vector w, being A the criteria pairwise comparison matrix of table 3.12 and w the weight vector represented in the last column of the same table. This value was found to be 0.1178 and the *Random Index (RI)* was found to be 1.48, for the case of twelve criteria. In this case, $\frac{CI}{RI}$ is equal to 0.08 which is smaller than 0.1 and, for this reason, the consistency is checked.

Figure 3.11 shows the final scores of all the considered possibilities of external force balances. Types 1 to 6 refer to platform, rotational platform, pyramidal, pyramidal-platform and innovative designs of figures 3.10(f) and 3.10(g), respectively. It can be seen that the platform force balance presents the maximum score, followed by the rotational-platform. Although the platform balances are very simple, they present a very good commitment in an academic environment due to the simplicity of assembly,

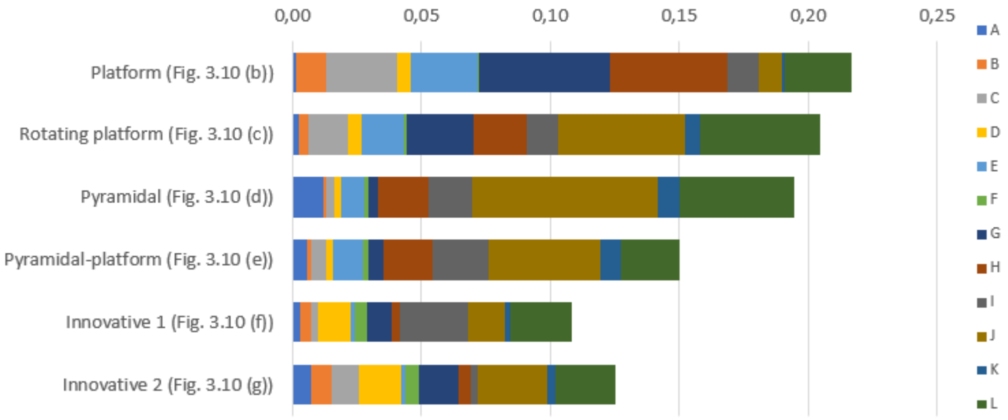

Figure 3.11: Final AHP score per force balance type

operation and maintenance.

3.3.2 *Stewart* Platform

As seen before, it is possible to have platform balances with different shapes although in general they have the main plate (platform) which is connected to the strut where the model is mounted. This platform is supported by bars that are linked to a fixed platform on the floor and are supposed to carry axial forces only. The connection between the bars and both platforms is made by spherical joints to avoid torsion and bending phenomena in the bars. Forces and torques are obtained using strain gauge extensometers that are coupled to each bar as *Wheatstone bridges* and measure axial displacements. These displacements together with mechanical properties can be used to infer stresses and forces.

In general terms, we are interested in having six degrees of freedom. To accomplish this, it is necessary to consider six bars that must not be collinear so that the six leg forces can be linearly independent. One of the most known mechanisms is called the *Stewart* platform. Since its appearance, it was used mainly in flight simulators in the training of pilots, although it can be used in many other physical tests. In this case, and provided its good stiffness, it is suggested to be used as a force and torque sensor by instrumenting its elastic legs [25].

Stewart platforms may present diverse shapes but the most widely known are designated by 3-3, 3-6 and 6-6, represented in figure 3.12 [26]. In the first case, both fixed and moving platforms present a triangular shape. This shape, theoretically and for certain dimensions, has good load carrying capability, however it brings up a construction problem as the spherical joints at both platforms must be double, since they have to join two bars at the same vertex. This problem appears also for the 3-6 type since one of the platforms is triangular and two bars coming from two vertices of the other platform join at the same vertex. Regarding the 6-6 type, by analogy, one can see that both platforms have six vertices and the connections between the bars and the platforms is made by simple spherical joint, each one of them connecting one bar to one vertex.

Although these are the most common designs, some variations may arise to simplify construction or operation. These variations have, however, to be carefully calculated and dimensioned because some

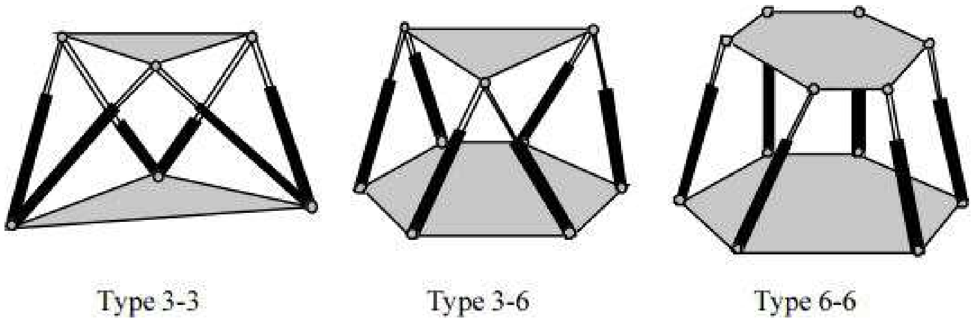

Figure 3.12: *Stewart* platform types [27]

configurations may lead to uncontrollable states known as singularities. In the case of a force-torque sensor, when singularities occur it is impossible to balance a certain load applied to the platform.

To evaluate the quality of a certain design, it was introduced the *quality index* (λ), that varies from 0 to 1, being 1 the optimal design and 0 a design with singularities. This quality index takes a maximum value of 1 that corresponds to the optimal configuration in which the determinant of the correspondent Jacobian matrix is maximum. The Jacobian matrix relates the axial forces in the i^{th} bar with the applied forces and torques and has the form

$$J = \begin{bmatrix} \hat{S}_1 & \hat{S}_2 & \ldots & \hat{S}_n \end{bmatrix}, \tag{3.6}$$

where *n* is the number of bars and $\hat{S}_i$ is the unit vector of the Plucker coordinates along the line of the i^{th} bar. The unit vector $\hat{S}_i$ has six components, the first three represent the coordinates of the line along the i^{th} bar and the remaining three correspond to the components of the external product of the vector from the origin to the vertex of one plate and the other is the vector from the origin to the vertex of the other plate, of the i^{th} bar. The coherence between the order of the vectors of the external product and the vector of the bar must be guaranteed [28].

If we imagine a bar, whose vertices have coordinates (x_1, y_1, z_1) and (x_2, y_2, z_2) and we define the vector along the line of the bar to be from 1 to 2, the first three components of vector S for the referred bar are ($x_2 - x_1$, $y_2 - y_1$, $z_2 - z_1$) and the remaining three components can be obtained by

$$\begin{vmatrix} \hat{i} & \hat{j} & \hat{k} \\ x_1 & y_1 & z_1 \\ x_2 & y_2 & z_2 \end{vmatrix} = (y_1 z_2 - y_2 z_1)\hat{i} + (x_2 z_1 - x_1 z_2)\hat{j} + (x_1 y_2 - x_2 y_1)\hat{k}. \tag{3.7}$$

Combining the previous results, it is possible to obtain, for a bar *i*, the vector $\hat{S}_i$, with vertices 1 and 2,

$$\hat{S}_i = \begin{bmatrix} x_2 - x_1 & y_2 - y_1 & z_2 - z_1 & y_1 z_2 - y_2 z_1 & x_2 z_1 - x_1 z_2 & x_1 y_2 - x_2 y_1 \end{bmatrix}. \tag{3.8}$$

With this, one can obtain the Jacobian matrix, as shown in equation (3.6) and thus the quality index (λ). The quality index is obtained as

$$\lambda = \frac{|J|}{|J|_m} \tag{3.9}$$

where $|J|$ stands for the determinant of the Jacobian matrix of a certain configuration to be studied and $|J|_m$ stands for the determinant of the Jacobian matrix that corresponds to the optimal configuration.

As discussed before, the *Stewart* platform may be of three types: 3-3, 3-6 and 6-6. Ideally, the octahedral type 3 platform shown in figure 3.12 is considered to be the most geometrically stable design, particularly when the side of the fixed platform is twice the size of the moving platform being the later equal to the distance between both platforms. Despite these design advantages, both 3-3 and 3-6 *Stewart* platforms present the same issues when it comes to construction. They require, as referred previously, the use of double spherical joints at the vertices of the 3 sided plates, that means that in the case of 3-3 platform each of all joints must support two bars, and in the case of 3-6 platform, three of the spherical joints must be double. This type of double-joint is impossible to have in practice as it is hard to manufacture and, moreover, it causes interference phenomena between the bars. For this reason, the most reasonable solution is to separate this double joints by transforming a three-sided plate in a six-sided plate [29].

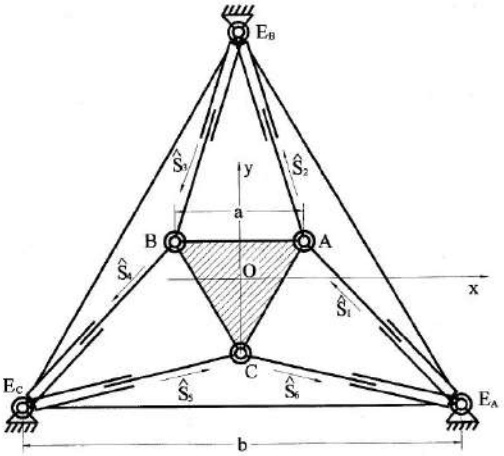

Figure 3.13: 3-3 *Stewart* platform with double spherical joints [29]

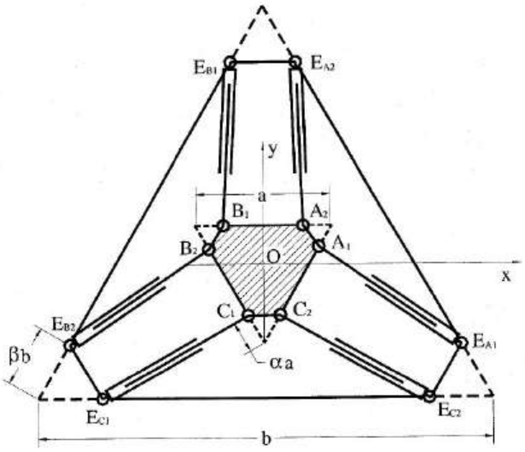

Figure 3.14: 6-6 *Stewart* platform based on the 3-3 platform [29]

For instance, the 3-3 platform presented in figure 3.13 can be transformed in a 6-6 platform similar to the one whose planform is represented in figure 3.14, thus vanishing construction and coupling issues related with double spherical joints.

Having these considerations in mind, one can come up with diverse solutions of an effective platform to be used as a force and torque sensor. One possible approach is to use a 6-6 platform, with both hexagonal plates and spherical joints at the vertices, as represented in figure 3.15.

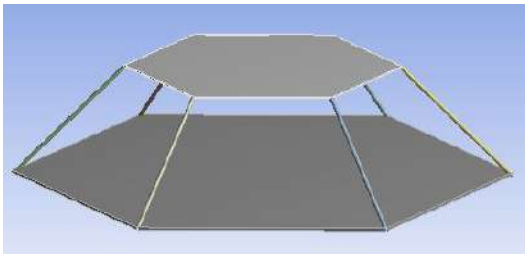

Figure 3.15: Hexagonal platform

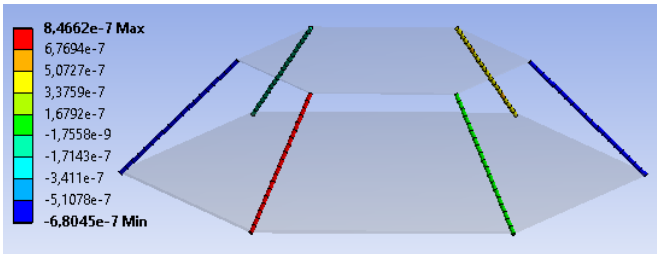

Figure 3.16: Maximum axial forces when M_Z is applied

This mechanism could be, provided the considerations made before and its simple assembly, a good solution for the force balance, however, a static structural analysis using *ANSYS Workbench 16.0* proved this wrong. To perform this analysis, the model shown in figure 3.15 was assumed to have both platforms made of structural steel and circular cross-section bars of aluminium. These materials may not correspond to reality, specially the moving platform due to the high weight, but are a good starting point. The analysis was carried assuming the maximum loads and torques that are expected to be measured and were determined in section 3.2.3. The results of this analysis are shown in table 3.13.

Force balance	F_X $(215\,N)$	F_Y $(1170\,N)$	F_Z $(390\,N)$	M_X $(585\,Nm)$	M_Y $(115\,Nm)$	M_Z $(60\,Nm)$
			Maximum axial force (N)			
Hexagonal (Fig. 3.15)	47.8	300	91.9	253.9	43.2	10^{-7}

Table 3.13: Hexagonal platform - static structural analysis results

In terms of dimensions, the upper platform has a radius of $500\ mm$, the distance between both platforms is $400\ mm$ as is the projected length of each bar in the horizontal plane. Table 3.13 shows axial force of the bars since this parameter is directly related with their displacement, by considering both mechanical and geometrical properties. The problem stated earlier that is related with this structure can be seen when the maximum expected torque in *Z* direction is applied, in this case the maximum axial force is of the order of 10^{-7}. When compared to the values of axial forces for the remaining loading conditions that are of the order of $10^1 - 10^2$, that particular value is really small and this represents a problem when it comes to measuring since it would require ultra sensitive and precise extensometers capable of measure such small quantities. For this reason, this design was not taken into account.

To overcome this problem, it was necessary to change the position of the bars, in particular, their orientation with relation to the vertical axis. Since we already concluded that, for the sake of construction and precise measuring, it is imperative to have a 6-6 *Stewart platform* and one is interested in obtaining the quality index of the proposed designs, we have to calculate the Jacobian matrix of this configuration. Applying equation (3.6) to the general configuration of a 6-6 platform represented in figure 3.14, it is possible to obtain the Jacobian matrix and thus its determinant,

$$|J| = \frac{81\sqrt{3}a^3b^3h^3(3\alpha\beta - 2\alpha - 2\beta + 1)^3}{4(a^2(3\alpha^2 - 3\alpha + 1) + ab(3\alpha\beta - 1) + b^2(3\beta^2 - 3\beta + 1) + 3h^2)^3}. \tag{3.10}$$

The maximum value of $|J|$ or, using the adopted notation, $|J|_m$ that corresponds to the optimal design is found by differentiating equation (3.10) with respect to h and equating to 0 resulting in

$$h = \sqrt{\frac{1}{3}(a^2(3\alpha^2 - 3\alpha + 1) + ab(3\alpha\beta - 1) + b^2(3\beta^2 - 3\beta + 1))}. \tag{3.11}$$

Considering the maximum height between the two platforms (h) to be 0.5 meters in order for the balance to be outside the flow and, for instance, $\alpha = \frac{1}{4}$, $\beta = \frac{1}{6}$ and $b = a$, applying the conditions above, the force balance would present unreasonable values for a and b, in this case, around 2.27 meters. This would require almost all the available area inside the wind tunnel and tremendous amounts of material. That is why this design is not feasible.

To overcome this problem, it is necessary to design a new structure and assess its quality index. For a configuration similar to figure 3.14, the general set of coordinates is

$$\begin{array}{ll}
A_1\left(\frac{a(1-\alpha)}{2},\frac{a(1-3\alpha)}{2\sqrt{3}},h\right) & A_2\left(\frac{a(1-2\alpha)}{2},\frac{a}{2\sqrt{3}},h\right)\\
B_1\left(\frac{a(2\alpha-1)}{2},\frac{a}{2\sqrt{3}},h\right) & B_2\left(\frac{a(\alpha-1)}{2},\frac{a(1-3\alpha)}{2\sqrt{3}},h\right)\\
C_1\left(-\frac{a\alpha}{2},\frac{a(3\alpha-2)}{2\sqrt{3}},h\right) & C_2\left(\frac{a\alpha}{2},\frac{a(3\alpha-2)}{2\sqrt{3}},h\right)\\
E_{A1}\left(\frac{b(1-\beta)}{2},\frac{b(3\beta-1)}{2\sqrt{3}},0\right) & E_{A2}\left(\frac{b\beta}{2},\frac{b(2-3\beta)}{2\sqrt{3}},0\right)\\
E_{B1}\left(-\frac{b\beta}{2},\frac{b(2-3\beta)}{2\sqrt{3}},0\right) & E_{B2}\left(\frac{b(\beta-1)}{2},\frac{b(3\beta-1)}{2\sqrt{3}},0\right)\\
E_{C1}\left(\frac{b(2\beta-1)}{2},-\frac{b}{2\sqrt{3}},0\right) & E_{C2}\left(\frac{b(1-2\beta)}{2},-\frac{b}{2\sqrt{3}},0\right).
\end{array}$$

The overall configuration must respect the dimensions of the available area of the wind tunnel and has to be efficient in terms of construction, that is, using the minimum amount of material to obtain the best possible results. This factor is not taken into account with the quality index, since it only assesses the design, comparing it to the optimal configuration.

By analysing the relation between the different parameters that define the balance configuration (a, b, α, β, h) and obtaining the quality factor for different feasible sets of properties, as represented in appendix C, it was possible to get a good configuration without compromise both quality of design and mechanical feasibility. This final configuration is defined by $a = 350\,mm$, $b = 700\,mm$, $\alpha a = 60\,mm$, $\beta b = 45\,mm$ and $h = 300\,mm$ and has a quality index of $\lambda = 0.995$, which is pretty close to the optimal design. The definition of αa and βb instead of α and β, respectively, was due to a thinking forward process: one is interested in having a shape that is the best approximation to a triangle as possible, for the both platforms. This forces the connection of the two bars to be as close as possible to the virtual vertex. The values of αa and βb represent, respectively, the trimmed vertices of upper and base platforms and consider the minimum distance between the two connections of the bars to the platforms taking also into account the connection mechanism that will be presented later. Such configuration is depicted in figure 3.17.

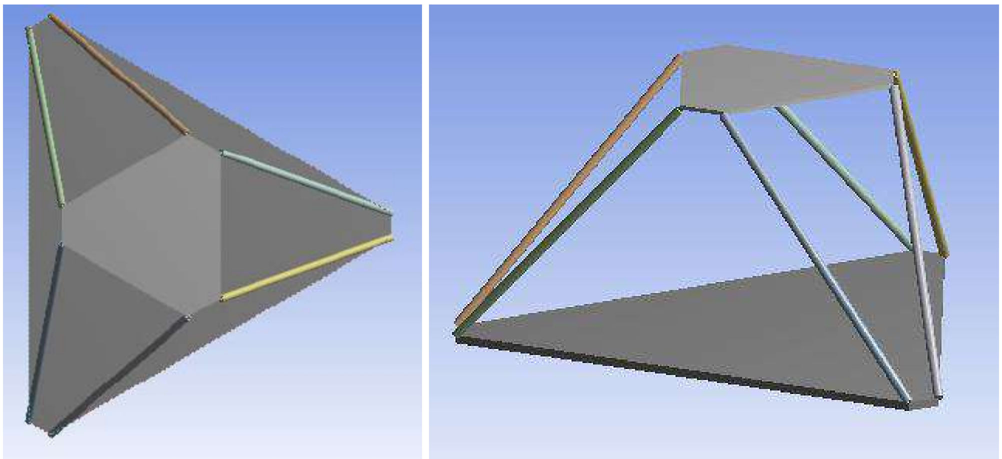

(a) Planform

(b) *3D* model

Figure 3.17: *Stewart* platform final configuration

In order to assess the validity of this structure, a similar analysis to the one performed to the hexagonal platform has to be carried out, by applying the maximum expected forced and torques and analysing the maximum axial force in the bars. As one can conclude by analysing the results presented in table 3.14, the order of magnitude of the axial forces for each component of force and torque applied to the structure is similar, varying from 10^1 to 10^3. It is possible to conclude, that the issue of one axial force being at least six orders of magnitude smaller than the remaining ones no longer exists thus vanishing the measuring difficulty stated before.

Force balance	F_X $(215\,N)$	F_Y $(1170\,N)$	F_Z $(390\,N)$	M_X $(585\,Nm)$	M_Y $(115\,Nm)$	M_Z $(60\,Nm)$	All components
				Maximum axial force (N)			
Final configuration (Fig. 3.17(b))	103.2	589.7	90	1750.3	360.9	101.8	2346.2

Table 3.14: *Stewart* platform - static structural analysis results

Besides the main frame depicted above that composes the structure of the balance, additional components have to be implemented in order to ensure that it is fully operational. For instance, a strut has to be attached perpendicular to the upper platform, in its center; this element will support the model to be tested. After coupling the model in the force balance, one is interested in adjust both sideslip angle (β) and the angle of attack (α). It is important to note that α and β are different from the ones referred previously as in this case they represent angles instead of construction parameters of the *Stewart* platform.

In order to adjust the sideslip angle, a rotational apparel has to be designed and adapted to the force balance. The main idea is to build a rotary table using a fixed plate coupled to a rotary mechanism in which the bottom platform of the main structure of the force balance will be mounted. This mechanism will allow the user to choose the desired β angle to perform the test just by rotating the force balance over the table.

The adjustment of the angle of attack is made by controlling the position of the support in which the model is to be fixed. This support will be attached to the extremity of the strut that will be placed in the center of the upper platform. The adjustment of these angles has to be carried out prior to the experimental procedures.

The detailed composition of the force balance will be detailed in Chapter 4.

Chapter 4

Mechanical Design

Having defined the general configuration, it is necessary to design each of the components, determining their exact dimensions and the materials to be used, so they can be manufactured or purchased.

(a) Aircraft testing (b) Half wing testing

Figure 4.1: Preliminary model of the force balance

In general terms, the force-moment sensor is constituted by two platforms with six sides, being the upper one smaller than the base platform. The connection between these platforms is made by means of bars. Since, as said before, these bars have to deform and carry loads only in the axial direction, ball joints will be placed in their extremities. To connect the ball joints to each of the platforms, a metallic coupler will be designed. A strut will also be needed to mount the model to be tested as well as a mechanism to fix it to the upper platform. In this case, we will be considering two different struts, one to test half wing models and another to test full plane models, as we are interested in placing the models at the center of the test section; this will be discussed later in section 4.2.1. These are the main components of the force balance, although it is also necessary to develop mechanisms to adjust the angles of attack and sideslip as well as a solution to fix it to the ground. The preliminary model is represented in figure 4.1 for aircraft (figure 4.1(a) and half wing (figure 4.1(b) testing.

This model, although very close to the final configuration, may suffer some adaptations in order to fulfil the design requirements that were previously defined in section 3.2.3 (load range and admissible angular displacements).

4.1 Computational Structural Model

In order to analyse the model subjected to the expected operation conditions, finite element analysis will be performed using *SolidWorks*, v2017 by *Dassault Systèmes*. A very important aspect one has to take into consideration in this type of analysis is the mesh considered to discretize the whole structure, since we are transforming a continuous domain in a discrete domain. In terms of element type and considering the use of a high-quality mesh, parabolic tetrahedral solid elements will be used to discretize the domain adopting a curvature-based mesher that will automatically refine the mesh near the curves and edges of the structure. These elements are defined by four corner nodes, six mid-side nodes, and six edges, as shown in figure 4.2.

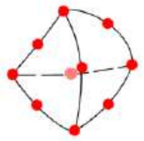

Figure 4.2: Parabolic tetrahedral solid element (*SolidWorks*, Corp.)

In order to assess the influence of the mesh size in the results of the analysis and considering the maximum expected load range for the test with the plane model acting on the force balance and using coarser and finer meshes, it is possible to fix a certain point in the structure (near the region of the strut where the stress values are higher) and plot both stress and displacement variation with the number of elements, as represented in figures 4.3(a) and 4.3(b), respectively.

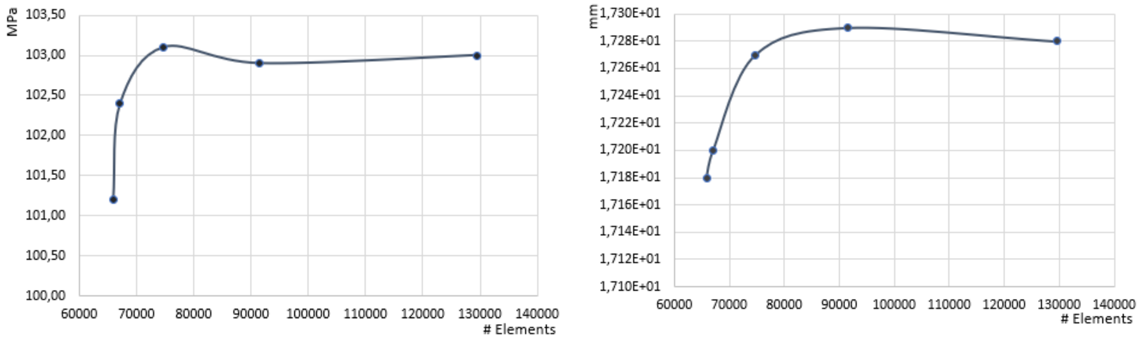

(a) Stress variation with the number of elements

(b) Displacement variation with the number of elements

Figure 4.3: Mesh study

An analysis of both plots (figure 4.3) leads one to conclude that from a certain number of elements (approximately 80000) on, the values of stress and displacement do not vary significantly. Another important factor that has to be taken into account is the amount of time to run the analysis: considering the last two points on both plots, where the leftmost one corresponds to 91518 elements and the rightmost one to 129563, took, respectively, 6 minutes and 17 minutes to finish the analysis and, for this reason, the choice lied on discretize the structure into 91518 which corresponds to use solid elements with a maximum size of $20\,mm$ and a minimum size of $5\,mm$ although guaranteeing the mesh refinement in the regions of edges and curves.

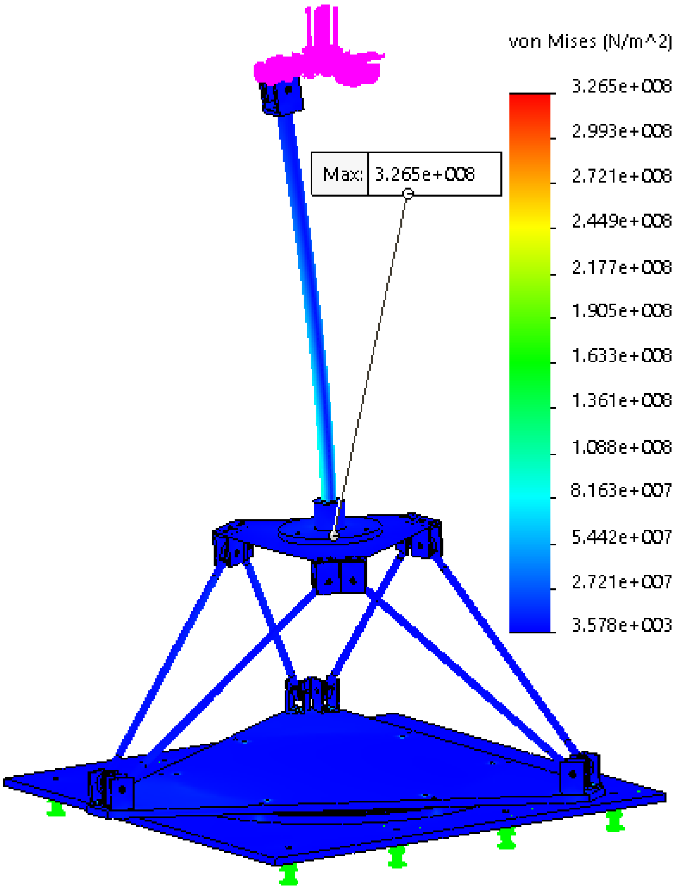

Figure 4.4: Stress distribution for the plane model maximum load

Considering the maximum load range found previously for the full aircraft model (table 3.10) and applying it to the preliminary design of the force balance, we obtain the stress results represented in figure 4.4. The shape of this preliminary model will be described later on and the necessary changes to fulfil the requirements will also be discussed but, besides the platforms and the bars, a strut with $550\,mm$ of height and a cross section with an external diameter of $20\,mm$ and an internal diameter of $16\,mm$ is used in this first approach. The results for the halfwing force balance are shown in appendix D and all the technical drawing for all the designed components are shown in appendix E.

4.2 Sizing and Material Selection

4.2.1 Strut and Flange

In terms of design, the strut consists of a metallic bar that connects the model that is positioned in the center of the test section to the force balance structure. Since this strut will be placed in the test section, it will also be subjected to the flow forces. For this reason, it is important to guarantee that the surface area of the strut crossed by the airflow is minimum and so, the best way to guarantee this is to use a bar with a relatively small diameter. On the other hand, forces and moments will be applied in the attachment point that is the top of the strut and it is necessary to keep the rotation of the strut below certain predefined values and thus limiting torsion and bending behaviour of the strut. This is achieved by modifying the shape of both strut and flange. This last component consists of a metallic disc that connects the strut and the moving platform.

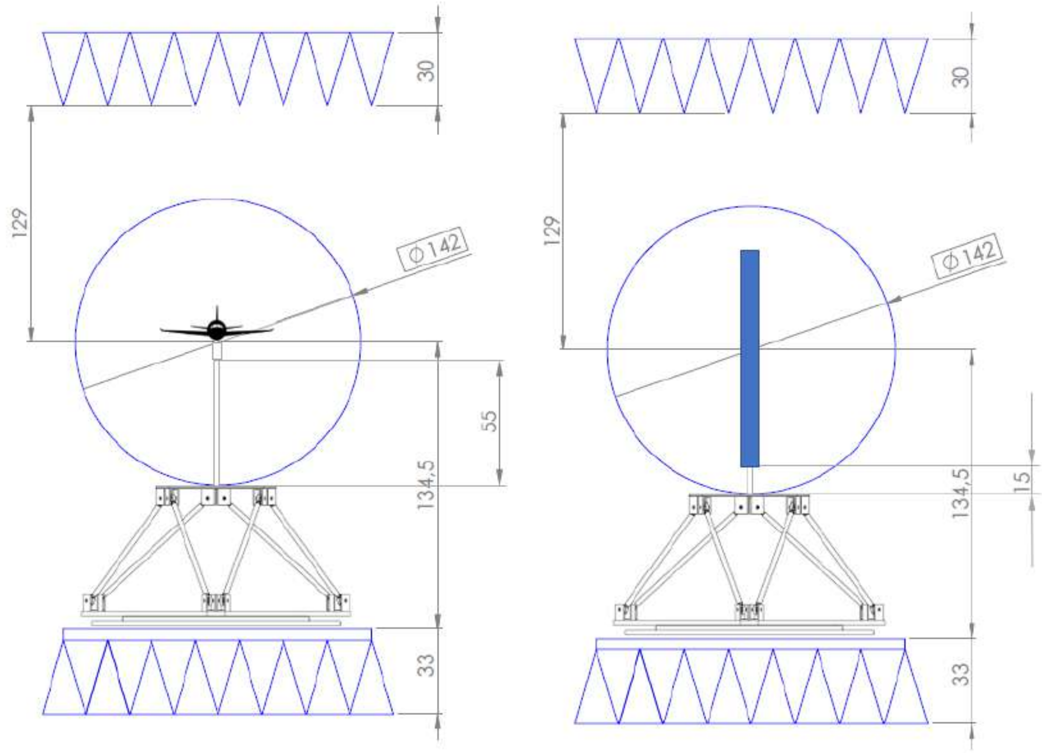

(a) Aircraft models setup

(b) Half-wing models setup

Figure 4.5: Schematic representation of the force balance positioning in the wind tunnel

Another important factor that needs to be taken into consideration is the fact that the model is supposed to be placed in the center of the wind tunnel test section and, for this reason, it is necessary to guarantee that the strut has an appropriate height. At this point, we will be considering two different approaches, one for each testing model (half wing or full plane). In the case of the half wing models, considering the test section radius ($71\ cm$) and the possible dimensions for the model and the connectors, a height of $55\ cm$ represents a good option. The placement in the wind tunnel and, more precisely, the positioning of the strut are depicted in figure 4.5(a), where all the presented dimensions are in centimetres. In the case of half wing models, these will be placed vertically in the wind tunnel, being the half span the vertical length. In order to benefit from the maximum available area of the test section, it does not make sense to use a strut as long as used previously and, for this reason, we will consider a $15\ cm$ long strut as represented in figure 4.5(b).

Regarding the preliminary model of the force balance, presented in figure 4.1(a), an issue rises up when the maximum set of loads and moments is applied, since large and inadmissible angular displacements are verified in the strut. In this case, the strut is made of an aluminium alloy (Al 6063-T6) and presents an external diameter of $20\ mm$, an internal diameter of $16\ mm$ and, as referred previously, a length of $550\ mm$. As for the flange, it is a $8\ mm$-thick metallic disc with a diameter of $100\ mm$. The external face of the strut is connected to the center of the flange where a hole with $20 mm$ of diameter was made. The simulation was performed assuming that these two entities are perfectly bonded together.

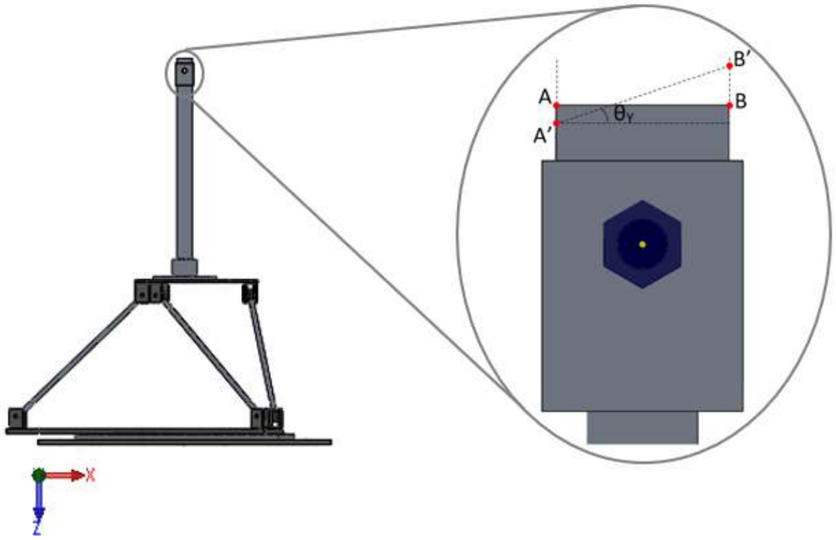

Figure 4.6: Schematic representation of rotation θ_Y at the top of the force balance

Figure 4.6 shows the mechanism that will be used to adjust the angle of attack that corresponds to the top of the force balance where the models are supposed to be attached. In order to fulfil the rotation requirements that were established previously in section 3.2.3, it is necessary to understand the way the structure will be deformed whenever a set of loads and moments is applied and how this deformation will affect the angular displacement. In order to measure the angle (θ_Y) it is necessary to consider the two middle points of both extremities of the mechanism (points A and B, in the figure). Considering an arbitrary set of loads and moments applied, both points A and B suffer a vertical displacement and change their position to A' and B', respectively. This vertical displacement can be translated into a rotation in Y-axis that will directly affect the aerodynamic angles of the model and so, the range of loads and moments that were supposed to be obtained. Considering the length of the mechanism (*l*), the angle (θ_Y) can be calculated as $\theta_Y = \frac{\Delta}{l}$, where Δ stands for the resultant vertical displacement calculated as $\Delta = |\delta_A - \delta_B|$ For the maximum load range for the plane model and for the half wing model and considering the force balance design previously presented, one obtains the values represented in table 4.1.

Table 4.1: Rotation θ_Y at the top of the force balance

	δ_A $[mm]$	δ_B $[mm]$	Δ $[mm]$	θ_Y [rad]	θ_Y [°]
Aircraft model	1.10×10^{-1}	-1.33	1.44	0.046	2.65
Half-wing model	1.82×10^{-1}	-2.95×10^{-1}	0.48	0.015	0.88

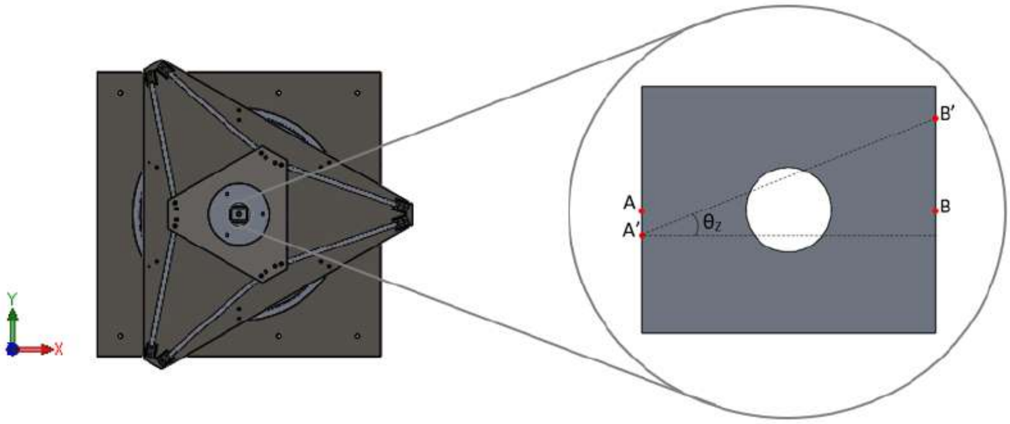

Figure 4.7: Schematic representation of rotation θ_Z at the top of the force balance

A similar way of thinking has to be considered in order to measure the rotation with respect to the Z-axis. The schematic representation of the displacements at the extremities of the mechanism is represented in figure 4.7. Using the same variables considered for the analysis of the rotation in Y-axis and applying the same loading conditions, one obtains the results presented in table 4.2.

Table 4.2: Rotation θ_Z at the top of the force balance

	δ_A $[mm]$	δ_B $[mm]$	Δ $[mm]$	θ_Z [rad]	θ_Z [°]
Aircraft model	5.81	5.88	0.07	0.002	0.13
Half-wing model	16.1	15.0	1.10	0.036	2.05

Analysing both tables 4.1 and 4.2, it is possible to conclude that for the θ_Y rotation, the critical situation corresponds to the plane model testing while for the θ_Z rotation, the critical situation corresponds to the half-wing model testing, as these values are above the maximum values of rotation defined in table 3.11 thus failing to meet the requirements. In order to fulfil the angular displacement specifications, it is necessary to test the solutions with each of the critical conditions.

One possible solution to decrease the values of rotation is to modify the shape of the flange. Rotation in Y-axis is due to bending phenomena that takes place in the edges of connection of the strut and the flange. A smoother transition may be useful to diminish these undesired displacements to acceptable values. Figure 4.8 shows the previous flange (a)) and the newer one (b)) where it is visible the smoother transition from the direction of the strut to the direction of the platform.

Considering this new flange and the same configuration for the strut, it is possible to come up with an analysis on the values of rotation, as represented in table 4.3. One can verify that the new is not very efficient at decreasing the values of rotation and, in some cases, the value has even increased. For this reason, and taking also into consideration that the new flange is heavier thus increasing the weight

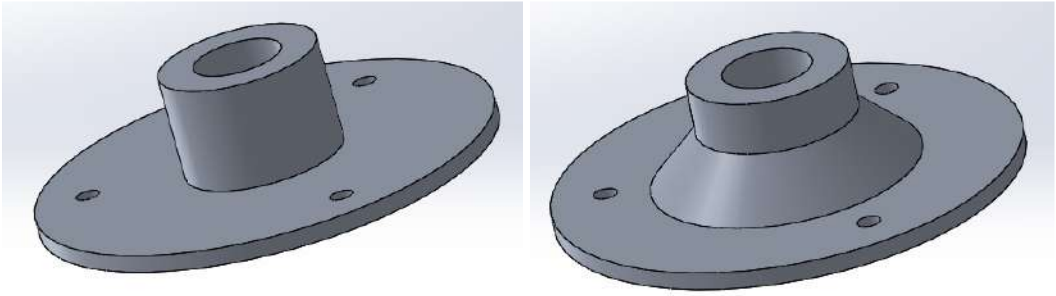

(a) Preliminary design (b) Adapted design

Figure 4.8: Flange solutions

above the extensometers, this solution was disregarded.

Table 4.3: Interference of flange design in the expected rotation of the structure

		θ_Y [°]	θ_Z [°]
Preliminary design	Aircraft model	2.65	0.13
	Half-wing model	0.88	2.05
Adapted design	Aircraft model	2.62	0.13
	Half-wing model	0.90	2.05

Another possible solution to overcome this issue is to change the cross section of the bar, that is, reducing or increasing the internal and external diameters. For the sake of construction simplicity, only standard cross-sections will be considered has an option. Table 4.4 shows the different possibilities and the respective results and the presented values of mass correspond to the weight of the strut in the aircraft model analyses.

Table 4.4: Influence of the strut design on θ_Y and θ_Z rotations

Strut Design			Aircraft Model		Half-Wing Model	
External Diameter [mm]	Internal Diameter [mm]	Mass [kg]	θ_Y [°]	θ_Z [°]	θ_Y [°]	θ_Z [°]
20	16	0.168	2.65	0.13	0.88	2.05
25	20	0.262	1.35	0.05	0.58	1.05
30	22	0.485	0.81	0.02	0.45	0.60
32	20	0.728	0.68	0.01	0.41	0.48

It is possible to conclude that, increasing the external diameter of the strut is a good strategy to decrease the values of rotation. However, the maximum pre-established values of rotation of $0.5°$ defined in table 3.11 are yet to be achieved. Another strategy will be carried out to decrease the values of rotation and even linear displacement as, as it is shown in table 4.2, in the case of the test with half wings, the displacements are considerably above the maximum value of $10\,mm$ defined in table 3.11, even for the remaining strut dimensions, this value continued to be slightly above this limit. This strategy consists in decreasing the height of the strut, in both cases: let us consider, for the aircraft testing, a strut with a height of $400\,mm$, and, for the case of half-wings, a strut with $130\,mm$ will be considered. This last value was harder to get, since the model has to be kept outside of the mixing layer. Considering the total length of the strut with the support that is around $190\,mm$, this was found to be an adequate length for clearance. Table 4.5 shows the new results, considering the same strut cross sections, but for the new values of height. Once again, the values of mass correspond to the height of the strut with $400\,mm$ of length.

Table 4.5: Influence of the new strut design on θ_Y and θ_Z rotations

Strut Design			Aircraft Model		Half-Wing Model	
External Diameter $[mm]$	Internal Diameter $[mm]$	Mass $[kg]$	θ_Y [°]	θ_Z [°]	θ_Y [°]	θ_Z [°]
20	16	0.122	1.53	0.09	0.74	1.77
25	20	0.191	0.82	0.04	0.52	0.92
30	22	0.353	0.53	0.02	0.39	0.56
32	20	0.529	0.46	0.01	0.41	0.46

One can conclude, by comparing tables 4.4 and 4.5 that decreasing the height of the strut was the solution to fulfil the requirements of rotation presented in table 3.11. In this case, the strut cross section has an external diameter of $32\,mm$ and an internal diameter of $20\,mm$ and a length of $400\,mm$ for the case of aircraft models testing and $130\,mm$ for the half-wing testing.

Considering this flange and strut, a maximum displacement of $8\,mm$ happens at the tip of the strut, which is below the maximum limit for displacement defined in section 3.2.3.

It is important now to describe the design process of each component, not only in terms of shape and dimensions but also in terms of materials and mechanical properties. The results of the simulation will also be presented and discussed for each component in order to assess the structural integrity of the whole structure.

4.2.2 Fixed Platform

Starting with the fixed platform at the bottom of the structure, the main aspects one needs to consider are the platform thickness and the location of the holes to mount the rod end bearings couplers and the sideslip angle adjustment mechanism.

Concerning the thickness of the platform, it has to be significant since it is also going to help providing support of the whole structure, since this part is to be placed below the strain gauges and so its weight does not interfere with the measurements being possible to take advantage of this fact. The best way to guarantee this last factor is to choose a resistant metal with high density although relatively easy to acquire and cut to the desired shape. Steel was found to be the best option. Giving the average density of the steel (around $7860\,kg/m^3$), and the desired shape, it is possible to relate the mass of the fixed platform with its thickness. Considering a thickness of $10\,mm$, the weight of this platform is found to be around $16.4\,kg$. The 3D model of this part is represented in figure 4.9.

Although, theoretically the greater the mass of the platform the better the support of the balance, there are limitations concerning the maximum thickness. Since the material to be used (steel) is extremely dense, the techniques to cut the initial sheet metal to obtain the required shape depend greatly on the thickness. The most widely used cutting methods are oxy-fuel, plasma, laser or waterjet and the selection is mostly based in the thickness of the plate and on the desired edge quality. Generally, water-

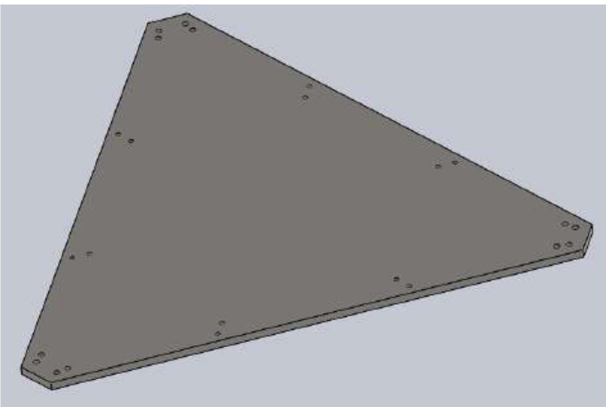

Figure 4.9: $3D$ model of the fixed platform

jet cutting offers higher accuracy and edge quality thus being a more expensive procedure. Moreover, the greater the thickness the more expensive the shaping will be since not only the initial sheet metal is more expensive but also the cutting process can be more demanding.

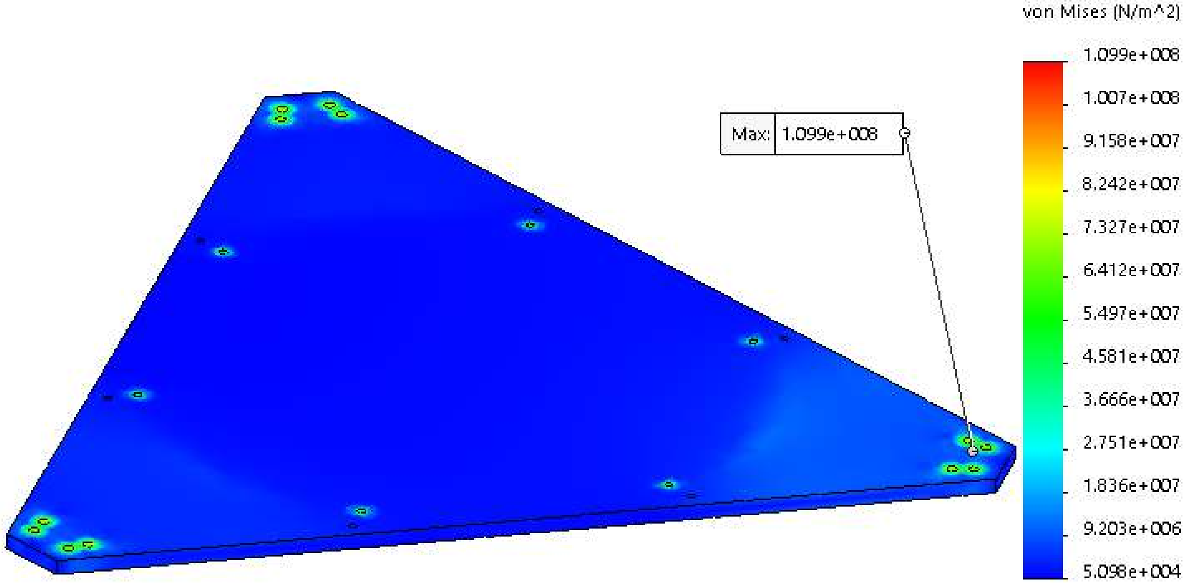

Figure 4.10: Fixed platform - loading simulation results

Considering the maximum expected loads and moments, it is possible to carry out a simulation and evaluate the behaviour of this part when subjected to such conditions. This part can be isolated from the other components and analysed separately, as shown in figure 4.10. This platform was considered to be made of a specific type of structural steel (1.0037) that yields at $235\ MPa$. By observing the figure, one can see that the maximum stress value is slightly below $110\ MPa$ and so, yielding does not occur.

4.2.3 Sensing Bars

Cylindrical bars will connect both platforms and are supposed to axially carry all the loads. Since the bars present a simple shape, the best solution was to search for the available possibilities in hardware stores. These stores sell a wide variety of bars, with different cross-section shapes, different dimensions and different materials.

Starting with the material, these bars are usually available in steel and aluminium. Considering the *Yield Strength* (σ_Y) of both materials, after which the deformation starts to be plastic instead of elastic, and comparing them, it is possible to elect the best option. General hardware stores usually sell cold rolled steel (DIN EN10130) and stainless steel that present values of *Yield Strength* of around $200\ MPa$ to $300\,MPa$, depending on the production methods, as for the aluminium alloy, the most common type for rods is the *6061-T6* which present a typical value of around $275\,MPa$ for *Yield Strength*. Considering two bars with similar cross sections and the materials previously referred, the choice lies on aluminium alloy, since it is capable of supporting high load values while being less dense; the bars will be lighter, thus reducing the weight of the structure that is above the ground and has to be taken into account during the calibration process.

Regarding the cross section, it can either present a squared or a circular shape. To guarantee a uniform deformation of the bar, both in axial and in the cross-section directions and in order to simplify the coupling of the ball joints, the circular shape was chosen. Moreover, the bar can be solid or instead a circular tube. For the same value of loading and since $\sigma = \frac{F}{A}$ (where F stands for the axial force and A for the cross-sectional area), the circular tube will present higher deformation since the cross-sectional area is smaller when compared to the solid one and thus the stress is higher. It is important to remind that $\sigma = E\epsilon$, where E stand for the *Young's Modulus*, in Pa and ϵ stand for strain, and since in both cases the material is the same, the higher the stress, the higher the deformation.

One can see that choosing between hollow and closed section bars will greatly affect the load carrying capability of the force balance. For instance, if we consider a bar with a 10 mm diameter closed cross-section and another with hollow section with $10\ mm$ of outer diameter and $8\ mm$ of inner diameter subjected to the same axial loading condition, the stress for the bar with closed-cross section will be about 36% of the stress for the bar with the hollow cross section. Regarding this fact, it would be expected that one would choose the bar with closed cross-section. However, this solution brings up a relevant issue: for the same loading conditions, it will be needed more sensitive extensometers as the strain values are smaller; on the other hand, the bars with closed cross-section are heavier and their weight may interfere more with the strain gauges readings.

A simultaneous market research on stock aluminium bars and rod end bearings led to choose aluminium bars with $10\,mm$ of outer diameter and $7\,mm$ of inner diameter, the adequate dimensions to drill the internal M8 screws on both extremities. The $3D$ model of the sensing bar is represented in figure 4.11.

When the maximum load case is applied, the range of stress varies with each bar. Considering and isolating the bar where the stress was found to be highest, it was possible to find its normal stress as it can be seen in figure 4.12(a). It can be verified that the maximum stress value is slightly below $24\ MPa$, in module, which is considerably less than the yield strength of the considered aluminium that is $275\ MPa$. This value of normal stress is of particular importance as it will be used to assess the structural integrity of the rod end bearings.

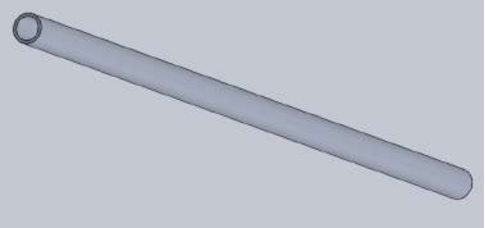

Figure 4.11: $3D$ model of the sensing bar

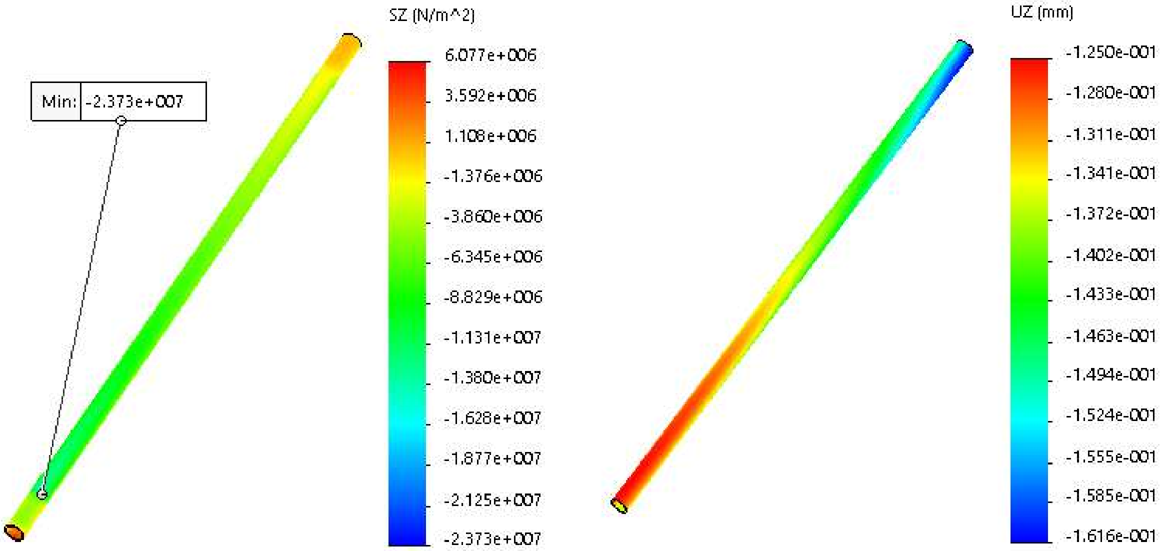

(a) Maximum expected normal stress

(b) Expected axial displacement

Figure 4.12: Sensing bars

Figure 4.12(b) shows the expected range of axial displacements that the bar is expected to sense when the maximum load range is applied. These values of deformation are the ones that will be measured by the strain gauges and taken into consideration during the calibration process. As can be observed the maximum expected range of displacement presents an order of magnitude of around $10^{-1}mm$, with values varying from $0.125\,mm$ to $0.162\,mm$, in absolute value.

The values of strain at the bars are also very important as they are going to be measured by the strain gauges and so, one has to guarantee that the maximum admissible value of strain measured by the gauge includes the range of strains that are expected to occur in the bars. These comparative analysis will be performed further in section 5.1.

4.2.4 Rod End Bearing

Since it is supposed to measure the deformation of the sensing bars in their axial direction, it is essential to guarantee that the bars will only deform in this way. To do so, rod end bearings will be coupled to both extremities of each bar. This mechanism will allow the force balance to move freely except in the axial directions of the bars and each loading condition will be translated to a certain combination of deformation distribution in each bar.

In general, one can have three different types of rod end bearings: with male thread, with female thread or with a welding shank. To guarantee the modularity and the simplicity of parts replacement of the force balance, the last solution is excluded. It is relatively easy to internally thread each bar in both extremities and so use rod end bearings with male threads. To guarantee a more efficient assembly of the bearings in the bars, an effective solution was to use different directions for the threads in both extremities, that is, in one of the extremities it is used a rod end bearing with a left male thread, and in the other extremity it is used an equivalent rod end bearing with a right male thread, being the internal threads in the bars done accordingly. This solution prevents eventual unscrewing phenomena as rotating the bar in a certain direction will cause the same result in both joints, being possible to tighten this connection by fixing the rod end bearings and rotating the bar in one direction.

To choose the sensing bars and the rod end bearings, it had to be taken into account the internal diameter of the bars and the dimension of the male thread. Given this, rod end bearings with a M8 male thread were found to be the best solution. After considering the available brands provided by different suppliers and analysing the relation between cost and benefit, the choice fell on rod end bearings by *INA/FAG*, **GAL8-UK** for the rod end bearing with left male thread and **GAR8-UK** for the rod end bearing with right male thread represented in figure 4.13.

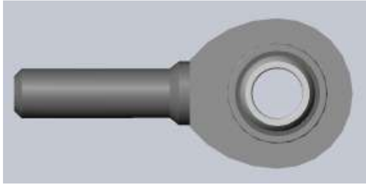

Figure 4.13: *3D* model of the selected rod end bearing

The referred rod end bearings satisfy the norm **DIN ISO 12 240-4** that specifies dimensions, tolerances and radial internal clearances for several dimensions of spherical plain bearing rod ends.

The rod end bearing is made of three main parts: the housing, the inner ring and the outer ring to which the contact pair is connected. The function of the contact pair is to avoid lubrication processes since these are maintenance-free rod end bearings. The rings and the housing are made of a drop forged quenched and tempered steel (C45 QT - material no. 1.0503) and have a zinc coated surface. As for the contact pair, a surface of hard chromium is coated with a PTFE plastic composite with sintered bronze.

This specific type of rod end bearing is capable of support a maximum dynamic load (C_r) of $5850\ N$ and a maximum static load (C_{0r}) of $12900\ N$. As referred previously, the maximum normal stress of the bar is important as this value can be used to obtain the maximum axial force value and compare it to the rod end bearing specifications. Considering the cross section area of the bar and the stress value, and using the expression $\sigma = \frac{F}{A}$, one can obtain the results depicted in table 4.6.

Table 4.6: Rod end bearing integrity

Normal Stress (σ) [Pa]	External diameter [m]	Internal diameter [m]	Cross-section area [m^2]	Axial force [N]
2.373$\times 10^7$	0.010	0.007	1.60$\times 10^{-4}$	3802

The value of axial force leads one to conclude that the maximum range of forces and moments can be applied without compromising this part as it is smaller than the static load limit of the rod end bearing ($12900\,N$). It is important, however, to analyse the subassembly of the bar coupled with the rod end bearings and guarantee that the maximum expected loads can be applied without bringing up any issues. Using the *CAD* models provided by the supplier and applying the materials mentioned previously, it is possible to run an analysis and obtain the results presented in figure 4.14 that shows that the maximum stress value occurs in the region of the bearing housing. However, this piece is made of a steel that yields at $580\,MPa$ which is greater than the maximum obtained stress value of $64.68\,MPa$.

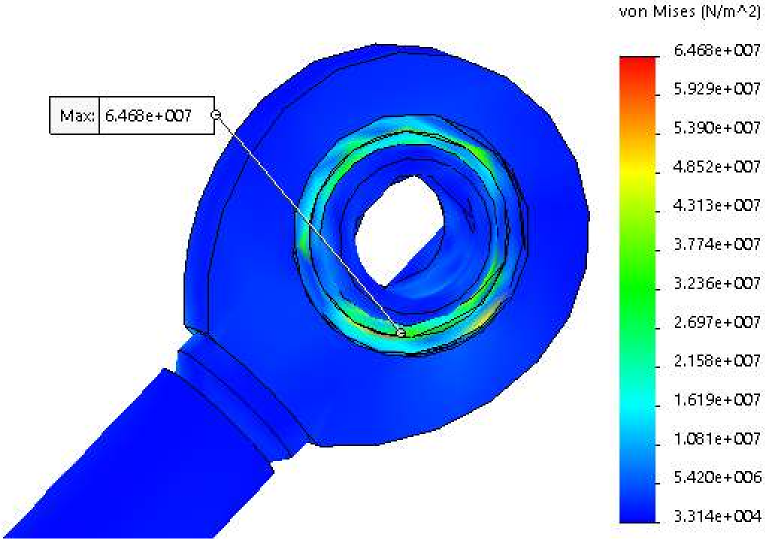

Figure 4.14: Bar and rod end bearing stress simulation

4.2.5 Moving Platform

The moving platform is very similar to the fixed platform described previously and, for this reason, its design will also be similar. The planform area of the platform can be obtained by subtracting to the triangle with $350\,mm$ of side the three triangles with $60\,mm$ of side that correspond to the factor αa.

Regarding the material and after many considerations, the conclusion was that the same steel used for the fixed platform even with a smaller thickness would be very heavy and interfere with the measurements of the sensing bars. The main aspect one has to take into consideration is the weight of this moving platform: since it will be placed above the extensometers, it will add a contribution to the measured loads that need to be taken into account in the calibration process in order to obtain the real loading values. One way to overcome this issue is to have a light material. The stiffness is also very important since one is expecting that the deformations occur only on the sensing bars and not on the moving platform. This reason justified the use of a carbon fibre composite panel as it presents high stiffness and, as required, very low density when compared to the base platform.

As for the material and considering the necessity of having a light-weight structure above the sensing bars, a composite sandwich panel was selected as it is already being used in the Aerospace Engineering's Laboratory for several works. It consists of a sandwich panel with a hard foam core and face sheets of a carbon fibre composite. The core provides light-weight structural integrity while the carbon fibre/epoxy faces provide both high stiffness and strength. The set of properties of this sandwich is represented in table 4.8. Figure 4.15 represents the laminate layup. The grey layers represent the carbon-fibre/epoxy resin composite face sheets and the darker lines the different orientations of their fibres and the thicker central layer stands for the hard foam core. It is important to highlight that the laminate is assumed to be perfectly symmetric not only in terms of thickness but also regarding the orientation of the fibres in both sides of the core. Additionally to the orientation, the thickness of each layer is also represented.

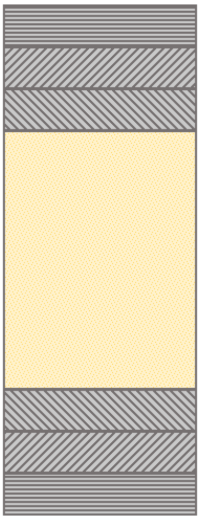

	Material	Thickness $[mm]$	Orientation [°]
1	Carbon-Fibre/Epoxy	0.8	0
2	Carbon-Fibre/Epoxy	0.8	45
3	Carbon-Fibre/Epoxy	0.8	-45
4	Foam	5	-
5	Carbon-Fibre/Epoxy	0.8	-45
6	Carbon-Fibre/Epoxy	0.8	45
7	Carbon-Fibre/Epoxy	0.8	0

Figure 4.15: Schematic representation of laminate layout

Similarly to what was done to the base platform, the simulation will be carried out assuming that the maximum loading range is applied and the results were obtained by isolating this specific part. The result of this simulation in terms of maximum stresses and deformation is represented, respectively, in figures 4.16(a) and 4.16(b).

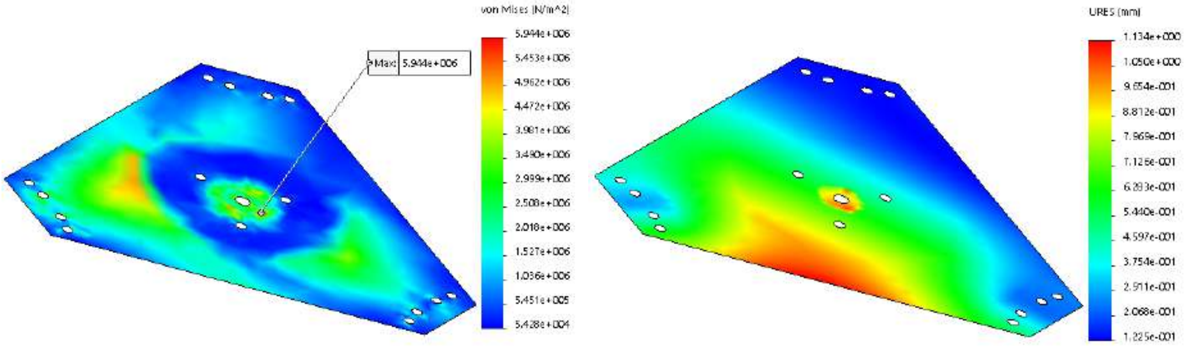

(a) Stress analysis

(b) Deformation analysis

Figure 4.16: Upper platform

The carbon fibres provide the necessary strength to the upper platform, allowing it to support the range of loads and moments applied without compromising its integrity or deform permanently. It can be seen that the greater values of stress take place in contact regions between different components., where load transferring occurs. Regarding the total deformation, figure 4.16(b) allows us to see that the deformation values present an order of magnitude from 10^{-1} to 10^{0} varying between $0.123\,mm$ to $1.134\,mm$.

4.2.6 Coupler

In order to link the sensing bars and the rod end bearings to both platforms, a metallic coupler was projected. This metallic piece will be screwed to the platforms and the rod end bearing will be attached to it by means of steel rods and breaks. This link mechanism will be made of steel, like the base platform, by bending a sheet metal into a *U*-shaped piece with a thickness of $3\,mm$, as represented in figure 4.17(a). This thickness was obtained by considering the maximum load ranges that are expected to take place in the experiments. It is possible to isolate the coupler where the maximum stress range takes place and analyse the expected stress values that are represented in figure 4.17(b). Comparing the maximum expected stress $(110.2\ MPa)$ to the yield strength of the considered Alloy Steel $(\sigma_Y = 620\ MPa)$, it is possible to verify that the former is below the latter and so one can conclude that the structural integrity of this piece is guaranteed since it won't deform permanently.

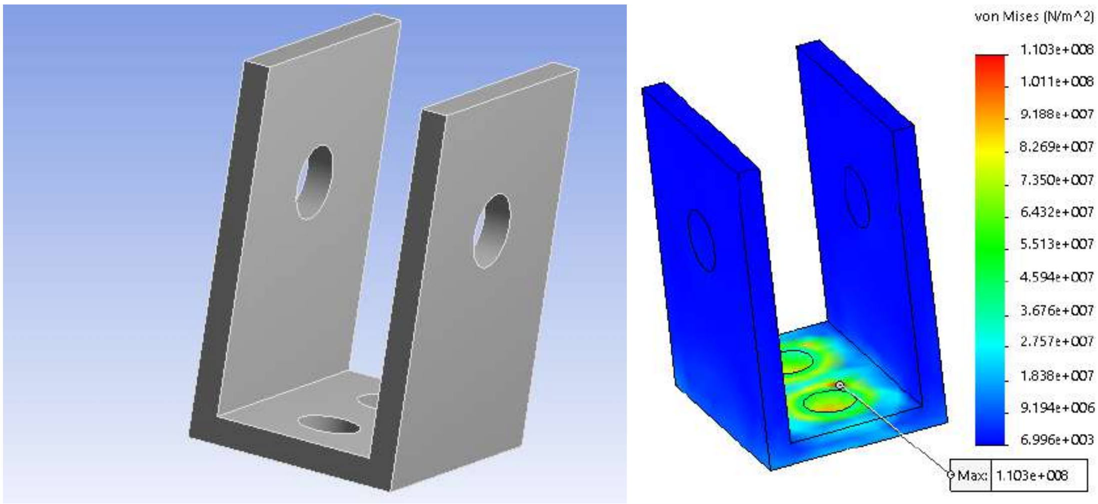

(a) *3D* model

(b) Stress analysis

Figure 4.17: Coupler

The set of components presented until this point can be seen as the skeleton of the force balance however several members have to be added in order for it to become fully functional. For instance, a vertical strut has to be attached to the center of the upper platform, by means of a metallic flange, and be used as a pole to support the model to be tested. A carefully detailed study on the attaching mechanism has to be carried out in order to prevent bending phenomena.

4.2.7 Sideslip Angle Adjustment: Rotating Platform

As said previously in section 3.3, it is necessary to implement a mechanism that allows the user to choose the adequate sideslip angle to the experiment. This rotating mechanism will be attached to a fixed rectangular shaped $10\,mm$ thick steel plate which, in turn, will be connected to the ground. This steel plate will present a graduated scale that will allow the user to rotate the force balance structure and thus choose the desired β angle.

The best solution for the rotating mechanism was found to be a bearing rotary table, as depicted in figure 4.18(a), as it presents a higher robustness and is able to support greater loads, however, its range of prices is prohibitive.

(a) Rotary table bearing (cutted view) (b) Rotating collar

Figure 4.18: Rotating platforms

Given this fact, a cheaper and more ordinary option had to be considered. Figure 4.18(b) shows a solution that costs less than 20 times than the first one, and although it has a smaller loading capacity, it is still a valid option for this purpose.

Figure 4.19 represents the results of the stress analyses of the subassembly formed by the rotating mechanism and the steel table. The maximum stress ($74.88\,MPa$) occurs in the vicinity of the holes that connect the rotary collar to the force balance structure itself, however this value is below the yield strength of the aluminium alloy that the rotary collar is made of ($\sigma_Y = 325\,MPa$) and the steel that composes the table ($\sigma_Y = 235\,MPa$).

4.2.8 Angle of Attack Adjustment

In order to adjust the angle of attack, a new mechanism has to be designed. A very important aspect has to be taken into account as α and β angles have to be decoupled in order to eliminate interferences between them, that is, the adjustment of both angles has to be mechanically separated. For this reason, the setting of α will be conducted at the top extremity of the force balance by means of an adjustable hook. At the top of a strut, a U-shaped metallic support will be welded. Another similar metallic component will be attached to it by means of bolted connections which can be adjusted and tighten to the desired angle of attack, as depicted in figure 4.20(a).

This piece is made of aluminium Al 2024-T4 which has a yield strength of $325\,MPa$ and, as can be seen in figure 4.20(b), the maximum value of stress in the mechanism is around $5.75\,MPa$ which is far below the first yielding value.

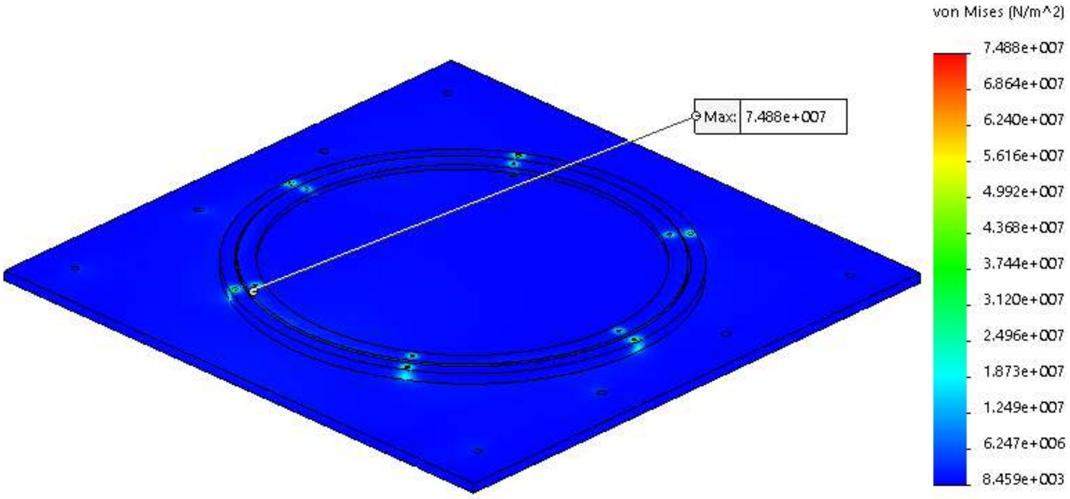

Figure 4.19: Rotary collar and table stress results

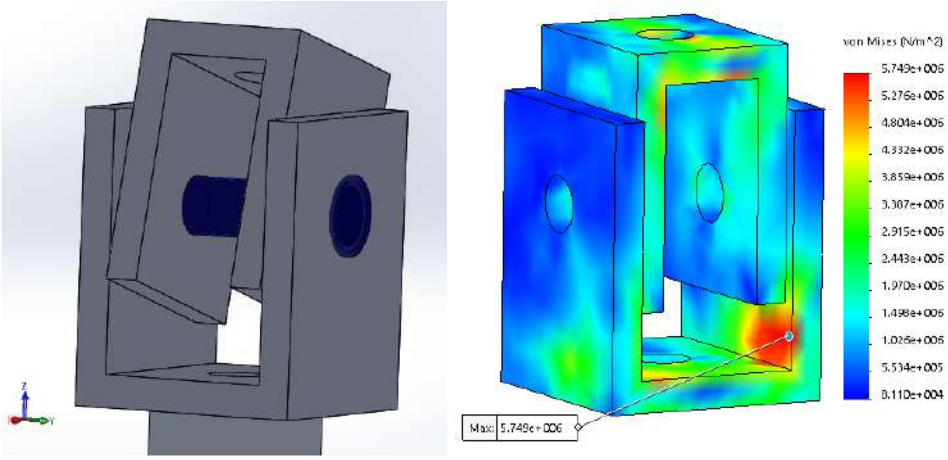

(a) Geometry and connections

(b) Stress distribution

Figure 4.20: Angle of attack adjusting mechanism

4.2.9 Complete Assembly

It is important to refer that as the components were being described through the last sections, the stress results of the simulation were shown in order to analyse the behaviour of each component and guarantee its integrity during the operation of the force balance.

Figure 4.21 shows the exploded view of the whole structure of the force balance and identifies each component in the table below.

Table 4.7 shows the metallic materials that were selected for the main components of the force balance. However, the moving platform (item no. 4) is a laminate panel with a core of foam and face sheets of carbon-fibre/epoxy composite and, for this reason, this material is not isotropic as its properties vary with the orientation of the fibres. Table 4.8 details the properties of the laminate materials: the foam that forms the core of the panel and the carbon-fibre/epoxy resin composite that forms the faces of the panels.

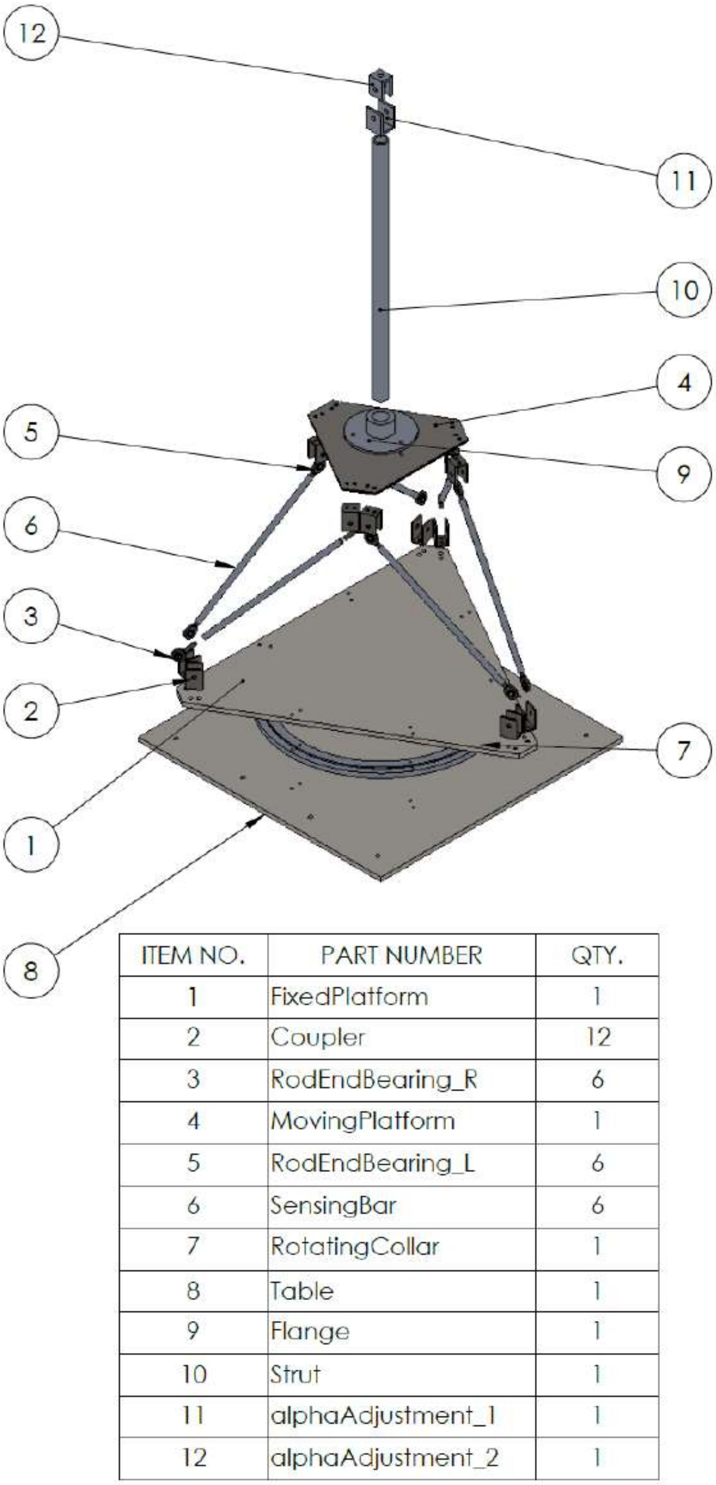

ITEM NO.	PART NUMBER	QTY.
1	FixedPlatform	1
2	Coupler	12
3	RodEndBearing_R	6
4	MovingPlatform	1
5	RodEndBearing_L	6
6	SensingBar	6
7	RotatingCollar	1
8	Table	1
9	Flange	1
10	Strut	1
11	alphaAdjustment_1	1
12	alphaAdjustment_2	1

Figure 4.21: Exploded view of the force balance model and identification of its components

4.3 Computational Structural Analysis

Now that all the components were presented, described and dimensioned, it is necessary to analyse the force balance behaviour for the test conditions that were presented previously, that is, the half wing model and the full aircraft model, for different sideslip angles, that correspond to the values represented

Table 4.7: Metallic materials used in the force balance

Material	Density ρ [kg/m^3]	Yield Strength σ_Y [MPa]	Young's Module E [GPa]	Item no.
Al 2024-T4	2780	325	72.4	7,11,12
Al 6061-T6	2700	275	69	6
Al 6063-T6	2700	215	69	7,10
Steel 1.0037	7800	235	210	1,8
Steel 1.0503	7800	580	210	3,5
Alloy Steel	7700	620	210	2
Brass	8500	240	100	3,5

Table 4.8: Moving platform laminate - material properties

	Carbon-fibre/epoxy [30]	Foam (ROHACELL© IG 71 [31])
Density [kg/m^3]	1600	75
Tensile Modulus [MPa]		92
Compressive Modulus [MPa]		73
Young's Modulus $0°$ [GPa]	70	
Young's Modulus $90°$ [GPa]	70	
Shear Modulus [MPa]	5000	29
Tensile Strength [MPa]		2.8
Compressive Strength [MPa]		1.5
Tensile Strength $0°$ [MPa]	600	
Compressive Strength $0°$ [MPa]	570	
Tensile Strength $90°$ [MPa]	600	
Compressive Strength $90°$ [MPa]	570	
Shear Strength [MPa]	90	1.3
Poisson's Ratio	0.10	

in tables 3.5 and 3.8, respectively.

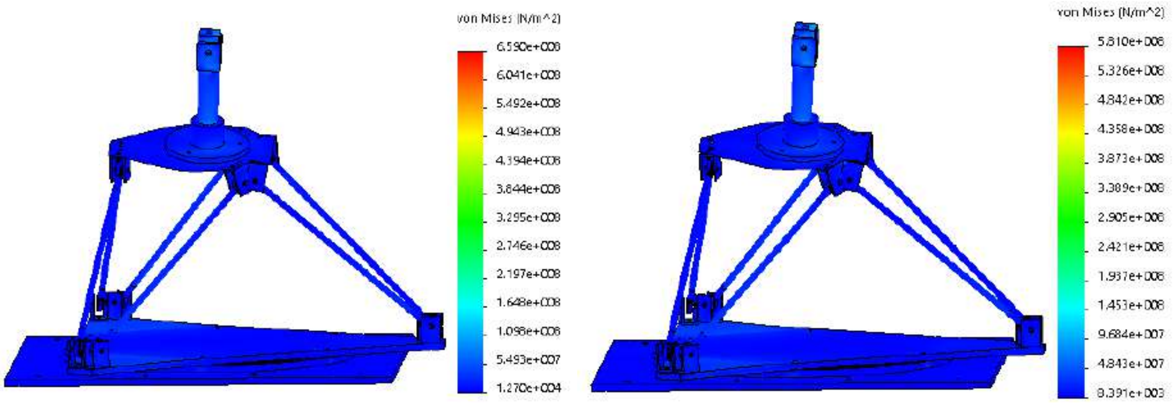

(a) $\beta = 0°$

(b) $\beta = 20°$

Figure 4.22: Half wing model - stress distribution (deformation scale - 8)

Figures 4.22(a) and 4.22(b) represent the stress distribution in the force balance while the associated load range for the half wing models represented in table **??** is applied. It is possible to verify that the overall maximum value of stress, around $659\ MPa$, occurs when $\beta = 0°$.

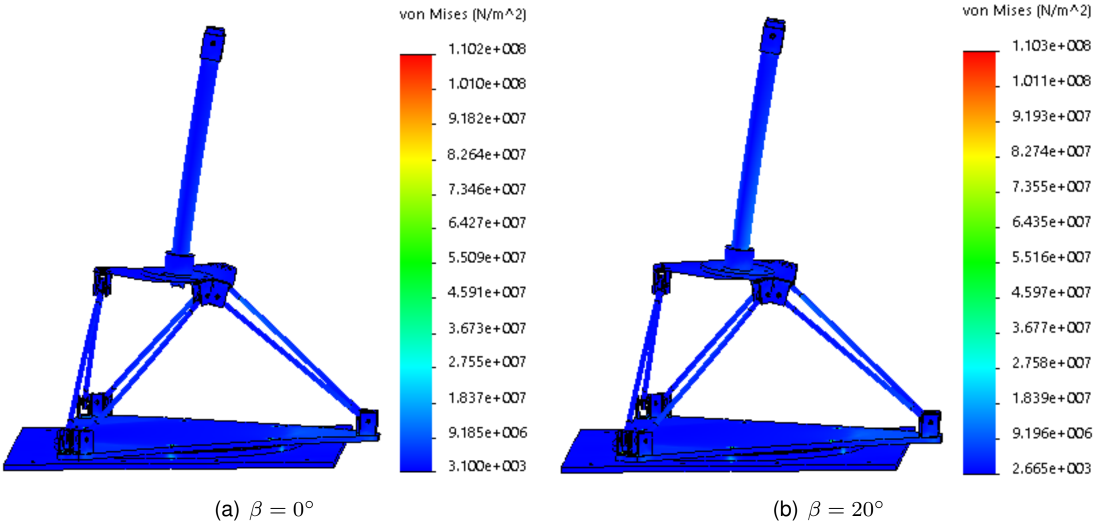

(a) $\beta = 0°$ (b) $\beta = 20°$

Figure 4.23: Full aircraft model - stress distribution (deformation scale - 38)

As for figures 4.23(a) and 4.23(b), they represent the stress distribution on the force balance while the associated maximum load range for the full aircraft model, represented in table **??**, is applied. Similarly, in this case, the maximum value of stress, $110.3\ MPa$ occurs when $\beta = 20°$.

Comparing both test scenarios, the half wing and the full aircraft, the maximum values of stress occur for the half-wing model. This makes sense as the order of magnitude for the expected values of forces and moments for the half-wing are substantially higher than the values of the aircraft model.

Chapter 5

Sensors and Instrumentation

After having designed and dimensioned all the mechanical parts of the force balance, it is important to select the sensors that have to be attached to the mechanism in order to determine the loading conditions. As discussed in section 2.3, it will be used *Wheatstone bridges* to fully instrument each bar, determine its deformation and thus obtain the loading conditions of the force balance. *Wheatstone bridges* are composed by four extensometers each whose deformation is translated in a voltage, that is the output signal and depends on the excitation voltage. However, the interest lies on obtaining the correspondent deformation which is obtained by using a *DAQ* - Data Acquisition System and a specific related software.

5.1 Strain Gauges

Concerning the extensometers, they have to be carefully chosen in order to guarantee an adequate operation. Since they are to be mounted in aluminium bars, the extensometers specifications have to guarantee good results when attached to aluminium pieces, since mainly, one can found extensometers to be attached to aluminium or steel.

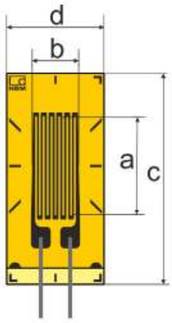

Figure 5.1: Schematic representation of the strain gauge to be used [32]

The second important aspect that has to be taken into account is the dimension of each extensometer since they have to be attached to an aluminium bar with $10\,mm$ of outer diameter, that corresponds to a perimeter of around $31.42\,mm$. Figure 5.1 represents, schematically, a strain gauge extensometer and its characteristic dimensions. The greater dimension c has, of course, to be smaller than the perimeter of the bars in order to be attached to it. However, if this dimension is too small, it will be difficult to manipulate this components, attach them to the bars and wire them. The solution is to find an available strain gauge whose dimension is a good compromise between these two conditions. Given so, the chosen extensometer has $c = 13\,mm$ and $d = 6\,mm$.

Another important aspect lies on the type of connection to the wires. For this type of strain gauges, there are, mainly, three types of possible wirings that are to be considered for this specific application: pre-wired strain gauges, strain gauges with integrated solder pads beneath the measurement grid and strain gauges with leads beneath the measurement grid. All these alternatives present pros and cons and the final cost is highly dependent on this characteristic. Ideally, the best option would be the pre-wired strain gauges since it would simplify the assembling process and the linkage to the data acquisition system, however, this solution is very expensive. The cheaper solution is the strain gauge with integrated solder pads, however, this welding process is hard and requires extremely high precision. Given this, the best solution was found to be the strain gauges with leads, since they are cheaper than the pre-wired ones and easier to operate when compared to the strain gauges with solder pads.

Considering all the specifications referred previously, the following extensometer was selected: **1-LY13-6/350** by HBM. The first digits *1-LY1* refer to the type of extensometer, in this case *L* stands for linear, *Y* stand for universal foil strain gauges for stress analysis and *1* stand for the type of wiring in this case with leads beneath the measurement grid. The next digit *3* refers to the material in which the extensometer is supposed to be attached, in this case aluminium. The last two numbers *6* and *350* represent, respectively, the measuring grid length, in milimeters, and the nominal resistance, in Ω. This value was found to be the best option, after analysing the specifications of the data acquisition system related with the full bridge inputs and excitation voltages [33].

Since the extensometers are supposed to be attached to the sensing bars, it is necessary to guarantee that they are capable of measuring the range of deformations that the bar is expected to have, both in axial and tangential directions. These two deformations are particularly important given the way that the extensometers are supposed to be attached to the sensing bars. As referred previously in section 2.3.1, in order to maximize the measuring efficiency of the strain gauges, they will be connected as *Wheatstone* bridges where one pair of strain gauges will be measuring the axial deformation of the bar and the other pair will be measuring the tangential displacement of the bar. It is important, also, to note that when one of the pairs is in tension the other is in compression.

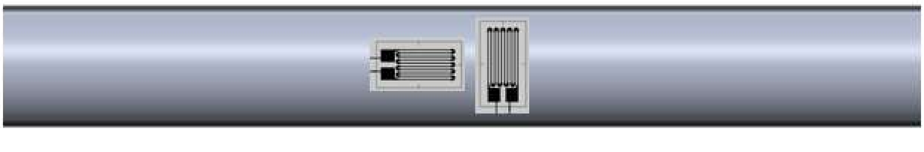

Figure 5.2: Schematic representation of the strain gauges attachment to the sensing bars

Figure 5.2 shows how the strain gauges are supposed to be attached to the sensing bar in order to form the *Wheatstone* bridges. In the figure, only the front view of the bar is represented but two more strain gauges are attached in the back in a similar manner so that, in the end, there will be two strain gauges aligned with the axial direction and another two perpendicular to it.

Considering the selected strain gauges, their maximum elongation (ϵ_{max}) is $50000\ \mu m/m$, that is 5×10^{-2}, and so it must be guaranteed that, for all the critical loading conditions presented previously, the sensing bars do not deform (both axially and tangentially) past this value of strain. Table 5.1 presents the maximum expected values of strain for the critical loading conditions at the middle of the bars, where the strain gauges will be attached, as depicted in figure 5.3. It is possible to see that the range of values is below the maximum admissible value of strain for this type of strain gauge ($50000\ \mu m/m$) and so, they can be used to measure the values of strain in the bars for all the operating conditions.

Table 5.1: Maximum absolute values of microstrain in the bars for the maximum expected loading conditions

Maximum micro-strain values ($\mu m/m$)	Axial	Tangential	Maximum Admissible
Plane model	105	34	50000
Half-wing model	395	130	

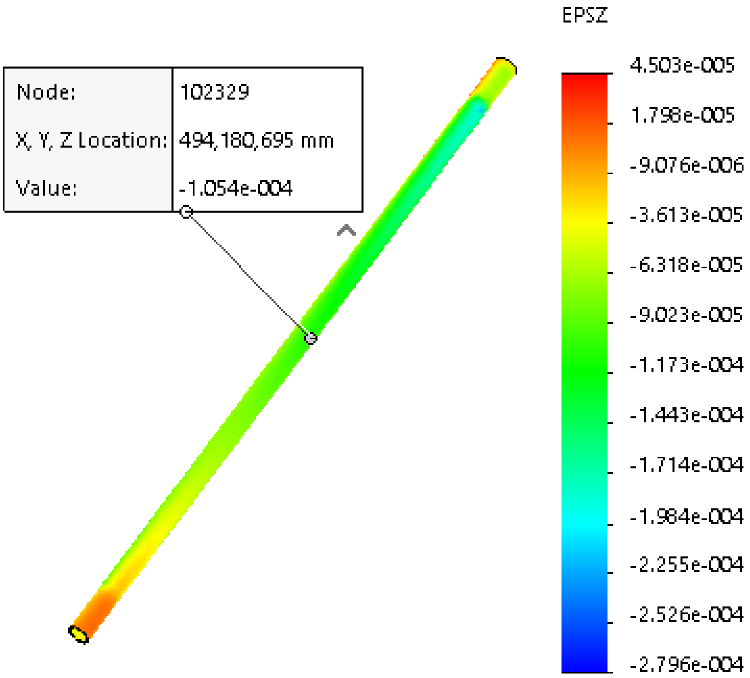
Node: 102329
X, Y, Z Location: 494,180,695 mm
Value: -1.054e-004

Figure 5.3: Strain measurement at the middle of the sensing bar

A first observation of the table 5.1 leads to conclude that the maximum expected values of microstrain are considerably below the maximum admissible value the strain gauge is capable of measuring. Based on these values, the issue that arises is that it is necessary to guarantee that the strain gauges have enough resolution to measure such small quantities as the maximum expected values of displacement are less than 1% of the maximum admissible elongation of the strain gauges. In fact, these sensors are highly sensitive and can be used to measure extremely low values of strain. A brief research showed that it is common for a strain gauge to have an extension of 0.1%, which corresponds to $1000\ \mu m/m$ and so one can conclude that the expected values are within this range [34]. In addition, the use of *Wheatstone* bridges compensates this effect as it would be extremely hard to quantify the change in the resistance of one isolated strain gauge when loaded.

5.2 Pitot Tube

Since there is already a Pitot tube attached to the wind tunnel and correctly calibrated and can be used to relate the true airspeed inside the wind tunnel with the frequency of operation of the wind tunnel fan. This relation was presented before in section 3.1. Then, it is possible to install another Pitot tube in the structure of the force balance to measure the true airspeed that the model is experiencing. This new Pitot tube can be calibrated by comparison with the true air speed of the calibrated Pitot tube [35]. An example of a Pitot tube that is mounted at the top of a wind tunnel can be seen in figure 5.4.

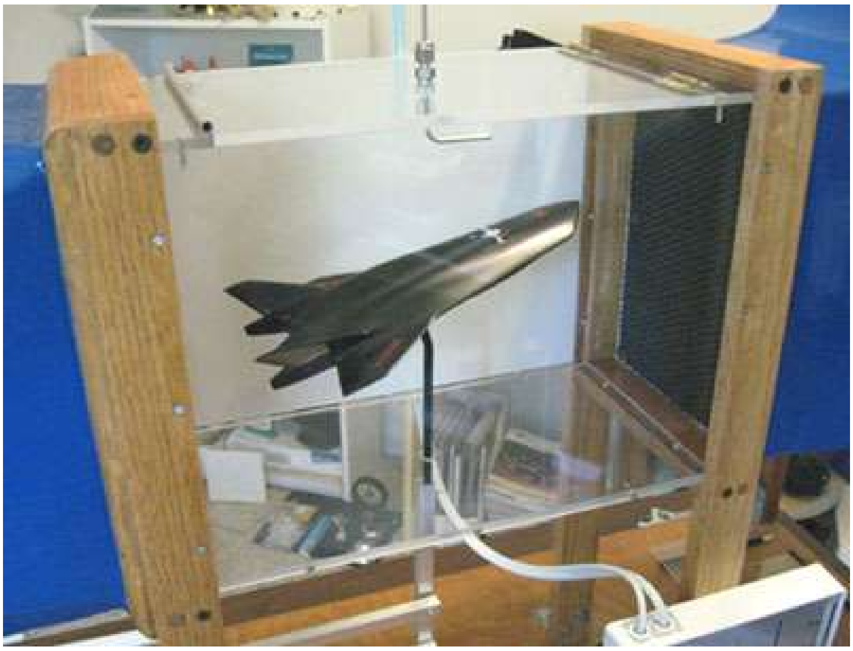

Figure 5.4: Wind tunnel with Pitot tube (AeroRocket)

5.3 Data Acquisition System (DAQ)

After having decided the most suitable type of extensometer for the force balance, it is necessary to find the equipment that is going to be used to transform the electrical output signal from the extensometers in a readable value of deformation. To do so, as referred before, a data acquisition system must be utilized.

This data acquisition system, commonly known simply as *DAQ*, has to be carefully chosen in order to be compatible with the extensometers selected previously. Considering the mounting mechanism of the extensometers, that are supposed to form *Wheatstone* bridges, one can search for this specification on the available options for data acquisition systems. In fact, there are systems that are specified to receive an input signal directly from *Wheatstone* bridges and then, the output signal is decoded in a computer software, and is possible to read all the deformation associated with each *Wheatstone* bridge.

Figure 5.5: Data acquisition device - *National Instruments*^{TM} NI 9237

The best solution was found to be a hardware from *National Instruments*^{TM} in particular the board *NI 9237* [36], shown in figure 5.5. This device is capable of measuring signals from either full, half or quarter bridges. It has 4 input channels which means that it is capable of measuring signals from 4 full bridges. Since the force balance has a total of 6 sensing bars, there are also 6 *Wheatstone* bridges. This means that, to fully obtain the loading conditions, it is necessary to have two of these systems of data acquisition.

Now that both extensometers and data acquisition system (DAQ) are selected, the connection mechanism between them must be clarified. Considering the data acquisition system, there are two possibilities that vary in the way the input is made (*DSUB* or *RJ50*). Figures 5.6(a) and 5.6(b) show, respectively the data acquisition system *NI 9237* with *DSUB* and *RJ50*, with a detailed identification of the input signals name.

Regardless of the type of port, each of the devices can measure the signals of four full-bridges and so, since there are six sensing bars and six full-bridges, we need two DAQ devices. The connection between the strain gauges and the DAQ device is shown in figure 5.7. For one full bridge, for each *RJ50* input, pins 2, 3, 6 and 7, that correspond to AI+, AI-, EX+ and EX-, are used. In the case of the *DSUB* connector the same input signals have to be considered being possible to connect four full bridges, as there are four equal set of inputs.

These devices can be easily connected to a computer via USB and, in order to obatain the decoded results, they require the use of a specified computer software (*LabVIEW - NI*).

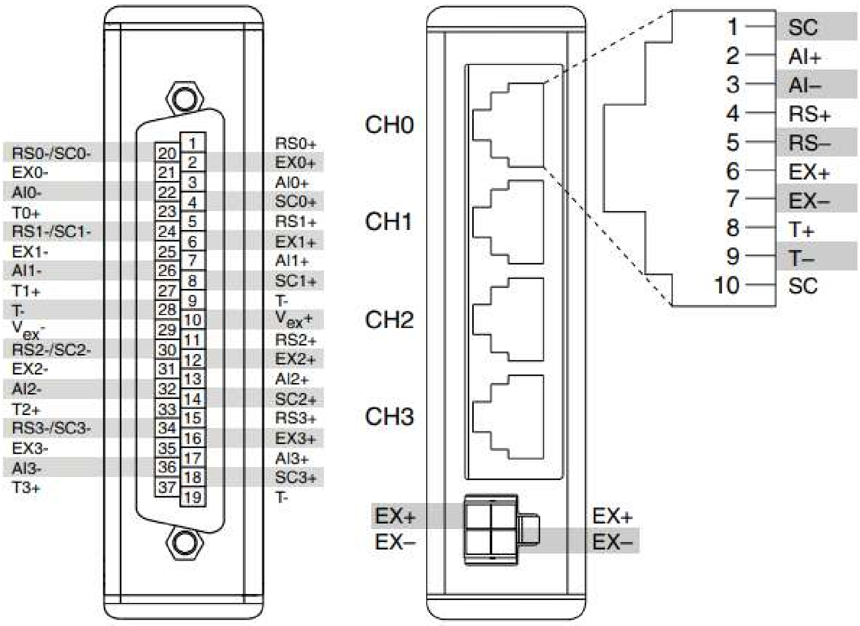

(a) With *DSUB* inputs (b) With *RJ50* inputs

Figure 5.6: *NI 9237*

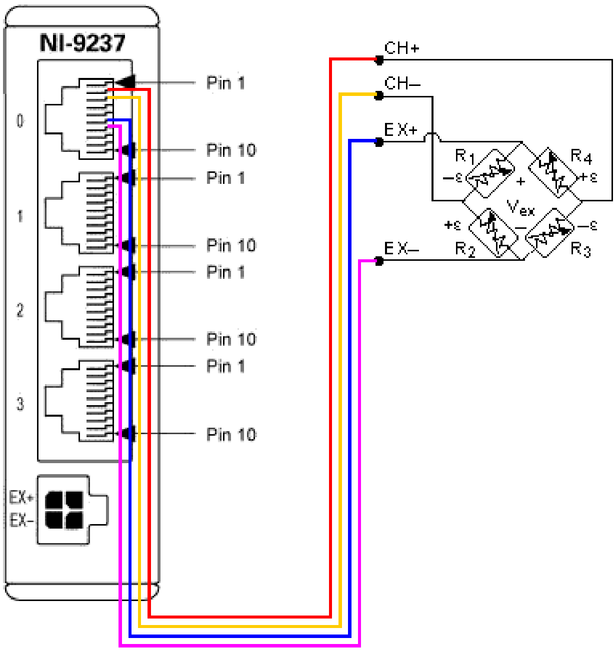

Figure 5.7: Connection of the full bridge to the *DAQ* device (*National Instruments*^{TM})

Chapter 6

Manufacturing, Cost and Assembly

After having defined the set of parts and mechanisms that are to be assembled into the force balance, it is important to clarify, first, the manufacturing process of each made-to-measure component and describe in detail the stock components and second, the way all the pieces have to be put together and connected mechanically. After the structure of the force balance is fully assembled, it has to be instrumented by attaching the extensometers to the sensing bars and connect them to the data acquisition system, as referred previously.

6.1 Bill of Materials

In order to simplify the description and visualization of the force balance components, it is possible to write a bill of materials which is a list of all the force balance components, both mechanical and electronic, and other parts that are going to be needed as well as the respective quantities. This list will include not only the components referred and described in chapter 4 but also the connecting components that are going to be necessary for the assembly, like bolts and nuts. This bill of materials presented in table 6.1 shows all the components of the force balance along with the respective quantities and suppliers.

6.2 Mechanical Components Manufacturing and Selection

After having presented the bill of parts that will compose the force balance, it is necessary to highlight the main aspects related to their manufacturing processes or, in the case of stock parts, explain the selection process that supported some decisions.

Starting with the parts that were made to specification, in a specialized shop, that are the table, the fixed platform, the couplers and the mechanism to control de angle of attack, some considerations have to be made.

Table 6.1: Bill of materials

	Component	Quantity	Manufacturer/Supplier
Mechanical	Table	1	Peçolopes, Lda.[1]
	Rotating collar	1	Casauto, Lda.
	Fixed platform	1	Peçolopes, Lda.[1]
	Coupler	12	Peçolopes, Lda.[1]
	Rod end bearing - left (INA GAL8-UK)	6	Enriel, S.L.
	Rod end bearing - right (INA GAR8-UK)	6	Enriel, S.L.
	Sensing bar	6	Leroy Merlin©
	Moving platform	1	IST
	Flange	1	Aluminium supplier
	Strut	1	Hardware store
	α adjustment mechanism (part 1)	1	Peçolopes, Lda.[1]
	α adjustment mechanism (part 1)	1	Peçolopes, Lda.[1]
	M6 hex bolt and nut	27	Hardware store
	M8 hex bolt and nut	8	Hardware store
	M4 flat-head bolt and nut	6	Hardware store
	M5 flat-head bolt and nut	9	Hardware store
	M10 hex bolt and nut	1	Hardware store
	Dowel pins and brakes	12	Hardware store
Electronic	Strain gauges (HBM 1-LY13-6/350)	24	HBM
	DAQ NI9237	2	National Instruments™

[1] The purchase is being processed by IST.

Table

As referred previously in section 4.2.7, this table is part of the sideslip adjustment mechanism and, at the same time, it is used as the connection platform between the force balance structure and the ground. For this reason, one of the main functions of this component is to provide support. Considering its shape, the best way to obtain this component is to cut a sheet metal to de desired shape and drill the holes that are using to connect other components. Given the thickness of the steel sheet, this component has to be manufactured in a specialized shop.

Fixed platform

Similarly and taking into account the fact that the material and the thickness of the fixed platform and the table are the same, the manufacturing mechanism is the same. In fact, both components can be made of the same steel sheet cut to the desired shape of each component. For this reason, this part is also manufactured using the same technique in the same specialized shop.

Couplers

As for the couplers, they consist in a $3\ mm$-thick steel sheet, cut to the desired planform shape of the component that were bent until reaching the desired shape.

Angle of attack adjustment mechanism

The two components that compose this mechanism are very similar and hence the manufacturing process is the same. As it occurs for the couplers, these two components are produced by cutting an aluminium sheet with a thickness of $5\ mm$ to the respective planform configuration of the components and bending it to the final configuration.

In order to made the purchasing process easier, and given the similarities presented in the conception of the above-mentioned components, a research on companies capable of cutting both aluminium and steel sheets with the desired thickness and performing sheet metal bending was carried out in order to get all the parts from the same supplier. After many quotation requesting and guaranteeing the companies met the purchase requirements defined by IST, the choice fell on *Peçolopes, Lda*.

Regarding the off-the-shelf components (rotating collar and left and right rod end bearings), their selection underwent a process of research and critical comparative analyses between all the available options.

Rotary collar

Considering the rotary collar presented in section 4.2.7 and after a market research, it was possible to find this solution available in *Casauto, Lda.* and, as of this date, the purchasing process is concluded.

Rod end bearings

Regarding the rod end bearings, as discussed in section 4.2.4, their selection process was made simultaneously with the selection process of the sensing bars. After having decided the characteristic dimension of the rod end bearings, that is, the M8 male thread, a market research had to be carried out in order to find the most suitable option, not only in terms of load carrying capabilities, but also in terms of price-quality ratio. Regarding the maximum admissible load values, it was possible to conclude that, considering rod end bearing with external M8 male threads from different manufacturers, the differences were negligible and, moreover, the maximum load values were found to be considerably larger than the maximum expected values at the bars of the force balance. For this reason, the selection process was lead by the price factor and the IST purchasing requirements. The choice fell on INA GAL8-UK left rod end bearing and INA GAR8-UK right rod end bearing, supplied by *Enriel, S.L.*.

Sensing bars

The cross-section dimensions of the sensing bar have already been discussed in section 4.2.3 and the justification for this selection presented. The choice fell on closed-cross section bars with $10\ mm$ of diameter. These bars can be found with a length of $1\ m$ at the most common hardware stores, which means that, based on the dimensions presented previously, one tube can produce three sensing bars thus being necessary to have two tubes, for the six bars. After the initial tubes were cut to the desired length of the sensing bars, it was necessary to drill the M8 left and right threads to tighten the rod end bearings at both extremities being this a relatively easy process.

Moving platform

As discussed in section 4.2.5, as this component is assembled above the strain gauges, it is important to keep it as lightweight as possible and, for this reason, a laminate sandwich panel will be used. This material is used at the Aerospace Engineering's Laboratory in many projects and was kindly provided to be used in this project. In fact, the laminate itself can be manufactured at the laboratory, in order to fit the desired specifications. After a sheet of this laminate is produced, it is relatively easy to cut it to the desired shape and drill the holes to connect other components.

Flange

This component is made of aluminium and the fabrication process is relatively simple. Regarding the shape of the flange, it starts from a cylinder with $100mm$ of external diameter, $30mm$ of internal diameter and a height of $35\ mm$. The raw aluminium block is then machined to the final configuration using *Computer Numerical Control* (CNC). After obtaining the final shape, it is possible to drill holes to connect the flange to the platform and to the strut.

Strut

Using a similar selection methodology as for the sensing bars, the strut is obtained by cutting an aluminium tube with $30\ mm$ of external diameter and $22\ mm$ of internal diameter to the desired length. In this case, however, we have to consider the existence of two testing scenarios that require the use of two struts with different heights, one with $400\ mm$ and another with $130\ mm$. As they present the same external and internal diameters, they can be obtained from the same initial tube. As it occurs for the sensing bars, this tube can be purchased in hardware stores or in aluminium suppliers, provided this is a standard cross-section dimension.

Having defined the metallic components that compose the force balance and presenting their manufacturing or selection process, it is necessary to present some considerations regarding the electronic devices that have to be used in order to make it fully operational.

6.3 Mechanical Assembly

To keep all the components in place and guarantee the force balance integrity, it is necessary to carefully detail the way the components are linked to each other. As it can be seen in table 6.1, the main mechanism used to connect the components is the bolted connection. The table at the bottom of the whole structure is connected to a platform by means of 8 M8 bolted connections that is attached to the ground. Above this table, the rotary collar is also linked to the table using, in this case, 6 M5 bolts with flat head.

The flat head is used in this case due to the lack of space between the table, the fixed platform and the rotary collar. Similarly, to connect the rotary collar to the fixed platform, 6 M4 bolts with flat heads will be used. To link both fixed and moving platform to the couplers, a total of 24 M6 bolted connections are necessary. As for the flange, 3 M6 bolted connectors will be used to attach it to the moving platform and 3 M5 bolts will be used to tightly secure the strut. Considering the mechanism to adjust the angle of attack at the top of the strut, a M10 bolted connection will be used to tighten both components together after selecting the desired angle of attack.

The connection between the rod end bearings and the couplers is made of dowel pins and the respective breaks. The dowel pins can be manufactured to fit the desired dimensions. One is interested in having pins with $8\,mm$ of diameter that can be obtained by cutting steel bars with this same diameter into pins of around $40\,mm$. This dimension corresponds to the distance between the two $8\,mm$ holes of the coupler ($24\,mm$) plus an extra length to both sides, necessary to link the brakes that keep the mechanism in place. In order to guarantee that the rod end bearing does not slip in the pin, two additional brakes will be placed at each side of the rod end bearing.

6.4 Instrumentation

In order to guarantee the higher accuracy on the strain gauges measurements, the attachment of the strain gauges to the sensing bars requires high level of detail. As referred previously in section 2.3.1, the strain gauges will be connected as full bridges. In this case, whenever two of the strain gauges are in tension, the other are in compression. Given this, it is necessary to guarantee the correct alignment of the strain gauges, as they have to be attached in two perfectly perpendicular pairs. In order to guarantee a correct attachment of the strain gauges to the aluminium bars, a set of tips, provided by the manufacturer of the strain gauges (HBM), can be presented:

- **Proper preparation** It is necessary to guarantee that all the materials are previously prepared and organized to guarantee that everything goes as expected;
- **Bonding surface preparation** The regions of the metal where the strain gauges are to be attached have to be treated in order to obtain a smooth surface without pores, notches and oxides. This process is usually carried out by using a sandblaster or, more simply, a handheld sander;
- **Surface cleaning** After the surface is softened, it has to be completely cleaned to eliminate grease and dust. It can be used a proper cleaning agent, preferably, an organic solvent. Clean pads should be used to wipe down the area;
- **Measuring points** In this case, four measuring points have to be marked in each bar, corresponding to the center of each strain gauge. This operation must be done with a ball pen as it avoids the creation of any further notches;
- **Adhesive selection** To attach the strain gauges to the bars, an adequate adhesive has to be selected being the most common a super-glue;

- **Strain gauge handling** The handling of the strain gauges has to be very careful and, since these components are very small, tweezers must be used.

After the strain gauges are carefully attached to the bars, a wiring procedure must be carried out. First, wires have to be welded to the strain gauges leads in order to form the full bridge circuit that was presented in section 2.3.1. After the wiring process is completed, it is possible to connect the full bridges to the data acquisition device, as discussed in section 5.3.

Further consideration on the strain gauge installation process can be found in literature, however, in this case, the most relevant is the one provided by the strain gauge manufacturer (HBM) [37].

6.5 Cost Breakdown

Considering the bill of materials presented before, it is possible to come up with an estimated budget for the force balance. Regarding off-the-shelf components, not only mechanical but also electronic, it was possible to research and find the best offers. Concerning all made-to-specification components, several requests of quotation to specialized companies had to be made, in order to obtain the best offers. Table 6.2 sums up the final cost of each component and the estimated cost of the force balance.

Table 6.2: Expected cost for force balance components

	Component	Quantity	Price (€)	%
Mechanical	Table	1	121.52	3.1
	Rotating collar	1	57.58	1.5
	Fixed platform	1	117.86	3.0
	Coupler	12	210.18	5.3
	Rod end bearing (INA GAL(R)8-UK)	12	231.60	5.8
	Sensing bar	6	8.00	0.2
	Moving platform	1	–	–
	Flange[1]	1	15.00	0.4
	Strut[1]	1	8.00	0.2
	α adjustment mechanism	2	139.09	3.5
	Bolts, nuts and other connectors	106	19.25	0.5
	Subtotal		928.08	23.4
Electronic	Strain gauges (HBM 1-LY13-6/350)	24	253.65	6.4
	DAQ NI9237	2	2782.00	70.2
	Subtotal		3035.65	76.6
	Total		3963.73	100

[1] This indicates that the cost is estimated and is based on similar parts.

It is possible to conclude that, in terms of cost percentage, the electronic components of the force balance constitute the main slice of the whole project as the data acquisition devices needed to decode the output signals of the strain gauges represent more than 70% of the total cost of the force balance. Overall, it is possible to conclude that this is an expensive project and, for this reason, the assembling and calibration procedures have to be carefully carried out so that the force balance measurements can be as precise as possible.

Chapter 7

Calibration

In order to use the force balance, it is necessary to have it fully calibrated. Since one is using strain gauges to assess the loading condition of the balance, it is necessary to convert the voltage output of each of the six bridges attached to the bars to the real loading condition in terms of lift, drag and side forces and rolling, pitching and yawing moments. To perform this calibration, it is necessary to select and apply a numerical methodology as well as an adequate calibration facility. In the following sections, several considerations about the recommended calibration method [38] to be adopted will be described.

7.1 Calibration Methodology

The first step on the calibration methodology is to select the mathematical relation between the strain gauges output and the loading components acting on the model. The output voltages of the six full bridges will be represented by r_i, with $i = 1, ..., 6$. Analogously, the aerodynamic components will be represented by f_i, being f_1 drag, f_2 side and f_3 lift forces and f_4 rolling, f_5 pitching and f_6 yawing moments. The basic relation, for a certain and unspecified loading condition, is described by

$$f_i = f(r_1, r_2, r_3, r_4, r_5, r_6). \tag{7.1}$$

It is necessary to refer that each force component is dependent not only on the force transducers output, but also on the calibration test that is being carried out and this last dependence is not shown in equation (7.1).

In fact, each component of the force or moment can generate disturbances on the sensing bars and thus induce an output in the respective bridge. The purpose of the calibration is to know, quantitatively, this relation between the output voltages of the bridge and the loading components.

There are several mathematical formulations that can be used to relate both quantities but the most common is to use a third-order polynomial with respect to the transducers output. An example, for an arbitrary component of one specific loading condition/calibration test, is

$$\begin{aligned} f_i = {} & r_1 c_{i,1} + r_i c_{i,2} + r_3 c_{i,3} + r_4 c_{i,4} + r_5 c_{i,5} + r_6 c_{i,6} + r_1^2 c_{i,7} + r_1 r_2 c_{i,8} + r_1 r_3 c_{i,9} \\ & + r_1 r_4 c_{i,10} + r_1 r_5 c_{i,11} + r_1 r_6 c_{i,12} + r_2^2 c_{i,13} + r_2 r_3 c_{i,14} + r_2 r_4 c_{i,15} + r_2 r_5 c_{i,16} + r_2 r_6 c_{i,17} + r_3^2 c_{i,18} + \\ & + r_3 r_4 c_{i,19} + r_3 r_5 c_{i,20} + r_3 r_6 c_{i,21} + r_4^2 c_{i,22} + r_4 r_5 c_{i,23} + r_4 r_6 c_{i,24} + r_5^2 c_{i,25} + r_5 r_6 c_{i,26} + r_6^2 c_{i,27}. \end{aligned} \tag{7.2}$$

As one can see, although the non-linear relation regarding the functions of r, the dependence on the coefficients $(c_1, c_2, ...)$ is purely linear. This coefficients will, then, be part of the so-called calibration matrix. It is important to remind that for each loading condition, there are six aerodynamic components and thus, six equations similar to the one described in equation (7.2). To obtain the coefficients $c_{i,j}$ of the calibration matrix, it is necessary to apply a set of known loading conditions, read the output voltages of the force transducers and then relate both. Since, for each component, the number of calibration coefficients is relatively large, it is necessary to apply a large number of calibration loads to obtain all the 27×6 coefficients, that is, 162 components of the calibration matrix. The high number of elements of the matrix coefficients requires a large number of calibrations with different loading conditions.

In vectorial terms, it is possible to write

$$\mathbf{f} = \mathbf{CR} + \epsilon, \tag{7.3}$$

where the matrix ϵ that can be regarded as a measurement error, where $\mathbf{f}$ is the loading vector of each aerodynamic component with dimension $N \times 1$, $\mathbf{R}$ represents the strain gauges readings matrix and has a dimension of $N \times 27$ and $\mathbf{C}$ is the calibration vector of each loading condition and has a dimension of 27×1, being N the number of loading conditions.

7.2 Least Squares Formulation

Least squares formulation has become one of the major tools for parameters estimation on experimental data. Although there are other methods available, this one provides good results and is the most widely known as it is easier to comprehend and provide better results. In fact, this method was found to have optimal statistical properties as it is consistent, unbiased and efficient [39].

Regarding equation (7.3), one can express de error vector as

$$\epsilon = \mathbf{f} - \mathbf{CR}, \tag{7.4}$$

remembering that the purpose of this formulation is to obtain $\mathbf{C}$, as a calibration matrix.

By choosing a certain $\widehat{\mathbf{C}}$, considered to be an approximation of the real $\mathbf{C}$, a minimization of the parameter J, defined as

$$\mathbf{J} = \epsilon^T \epsilon, \tag{7.5}$$

is carried out, where the superscript T indicates the matrix transposition.

By substituting equation (7.4) in equation (7.5), one obtains

$$\begin{aligned}\mathbf{J} &= (\mathbf{f} - \mathbf{RC})^T(\mathbf{f} - \mathbf{RC}) \\ &= \mathbf{f}^T\mathbf{f} - \mathbf{C}^T\mathbf{R}^T\mathbf{f} - \mathbf{f}^T\mathbf{RC} + \mathbf{C}^T\mathbf{R}^T\mathbf{RC}.\end{aligned} \tag{7.6}$$

Now that the parameter $\mathbf{J}$ is fully defined, a differentiation of this parameter in order to $\mathbf{C}$ has to be carried out. The result has to be equated to zero in order to find out the relation by which the estimate $\widehat{\mathbf{C}}$ minimizes $\mathbf{J}$,

$$\begin{aligned}\left.\frac{\partial \mathbf{J}}{\partial \mathbf{C}}\right|_{\mathbf{C}=\widehat{\mathbf{C}}} &= -2\mathbf{R}^T\mathbf{f} + 2\mathbf{R}^T\mathbf{R}\widehat{\mathbf{C}} = 0 \\ \mathbf{R}^T\mathbf{R}\widehat{\mathbf{C}} &= \mathbf{R}^T\mathbf{f}.\end{aligned} \tag{7.7}$$

The result of this differentiation is

$$\widehat{\mathbf{C}} = (\mathbf{R}^T\mathbf{R})^{-1}\mathbf{R}^T\mathbf{f} \tag{7.8}$$

and the parameter $\widehat{\mathbf{C}}$ is called *least-squares estimator* (LSE) of $\mathbf{C}$.

$\widehat{\mathbf{C}}$ was estimated by assuming that the error ϵ is constant during all the performed tests, that is, $\epsilon_1 = \epsilon_2 = ... = \epsilon_k$. This assumption , however, is far from reality since it is not possible to guarantee that the same physical conditions are constant and affect equally the set of tests as the calibration process is mainly manual.

To obtain the new *weighted least-squares estimator*, an analogous process has to be carried out. The new weighted error criterion is

$$\begin{aligned}\mathbf{J}_W &= \epsilon^T\mathbf{W}\epsilon \\ &= (\mathbf{f} - \mathbf{RC})^T\mathbf{W}(\mathbf{f} - \mathbf{RC})\end{aligned}, \tag{7.9}$$

where $\mathbf{W}$ stands for the desired weighting matrix.

By restricting $\mathbf{W}$ to being a symmetric positive definite matrix and carrying out the minimization of the parameter $\mathbf{J}_W$ with respect to $\mathbf{C}$ using the same methodology as in equation (7.7), the *weighted least-squares estimator*,$\widehat{\mathbf{C}}_W$, is obtained, as

$$\widehat{\mathbf{C}}_W = (\mathbf{R}^T\mathbf{W}\mathbf{R})^{-1}\mathbf{R}^T\mathbf{W}\mathbf{f}. \tag{7.10}$$

7.2.1 Weighting Matrix Definition

As said previously, several factors may affect the calibration environment and thus, it is not reasonable to assume that in each observation the transducers and the loading errors are the same. This reason leads to considerate a new factor in the equation, the weighting matrix, $\mathbf{W}$.

Since the calibration is a manual process of applying a pre-defined load to the balance by means of dead weights, pulleys and strings, there are uncertainties that would not be taken into account using the ordinary LS method. Each dead weight has a characteristic fabrication mass whose measurement is made by a balance that induces an uncertainty, so the combination of several dead weights induces an error that is very hard to quantify. As for the pulleys and strings, there are friction forces between both this components that can interfere with the results and whose behaviour is impossible to predict. These are the main sources of error in terms of the calibration process itself.

Regarding the full bridges used to measure the sensing bars deformation, they can also be a source of error as the extensometers are very sensitive to the experimental conditions that can interfere with the output voltages and thus the calibration results.

For this reason, the weighting matrix has to be defined considering the two main sources of error described previously: the one related to the calibration process itself and the other related to the full bridges measurements.

Regarding equation (7.10), the term $(\mathbf{R}^T\mathbf{W}\mathbf{R})^{-1}$ provides information about uncertainties of the estimated parameters, being its diagonal elements called variances (squared uncertainties - $u^2_{\widehat{\mathbf{C}}}$) and its off-diagonal elements are the covariances of the fitted parameters.

As for $\mathbf{W}$, it can be regarded as the inverse of the covariance matrix $(\mathbf{V})$ which is related to the uncertainties of the applied loads $(u_{\mathbf{f}})$. It reflects both sources of error stated above, as represented in equation 7.11 where the first term is related with the weighting process and the other is related to the bridges readings.

$$\mathbf{W} = (\mathbf{V}_W + \mathbf{S}\mathbf{V}_R\mathbf{S}^T)^{-1} \tag{7.11}$$

Regarding the matrices that are used to obtain $\mathbf{W}$, it is necessary to fully explain them.

Matrix $\mathbf{V}_W$

$\mathbf{V}_W$ is a square matrix whose dimension is the number of loading conditions $(N \times N)$ and is considered to be diagonal. As stated previously, this matrix is related to the uncertainties of the calibration process itself that have two main sources: the first one is due to the uncertainties of the applied weights and the other encompasses the remaining sources of error that can affect the behaviour of the calibration system like friction forces between the strings and the pulleys or misalignments.

Matrix $\mathbf{V}_R$

$\mathbf{V}_R$ is a square matrix with dimension $6N \times 6N$ that is related with the uncertainties on the full bridges readings. To obtain this matrix it is necessary to repeat the calibration process with the same loading conditions in the shortest possible time in order to avoid interferences. The diagonal elements of the matrix represent the variance between the same bridges outputs and the off-diagonal elements correspond to the covariant elements.

$$\mathbf{V_R} = \begin{bmatrix} u_{R_{1,1};R_{1,1}} & u_{R_{1,1};R_{1,2}} & \cdots & u_{R_{1,1};R_{1,N}} & u_{R_{1,1};R_{2,1}} & \cdots & u_{R_{1,1};R_{6,N}} \\ u_{R_{1,2};R_{1,1}} & u_{R_{1,2};R_{1,2}} & \cdots & u_{R_{1,2};R_{1,N}} & u_{R_{1,2};R_{2,1}} & \cdots & u_{R_{1,2};R_{6,N}} \\ \vdots & \vdots & \ddots & \vdots & \vdots & \ddots & \vdots \\ u_{R_{1,N};R_{1,1}} & u_{R_{1,N};R_{1,2}} & \cdots & u_{R_{1,N};R_{1,N}} & u_{R_{1,N};R_{2,1}} & \cdots & u_{R_{1,N};R_{6,N}} \\ u_{R_{2,1};R_{1,1}} & u_{R_{2,1};R_{1,2}} & \cdots & u_{R_{2,1};R_{1,N}} & u_{R_{2,1};R_{2,1}} & \cdots & u_{R_{2,1};R_{6,N}} \\ \vdots & \vdots & \ddots & \vdots & \vdots & \ddots & \vdots \\ u_{R_{6,N};R_{1,1}} & u_{R_{6,N};R_{1,2}} & \cdots & u_{R_{6,N};R_{1,N}} & u_{R_{6,N};R_{2,1}} & \cdots & u_{R_{6,N};R_{6,N}} \end{bmatrix} \tag{7.12}$$

In order to obtain the covariance matrix ($\mathbf{V}_R$), it is necessary to obtain a matrix **R** with dimension $6N \times 3$. In this case we are assuming that three similar calibration processes are carried on. Regarding this matrix, the first N elements of column 1 are the readings of the full bridge number 1 from the first calibration process, the next N elements of column 1 are the reading of the full bridge number 2 from the first calibration process and so on. Similarly for the columns 2 and 3, using the results of the second and third calibration processes, respectively. The matrix V_R is then obtained via MATLAB® code.

Matrix $\mathbf{S}$

Matrix $\mathbf{S}$ is the sensitivity matrix and has a dimension of $N \times 6N$ and its components correspond to the partial derivatives of equation (7.2). Considering the component of drag force (f_1), the matrix $\mathbf{S}$ is represented as

$$\mathbf{S} = \begin{bmatrix} \frac{\partial f_{1,1}}{\partial R_{1,1}} & \frac{\partial f_{1,1}}{\partial R_{1,2}} & \cdots & \frac{\partial f_{1,1}}{\partial R_{1,N}} & \frac{\partial f_{1,1}}{\partial R_{2,1}} & \cdots & \frac{\partial f_{1,1}}{\partial R_{6,N}} \\ \frac{\partial f_{1,2}}{\partial R_{1,1}} & \frac{\partial f_{1,2}}{\partial R_{1,2}} & \cdots & \frac{\partial f_{1,2}}{\partial R_{1,N}} & \frac{\partial f_{1,2}}{\partial R_{2,1}} & \cdots & \frac{\partial f_{1,2}}{\partial R_{6,N}} \\ \vdots & \vdots & \ddots & \vdots & \vdots & \ddots & \vdots \\ \frac{\partial f_{1,N-1}}{\partial R_{1,1}} & \frac{\partial f_{1,N-1}}{\partial R_{1,2}} & \cdots & \frac{\partial f_{1,N-1}}{\partial R_{1,N}} & \frac{\partial f_{1,N-1}}{\partial R_{2,1}} & \cdots & \frac{\partial f_{1,N-1}}{\partial R_{6,N}} \\ \frac{\partial f_{1,N}}{\partial R_{1,1}} & \frac{\partial f_{1,N}}{\partial R_{1,2}} & \cdots & \frac{\partial f_{1,N}}{\partial R_{1,N}} & \frac{\partial f_{1,N}}{\partial R_{2,1}} & \cdots & \frac{\partial f_{1,N}}{\partial R_{6,N}} \end{bmatrix}. \tag{7.13}$$

Regarding the aerodynamic loads ($\mathbf{f}$), the first subscript indicates the component ($i = 1, ..., 6$) and the second subscript stands for the calibration loading condition ($j = 1, ..., N$). As for the bridges readings (R), the first subscript indicates the bridge number ($i = 1, ...6$) while the second component stands also for the loading condition ($j = 1, ..., N$). Matrix $\mathbf{S}$ can be simplified as only the partial derivatives that correspond to the same calibration loading condition are different from 0 and so it can be written as

$$\mathbf{S} = \begin{bmatrix} \frac{\partial f_{1,1}}{\partial R_{1,1}} & 0 & \cdots & 0 & \frac{\partial f_{1,1}}{\partial R_{2,1}} & \cdots & 0 \\ 0 & \frac{\partial f_{1,2}}{\partial R_{1,2}} & \cdots & 0 & 0 & \cdots & 0 \\ \vdots & \vdots & \ddots & \vdots & \vdots & \ddots & \vdots \\ 0 & 0 & \cdots & 0 & 0 & \cdots & 0 \\ 0 & 0 & \cdots & \frac{\partial f_{1,N}}{\partial R_{1,N}} & 0 & \cdots & \frac{\partial f_{1,N}}{\partial R_{6,N}} \end{bmatrix}. \tag{7.14}$$

After having presented matrices $\mathbf{V}_R$ and $\mathbf{S}$, it is possible to conclude that the term $\mathbf{S V_R S^T}$ is related to the uncertainties of the full bridges readings that affect the measurements and has a dimension of

$N \times N$. The first estimation of the matrix $\mathbf{S}$ is found in a preliminary analysis where the weighting matrix is considered to be the identity matrix ($\mathbf{I}$), then it is possible to estimate $\mathbf{V}_W$ and assuming $\mathbf{W} = \mathbf{V}_W^{-1}$, it is possible to obtain the matrix $\widehat{\mathbf{C}}_W$ from which the components of $\mathbf{S}$ can be estimated.

Now that all the components of the weighting matrix are defined, it is possible to obtain the least-squares estimator parameter ($\widehat{\mathbf{C}}$) and thus the values of forces and moments estimated by the least-squares formulation, whose vector is represented as $\widehat{\mathbf{f}}$, calculated as

$$\widehat{\mathbf{f}} = \mathbf{R}\widehat{\mathbf{C}}. \tag{7.15}$$

7.3 Fitting Evaluation

In order to assess the efficiency of the method, a new variable has to be introduced, the chi-squared, χ^2. It is defined as

$$\chi^2 = (\mathbf{f} - \widehat{\mathbf{f}})^T \mathbf{W} (\mathbf{f} - \widehat{\mathbf{f}}), \tag{7.16}$$

where $\mathbf{f}$ stands for the applied forces and moments.

Regarding this parameter, χ^2, a good fitting occurs, generally, when this value is close to the number of degrees of freedom that is defined as

$$N - N_p, \tag{7.17}$$

where N indicates the number of loading tests and N_p stands for the the number of components of equation (7.2).

Given this, a new variable arises, the so-called reduced chi-square parameter that is defined as

$$\chi^2_{red} = \frac{\chi^2}{N - N_p}, \tag{7.18}$$

and a value close to 1 represents good quality of fitting.

7.4 Calibration Procedure

Now that the analytical methodology considered to the calibration process was presented, it is important to understand the way some of the quantities will be obtained to construct the matrices.

The first step of this procedure is to build a calibration rig. This consists of a structure that is constituted by strings, dead weights and pulleys and is used to apply the set of loading conditions. Regarding this aspect, it is important to guarantee the alignment between these elements and the reference axis of the force balance. Mechanically, this calibration rig may consist of a metallic structure supported at the level of the attachment point of the model. Several trays support the dead weights hanging by strings in pulleys. The distribution of the trays along the structure must be done before hand, in order to diminish calibration errors and the only factor that is varying between each calibration step is the distribution of the dead-weights in each tray. It is very important to know, in advance, the loading distribution in terms of F_X, F_Y, F_Z, M_X, M_Y and M_Z caused by the application of the weights in each tray.

The next step on the calibration procedure consists of selecting the dead-weights to be used. In fact, the set of loading conditions will be defined by varying the not only the components that are being considered in each calibration step but also by varying the values of the dead-weights which reflects in changing the values of forces and moments to be measured. In order to guarantee that the force balance is capable of measuring an adequate range of loads, the selected dead-weights must present a wide spectrum, in order to test different orders of magnitude within the range of expected loads and moments found in section 3.2.3.

Once the calibration rig is set up and the dead-weights defined, it is necessary to establish the set of calibration scenarios. This corresponds to the parameter N presented before in section 7.1. The number of loading scenarios has to be greater than the number of coefficients of the equation (7.2) and has to account not only for the range of dead-weights, but also for the different possible combinations of forces and moments.

After planning the N testing conditions, the process is relatively simple. For each loading scenario, the output of each full bridge has to be registered, in order to obtain the matrix $\mathbf{R}$. It is necessary to highlight that 3 similar calibration procedures have to be carried out in order to obtain the covariance matrix ($\mathbf{V}_R$). After that, the methodology presented above is used and the fitting evaluated.

The overall method can be summed up in the following procedures:

- Select the dead weights;
- Plan, carefully, each loading condition of the calibration process;
- Apply the desired weights to each tray;
- For each loading condition, register the output of each of the six full bridges ($\mathbf{R}$);
- After all the results for the N loading conditions are obtained, repeat the procedure two more times;
- Estimate the weighting matrix $\mathbf{W}$, firstly, as the identity matrix and obtain $\mathbf{C}$;
- Compute the load values as $\widehat{\mathbf{f}} = \mathbf{R}\widehat{\mathbf{C}}$;
- Obtain an estimation of the matrix $\mathbf{V}_W$ by calculating the deviation between the real loading values and estimated values;
- Consider a new iteration with $\mathbf{W} = \mathbf{V}_W^{-1}$;
- Obtain the new matrix $\mathbf{C}$ and compute $\mathbf{S}$;
- Consider a new iteration with $\mathbf{W} = (\mathbf{V}_W + \mathbf{S}\mathbf{V}_R\mathbf{S}^T)^{-1}$ and estimate $\widehat{\mathbf{f}}$;
- Evaluate the fitting.

Chapter 8

Conclusions

8.1 Achievements

The main goal of this master thesis was to design a force balance to use in the Aerospace Engineering Laboratory's wind tunnel at Instituto Superior Técnico. In order to adapt it to the dimensions of the wind tunnel and to the possible measuring scenarios, a careful analysis was carried out.

After having defined the load range the force balance has to be able to carry, it was possible to define its main structure. A comparative analysis based on relevant criteria, such as cost, manufacturing simplicity or measurement accuracy, was performed in order to find the most suitable layout for this application. This analysis along with further research revealed that a *Stewart* platform-based force balance was the best option.

Combining the two main structural aspects stated above (load range of operation and force balance layout), it was possible to mechanically design all the components of the force balance. This mechanical analysis had to take into account several aspects, like the weight of the structure, the manufacturing easiness of the components, the maintenance simplicity of the parts and the assembly of the whole structure, but always keeping the overall budget as low as possible.

Having established the mechanical structure of the force balance and guaranteed its integrity when the maximum expected loads are applied, it was necessary to fully instrument it so that the applied forces and moments can be quantified, by measuring the deformation of the structure. To do so, specific strain gauges and data acquisition system were selected and an installation scheme was presented.

In order to guarantee the accurate correspondence between the applied loads and the sensors measurements, a calibration process has to be carried out so a methodology based on the least squares theory was proposed.

In conclusion, a fully operational force balance concept was designed to be placed in the wind tunnel to test a wide range of models, provided all the components are available.

8.2 Future Work

Having established the design of the force balance, it will be necessary to manufacture all made to specification components and acquire the remaining in order to fully assemble it.

In order to guarantee the maximum versatility of the force balance, instead of considering two different struts for the two distinct testing scenarios, it is possible to design a strut with adjustable length allowing one to test models with different shapes and dimensions.

To prevent undesired unbalances and instabilities, the force balance has to be carefully attached to the ground and so, for this reason, it may be required to develop a dedicated mechanism capable of avoiding such interferences.

As described in section 2.3.3, different types of attitude sensors could be connected to the structure in order to fully monitor the angular position of the model that is being tested. To limit the human interference in the force balance operation, additional devices could be implemented to control the position of the model in test. For instance, to rotate the collar underneath the fixed platform and adjust the angle in the vertical Z-axis, a small motor could be used. Similarly, a mechanism could be implemented to adjust the angle in the horizontal Y-axis at the top of the strut, however, in this case, additional aspects have to be considered since the device would be placed in the test section and so, it would cause interferences in the measured loads that have to be mitigated during the calibration process.

On the other hand, in order to create a light weight structure, several components could be designed considering different materials, namely, all the components that stand above the strain sensors. For instance, the metallic strut made of an aluminium alloy could be replaced by a lighter composite tube, as long as the conditions of maximum loading range and displacements continued to be fulfilled. In this connection, to narrow down the load acting on the strut itself, a cover mechanism for the strut with a more aerodynamic shape could be developed. This would allow the forces and moments acting on the model to be transferred directly to the sensing bars, without any further interferences on the strut member.

The output signals of the full bridges are converted to values of strain by using a data acquisition system, however, these values have to be posteriorly converted to the respective components of forces and moments, as a result of the calibration process that has to be carried out. It would be appealing to have a software, associated with the data acquisition system, capable of displaying the values of forces and moments directly and in real-time.

Bibliography

[1] J. Barlow, W. Rae, and A. Pope. *Low-Speed Wind Tunnel Testing*. John Wiley & Sons, 3^{rd} edition, 1999. ISBN 0471557749.

[2] M. Belan and F. Messanelli. Wind tunnel testing of multi-tip corona actuators on a symmetric airfoil. *Journal of Electrostatics*, 85:23–34, 2017. ISSN 0304-3886. doi:10.1016/j.elstat.2016.12.002.

[3] P. Lv, F. Mohd-Zawawi, S. Prothin, J. Moschetta, and J. Morlier. Adaptive proprotors as applied to convertible MAVs optimum twist of MAVion proprotor. *International Micro Air Vehicle Conference and Flight Competition (IMAV2013)*, pages 17–20, 2013.

[4] R. M. Cummings and A. Schütte. The NATO STO task group AVT-201 on 'Extended Assessment of Stability and Control Prediction Methods for NATO Air Vehicles'. *32^{nd} AIAA Applied Aerodynamics Conference*, pages 1–32, 2014. doi: 10.2514/6.2014-2000.

[5] P. Fiala, T. Jirků, Z. Szabó, and M. Steinbauer. Formula SAE aerodynamic optimization. Master's thesis, Faculty of Mechanical Engineering, Brno University of Technology, 2016.

[6] J. Mattuella, A. Loredo-Souza, M. Oliveira, and A. Petry. Wind tunnel experimental analysis of a complex terrain micrositing. *Renewable and Sustainable Energy Reviews*, 54:110–119, 2016. ISSN 1364-0321. doi:10.1016/j.rser.2015.09.088.

[7] Y. Tominaga and B. Blocken. Wind tunnel experiments on cross-ventilation flow of a generic building with contaminant dispersion in unsheltered and sheltered conditions. *Building and Environment*, 92: 452–461, 2015. ISSN 0360-1323. doi:10.1016/j.buildenv.2015.05.026.

[8] B. F. R. Ewald. Multi-component force balances for conventional and cryogenic wind tunnels. *Measurement Science and Technology*, 11(6):R81, 2000. URL `http://stacks.iop.org/0957-0233/11/i=6/a=201`.

[9] C. Tropea, A. L. Yarin, and J. F. Foss. *Springer handbook of experimental fluid mechanics*, volume 1. Springer Science & Business Media, 2007.

[10] A. Smith, D. Mee, W. Daniel, and T. Shimoda. Design, modelling and analysis of a six component force balance for hypervelocity wind tunnel testing. *Computers & Structures*, 79(11):1077–1088, 2001. doi:10.1016/S0045-7949(01)00005-0.

[11] R. K. Jr. Air velocity and flow measurement using a pitot tube. *ISA Transactions*, 37(4):257 – 263, 1998. ISSN 0019-0578. doi: 10.1016/S0019-0578(98)00036-6. URL `http://www.sciencedirect.com/science/article/pii/S0019057898000366`.

[12] R. C. P. E. Ower. *The Measurement of Air Flow.* Pergamon, 5^{th} edition, 1977. ISBN: 9781483188041.

[13] D. G. Hull. *Fundamentals of Airplane Flight Mechanics*. Springer Publishing Company, Incorporated, 1^{st} edition, 2007. ISBN 3540465715, 9783540465713.

[14] M. Kok, J. D. Hol, and T. B. Schön. Using inertial sensors for position and orientation estimation. *CoRR*, abs/1704.06053, 2017. URL `http://arxiv.org/abs/1704.06053`.

[15] XFLR5, v6.40. [Online] Available at: `http://www.xflr5.com/xflr5.htm` [Accessed: Feb-2018].

[16] J. Anderson. *Fundamentals of Aerodynamics*. McGraw-Hill Education, 2010. ISBN 9780073398105.

[17] T. Preusser and L. Polansky. External 6-component wind tunnel balances for aerospace simulation facilities. In *International Congress on Instrumentation in Aerospace Simulation Facilities, ICIASF'89 Record.* IEEE, 1989.

[18] S. Marin, S. Adriana, and I. Georgeta. Design of a compact six-component force and moment sensor for aerodynamic testing. *Incas Bulletin*, 3(1):95–100, 2011. doi: 10.13111/2066-8201.2011.3.1.13.

[19] A. R. Tavakolpour-Saleh, A. R. Setoodeh, and M. Gholamzadeh. A novel multi-component strain-gauge external balance for wind tunnel tests: Simulation and experiment. *Sensors and Actuators, A: Physical*, 247:172–186, 2016. ISSN 09244247. doi: 10.1016/j.sna.2016.05.035.

[20] D. Martinez, C. Meaurio, D. Alviso, J. Chaparro, E. Vargas, and J. C. Rolon. Design and implementation of an aerodynamic balance in a subsonic wind tunnel and validation through numerical and experimental investigations of lift and drag performances on airfoils. *16^{th} Brazilian Congress of Thermal Sciences and Engineering*, 2016.

[21] G. Raush, R. Castilla, P. Gamez-Montero, J. Wojciechowski, and E. Codina. Flexible rod design for educational wind balance. *Experimental Techniques*, 40(1):111–119, 2016. ISSN 17471567. doi: 10.1007/s40799-016-0017-9.

[22] M. Samardžić, Z. Anastasijević, D. Marinkovski, D. Ćurčić, and J. Isaković. External six-component strain gauge balance for low speed wind tunnels. *Scientific Technical Review*, 64(3):40–46, 2014.

[23] A. LLC. Pyramidal force/moment balance. [Online] Available at: `https://www.aerolab.com/products/pyramidal-balance/` [Accessed: May-2017].

[24] T. Saaty. *The Analytic Hierarchy Process*. McGraw-Hill, 1980.

[25] B. Dasgupta and T. S. Mruthyunjaya. The Stewart platform manipulator: a review. *Mechanism and Machine Theory*, 35(1):94–114, 2000. doi: http://dx.doi.org/10.1016/S0094-114X(99)00006-3.

[26] D. Stewart. A platform with six degrees of freedom. *Proceedings of the Institution of Mechanical Engineers*, 180(1):371–386, 1965.

[27] R. Ben-Horin, M. Shoham, and S. Djerassi. Kinematics, dynamics and construction of a planarly actuated parallel robot. *Robotics and Computer-Integrated Manufacturing*, 14(2):163–172, 1998. doi: http://dx.doi.org/10.1016/S0736-5845(97)00035-5.

[28] J. M. Selig. *Geometrical Methods in Robotics*. Springer-Verlag, Berlin, Heidelberg, 1^{st} edition, 1996. ISBN 0387947280.

[29] J. Lee. *Investigation of quality indices of in-parallel platform manipulators and development of Web-based analysis tool*. PhD thesis, University of Florida, 2000.

[30] L. Performance Composites. Mechanical properties of carbon fibre composite materials. [Online] Available at: `http://www.performance-composites.com/carbonfibre/mechanicalproperties_2.asp` [Accessed: Jan-2018].

[31] E. R. E. GmbH. Product information: Rohacell © ig/ig-f. [Online] Available at: `http://www.rohacell.com/product/rohacell/en/products-services/rohacell-ig-ig-f/` [Accessed: Jan-2018].

[32] HBM. Ly: Linear strain gages with 1 measurement grid, . [Online] Available at: `https://www.hbm.com/en/4561/ly-linear-strain-gauges-with-1-measurement-grid/` [Accessed: Sep-2017].

[33] HBM. Strain gauges: Absolute precision from hbm, . [Online] Available at: `https://www.hbm.com/fileadmin/mediapool/hbmdoc/technical/s1265.pdf` [Accessed: Apr-2018].

[34] M. Kreuzer. High-precision measuring technique for strain gage transducers. Technical report, Hottinger Baldwin Messtechnik, 2001.

[35] M. Borges. Design of an apparatus for wind tunnel tests of electric uav propulsion systems. Master's thesis, Instituto Superior Técnico, June 2015.

[36] *National Instruments*™. Ni 9237: datasheet. [Online] Available at: `http://www.ni.com/pdf/manuals/374186a_02.pdf` [Accessed: Apr-2018].

[37] K. Hoffmann. *Practical Hints for the Installation of Strain Gauges*. Hottinger Baldwin Messtechnik GmbH, Darmstadt, Germany, June 2014.

[38] M. Reis, R. Castro, and O. Mello. Calibration uncertainty estimation of a strain-gage external balance. *Measurement*, 46(1):24–33, 2013. doi: https://doi.org/10.1016/j.measurement.2012.09.016.

[39] T. C. Hsia. *System identification: least-squares methods*. Lexington (Mass.) : Lexington books, 1977. ISBN 0669996300.

Appendix A

XFLR5 Simulation Results

This chapter presents all the simulations that had to be performed with *XFLR5, v6.40* to assess the testing scenarios described in section 3.2. In this case, the airfoils were discretized in 100 points.

A.1 Stall Angles

Half-Wing Model

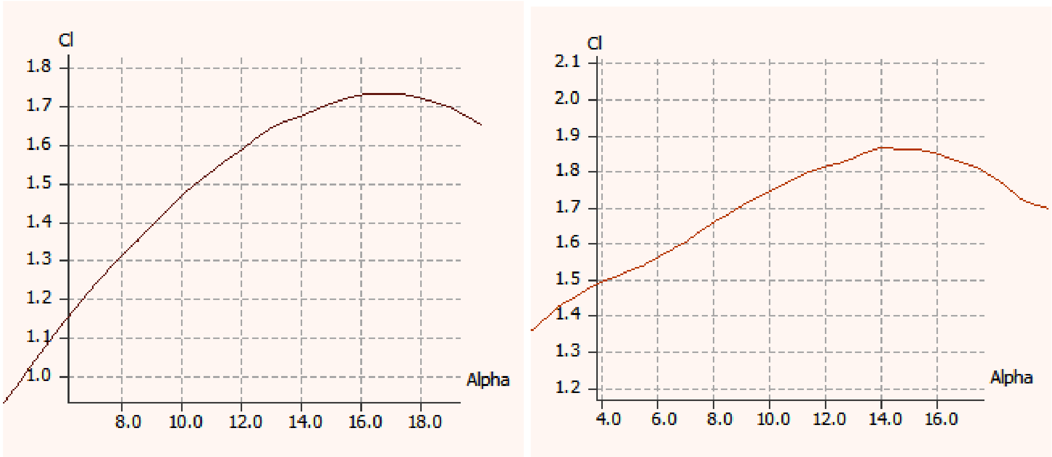

(a) NACA 4412 unflapped (AR 4) ($\alpha_{stall} = 16°$)

(b) NACA 4412 with 10° flap (AR 4) ($\alpha_{stall} = 14°$)

Figure A.1: Wing *XFLR5* simulation results for stall angles

Full Aircraft Model

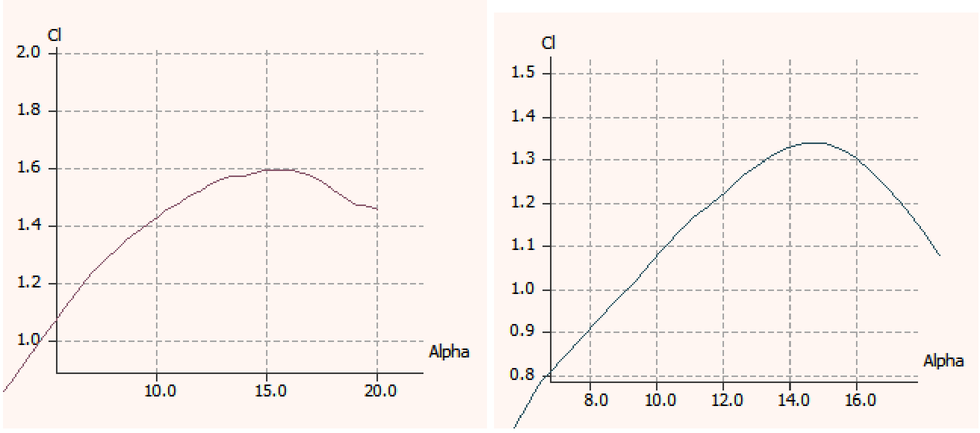

(a) NACA 4412 unflapped (wing) ($\alpha_{stall} = 15°$)
(b) NACA 0012 unflapped (tail) ($\alpha_{stall} = 14°$)

Figure A.2: Aircraft *XFLR5* simulation results for stall angles

A.2 Half-Wing Model Coefficients

Without flaps

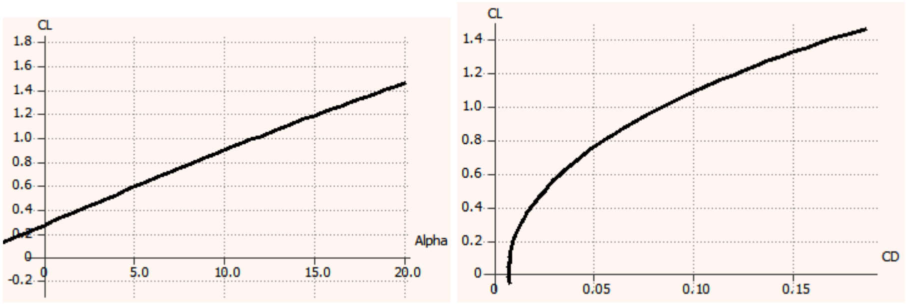

(a) C_L versus α
(b) C_L versus C_D

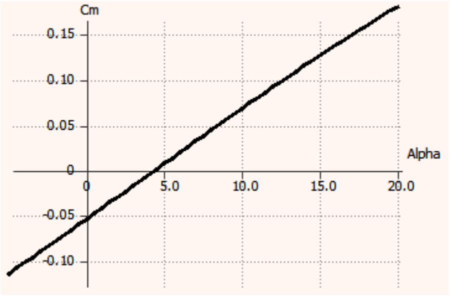

(c) C_M versus α

Figure A.3: *XFLR5* simulation results for a wing with an aspect ratio of 4 (without flaps)

$10°$ **trailing edge flap**

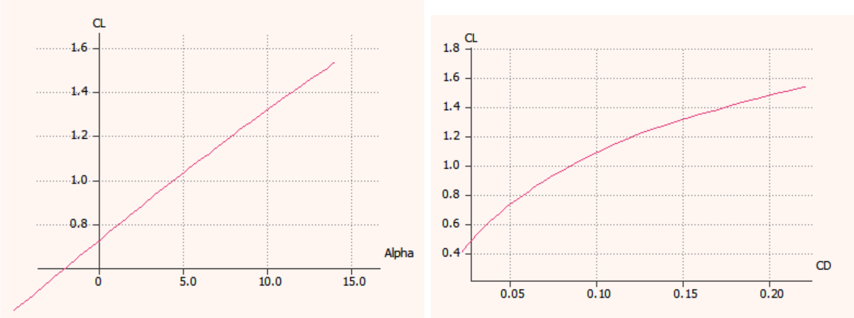

(a) C_L versus α (b) C_L versus C_D

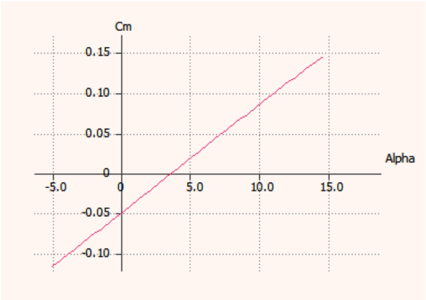

(c) C_M versus α

Figure A.4: *XFLR5* simulation results for a wing with an aspect ratio of 4 ($10°$ trailing edge flap)

Appendix B

AHP Matrices

$$\begin{bmatrix} 1 & 1/2 & 1/7 & 1/4 & 1/3 & 1/4 \\ 2 & 1 & 1/4 & 1/3 & 1 & 1/4 \\ 7 & 4 & 1 & 3 & 4 & 2 \\ 4 & 3 & 1/3 & 1 & 2 & 1 \\ 3 & 1 & 1/4 & 1/2 & 1 & 1/3 \\ 4 & 4 & 1/2 & 1 & 3 & 1 \end{bmatrix}$$

(a) Robustness

$$\begin{bmatrix} 1 & 4 & 8 & 7 & 3 & 2 \\ 1/4 & 1 & 5 & 4 & 1/2 & 1/3 \\ 1/8 & 1/5 & 1 & 1/3 & 1/5 & 1/7 \\ 1/7 & 1/4 & 3 & 1 & 1/3 & 1/5 \\ 1/3 & 2 & 5 & 3 & 1 & 1/3 \\ 1/2 & 3 & 7 & 5 & 3 & 1 \end{bmatrix}$$

(b) Simplicity

$$\begin{bmatrix} 1 & 4 & 6 & 5 & 7 & 4 \\ 1/4 & 1 & 5 & 4 & 6 & 3 \\ 1/6 & 1/5 & 1 & 1/3 & 2 & 1/4 \\ 1/5 & 1/4 & 3 & 1 & 3 & 1/3 \\ 1/4 & 1/6 & 1/2 & 1/3 & 1 & 1/5 \\ 1/3 & 1/3 & 4 & 3 & 5 & 1 \end{bmatrix}$$

(c) Fabrication

$$\begin{bmatrix} 1 & 1/2 & 3 & 3 & 1/3 & 1/4 \\ 2 & 1 & 2 & 2 & 1/3 & 1/3 \\ 1/3 & 1/2 & 1 & 1 & 1/5 & 1/5 \\ 1/3 & 1/2 & 1 & 1 & 1/5 & 1/5 \\ 3 & 3 & 5 & 5 & 1 & 1/2 \\ 4 & 3 & 5 & 5 & 2 & 1 \end{bmatrix}$$

(d) Instrumentation

$$\begin{bmatrix} 1 & 2 & 4 & 3 & 9 & 9 \\ 1/2 & 1/4 & 3 & 3 & 9 & 9 \\ 1/4 & 1/3 & 1 & 1/2 & 8 & 8 \\ 1/3 & 1/3 & 2 & 1 & 9 & 9 \\ 1/9 & 1/9 & 1/8 & 1/9 & 1 & 1 \\ 1/9 & 1/9 & 1/8 & 1/9 & 1 & 1 \end{bmatrix}$$

(e) Structurally adaptable

$$\begin{bmatrix} 1 & 1/2 & 1/4 & 1/5 & 1/8 & 1/7 \\ 2 & 1 & 1/3 & 1/4 & 1/7 & 1/6 \\ 4 & 3 & 1 & 1/2 & 1/6 & 1/5 \\ 5 & 4 & 2 & 1 & 1/5 & 1/4 \\ 8 & 7 & 6 & 5 & 1 & 1/2 \\ 7 & 6 & 5 & 4 & 2 & 1 \end{bmatrix}$$

(f) Innovative design

$$\begin{bmatrix} 1 & 4 & 8 & 8 & 5 & 4 \\ 1/4 & 1 & 5 & 5 & 4 & 3 \\ 1/8 & 1/5 & 1 & 1/2 & 1/3 & 1/5 \\ 1/8 & 1/5 & 2 & 1 & 1/2 & 1/3 \\ 1/5 & 1/4 & 3 & 2 & 1 & 1/2 \\ 1/4 & 1/3 & 5 & 3 & 2 & 1 \end{bmatrix}$$

(g) Cost

$$\begin{bmatrix} 1 & 3 & 3 & 3 & 8 & 7 \\ 1/3 & 1 & 1 & 1 & 7 & 6 \\ 1/3 & 1 & 1 & 1 & 6 & 5 \\ 1/3 & 1 & 1 & 1 & 6 & 5 \\ 1/8 & 1/7 & 1/6 & 1/6 & 1 & 1/2 \\ 1/7 & 1/6 & 1/5 & 1/5 & 2 & 1 \end{bmatrix}$$

(h) Wind tunnel attachment

$$\begin{bmatrix} 1 & 1 & 1/2 & 1/2 & 1/2 & 7 \\ 1 & 1 & 1/2 & 1/2 & 1/2 & 7 \\ 2 & 2 & 1 & 1 & 1/3 & 5 \\ 2 & 2 & 1 & 1 & 1 & 8 \\ 2 & 2 & 3 & 1 & 1 & 7 \\ 1/7 & 1/7 & 1/5 & 1/8 & 1/7 & 1 \end{bmatrix}$$

(i) Support versatility

$$\begin{bmatrix} 1 & 1/5 & 1/6 & 1/5 & 1/2 & 1/4 \\ 5 & 1 & 1/2 & 1 & 4 & 3 \\ 6 & 2 & 1 & 2 & 4 & 3 \\ 5 & 1 & 1/2 & 1 & 3 & 2 \\ 2 & 1/4 & 1/4 & 1/3 & 1 & 1/3 \\ 4 & 1/3 & 1/3 & 1/2 & 3 & 1 \end{bmatrix}$$

(j) Measurement accuracy

$$\begin{bmatrix} 1 & 1/6 & 1/7 & 1/7 & 1/2 & 1 \\ 6 & 1 & 1/2 & 1/2 & 3 & 2 \\ 7 & 2 & 1 & 1 & 3 & 2 \\ 7 & 2 & 1 & 1 & 3 & 2 \\ 2 & 1/3 & 1/3 & 1/3 & 1 & 1 \\ 1 & 1/2 & 1/2 & 1/2 & 1 & 1 \end{bmatrix}$$

(k) Force and moment decoupling

$$\begin{bmatrix} 1 & 1/2 & 1/2 & 3 & 1 & 1 \\ 2 & 1 & 1 & 4 & 2 & 2 \\ 2 & 1 & 1 & 3 & 2 & 2 \\ 5 & 1/5 & 1/4 & 1 & 1/2 & 1/2 \\ 1 & 1/2 & 1/2 & 2 & 1 & 1 \\ 1 & 1/2 & 1/2 & 2 & 1 & 1 \end{bmatrix}$$

(l) Results processing

Figure B.1: Criteria evaluation

After having obtained all the criterion comparison matrices and tanking into consideration the information provided by the criteria pairwise comparison (table 3.12), it is possible to come up with a final rating for each of the designs that results in the criteria assessment, as represented in table B.1

Table B.1: Force balance types scores

	A	B	C	D	E	F	G	H	I	J	K	L	Total
Platform	0,0014	0,0119	0,0274	0,0051	0,0263	0,0005	0,0507	0,0457	0,0121	0,0087	0,0015	0,0255	0,2167
Rotating-platform	0,0025	0,0037	0,0153	0,0056	0,0165	0,0007	0,0258	0,0208	0,0121	0,0493	0,0056	0,0468	0,2048
Pyramidal	0,0122	0,0009	0,0032	0,0025	0,0091	0,0013	0,0039	0,0194	0,0174	0,0720	0,0080	0,0448	0,1947
Pyramidal-platform	0,0058	0,0017	0,0056	0,0025	0,0120	0,0019	0,0057	0,0194	0,0216	0,0433	0,0080	0,0230	0,1504
Innovative 1	0,0030	0,0044	0,0028	0,0123	0,0018	0,0048	0,0093	0,0035	0,0261	0,0142	0,0025	0,0234	0,1082
Innovative 2	0,0071	0,0083	0,0103	0,0163	0,0018	0,0054	0,0149	0,0049	0,0026	0,0273	0,0029	0,0234	0,1253

Appendix C

Stewart Platform Quality Index (λ) Evaluation

Table C.1 represents the variation on the *Stewart* platform quality index when several dimensional parameters are changed.

Table C.1: Quality index evaluation for different *Stewart* platform properties

a [mm]	b [mm]	α	β	$a\alpha$ [mm]	$b\beta$ [mm]	h [mm]	Quality index (λ)
400	600	0.167	0.167	66.67	100	500	**0.22**
400	600	0.167	0.167	66.67	100	350	**0.47**
400	700	0.167	0.167	66.67	116.67	350	**0.65**
350	700	0.180	0.167	63	116.67	300	**0.83**
350	700	0.180	0.100	63	70	300	**0.96**
350	700	0.171	0.006	60	45	300	**0.99**

It is possible to observe that decreasing the height (h) between platforms while keeping the remaining properties constant, increases the quality index. Moreover, diminishing α and β parameters results in increasing the quality index. The last row represents the properties of the selected *Stewart* platform to use as the force balance main structure.

Appendix D

Structural Analysis

Similarly to what was done to the full plane model, a detailed stress and displacement analysis had to be carried out for the case of the half wing models, considering the forces and moments range found previously and the admissible angular displacement, as represented in table D.1.

Table D.1: Maximum expected range of loads and allowable angular displacements

F_X [N]	F_Y [N]	F_Z [N]	M_X [Nm]	M_Y [Nm]	M_Z [Nm]	θ_Z	θ_Y
213	1171	45	585	115	60	0.5°	0.5°

The obtained results for stress and maximum tangential displacement at the tip of the strut are represented in figures D.1(a) and D.1(b), respectively.

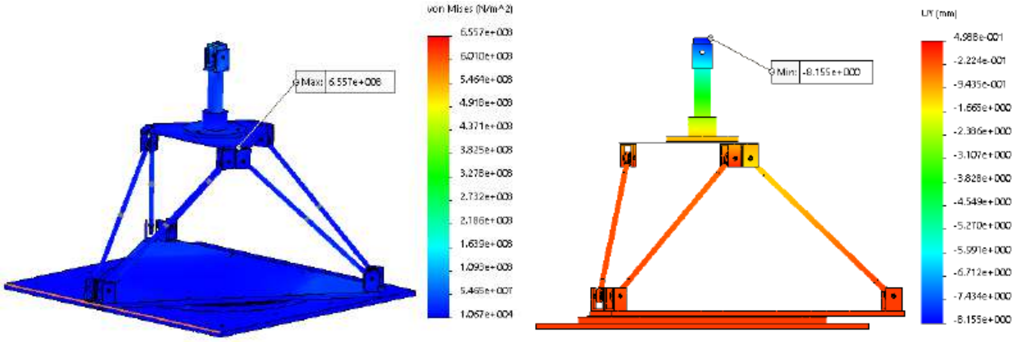

(a) Stress distribution

(b) Maximum tangential displacement

Figure D.1: Half wing model configuration

Strut & Flange

The range of stresses for the strut and the flange are represented in figures D.2(a) and D.2(b), respectively and, as can be seen, the maximum values of stress occur in the contact region between these two components where the load transferring happens.

Table D.2 compares the maximum values of stress in both components with the yield strength of the materials and, as can be seen, the former are lower than the latter and so, yielding does not occur.

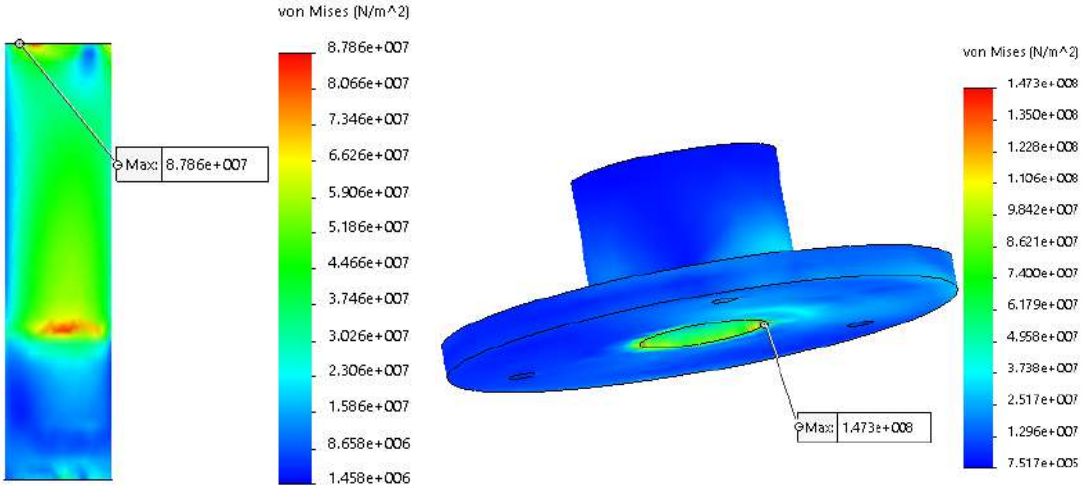

(a) Strut

(b) Flange

Figure D.2: Stress distribution in the model support components

Table D.2: Maximum stress at the strut and the flange

	Material	σ_{max} [MPa]	σ_Y [MPa]
Strut	Al 6063-T6	88	215
Flange	Al 6063-T6	147	215

Fixed platform

Stress distribution in the fixed platform is represented in figure D.3 and the respective maximum value is highlighted. The yield stress of the material (Structural Steel 1.0037) is $235MPa$ which is greater than the maximum value in the structure ($109MPa$).

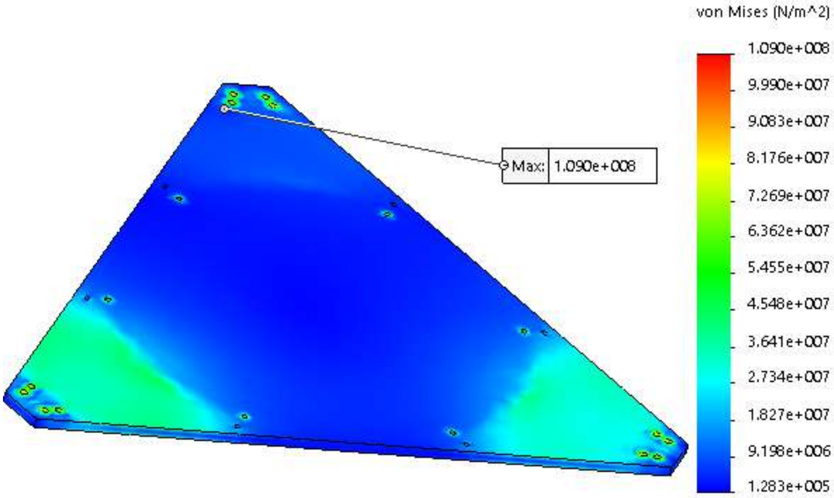

Figure D.3: Stress distribution in the fixed platform

Sensing bars

Figures D.4(a) and D.4(b) represent, respectively, the axial stress and displacement distribution along the bar. The yield strength of the material (Al 6061-T6 - σ_Y=275 MPa) is greater than the maximum stress value in the bar ($69MPa$) and so, yielding does not occur.

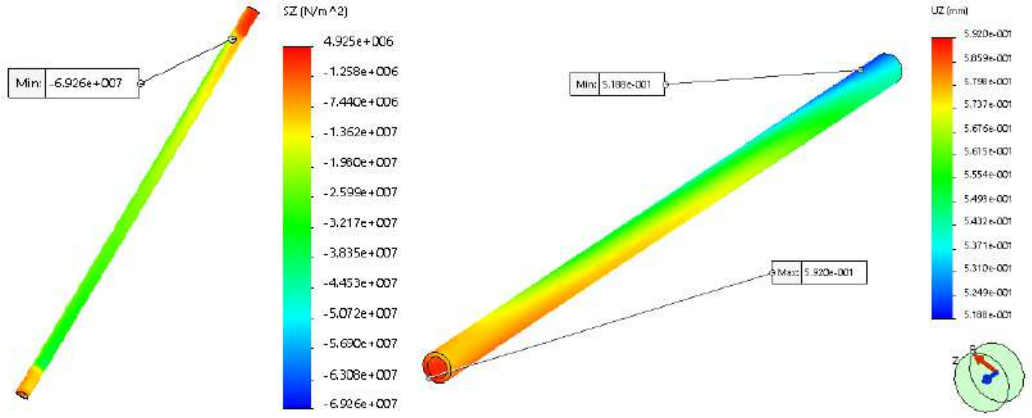

(a) Axial stress distribution

(b) Axial displacement

Figure D.4: Sensing bar analysis

This maximum value ($31MPa$) allows one to obtain the maximum expected axial stress, as represented in table D.3.

Table D.3: Maximum axial stress at the bars

σ_{max} [Pa]	External diameter $[m]$	Internal diameter $[m]$	Area $[m^2]$	Axial Force $[N]$
6.926×10^7	0.010	0.007	1.60×10^{-4}	11097

Rod end bearing

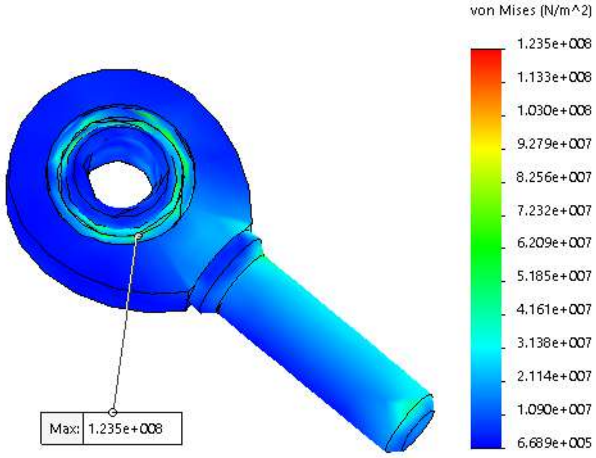

Figure D.5: Stress distribution along the rod end bearing

The rod end bearings must be able to carry the maximum expected axial loads at the sensing bars. In this case, they present the capability to support a maximum axial load of $12900N$ which is above the maximum expected value $(11097N)$.

In terms of stress values, figure D.5 shows its distribution throughout the rod end bearing that presents the maximum value of stress that occurs near the housing region.

Moving platform

Figure D.6 represents the stress distribution in the upper platform. The maximum stress value occurs near the region of contact with the couplers, where the loads are transferred.

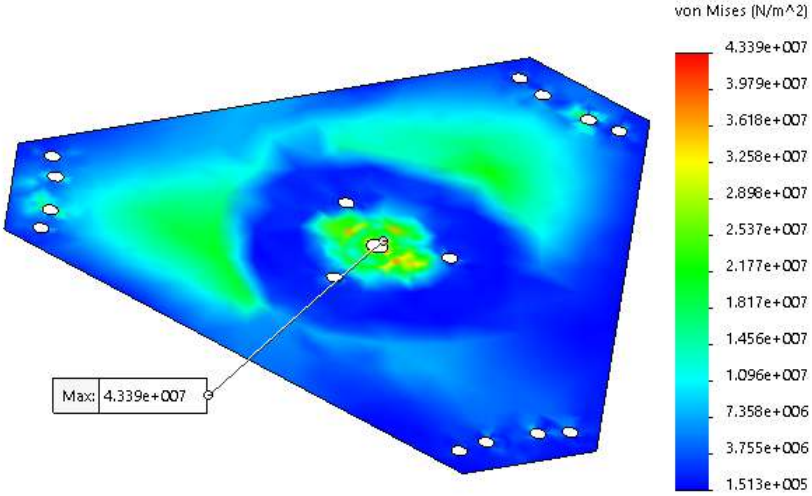

Figure D.6: Stress distribution in the upper platform

Coupler

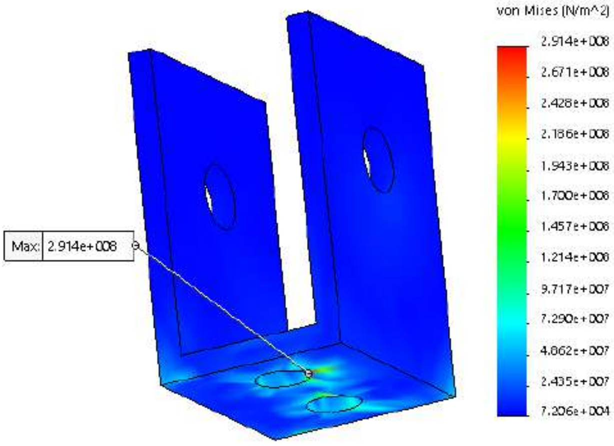

Figure D.7: Stress distribution in the coupler mechanism

Figure D.7 shows the stress distribution for the coupler units. As referred before, the maximum values of stress occur in the region of contact between the couplers and the upper platform near the holes. The maximum stress value ($291MPa$) is below the yield strength of the material (Alloy Steel - $620MPa$).

β adjustment: rotating platform

Stress distribution in the rotating platform and the table is represented in figure D.8. The maximum stress value ($127MPa$) is below the yield strength values of the table and the rotary collar that are $235MPa$ and $325MPa$, respectively.

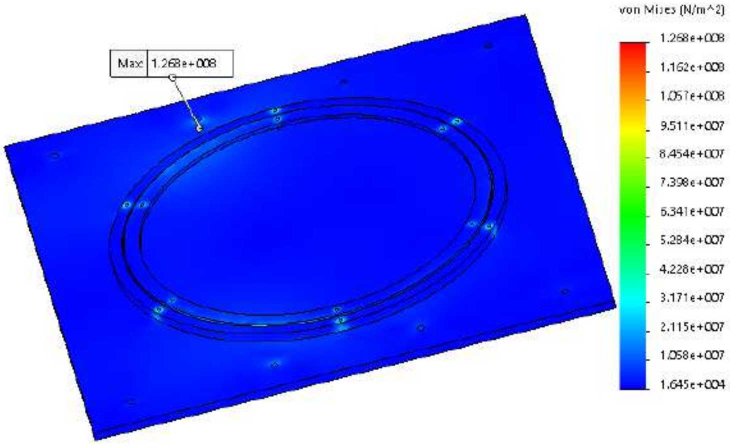

Figure D.8: Stress distribution in the table and rotating collar

α adjustment mechanism

Figure D.9 represents the stress distribution throughout the whole mechanism used to control de angle of attack. The maximum value of stress ($154MPa$) is below the yield strength of the considered aluminium alloy (Al 2024-T4) which presents a yield strength of $325MPa$.

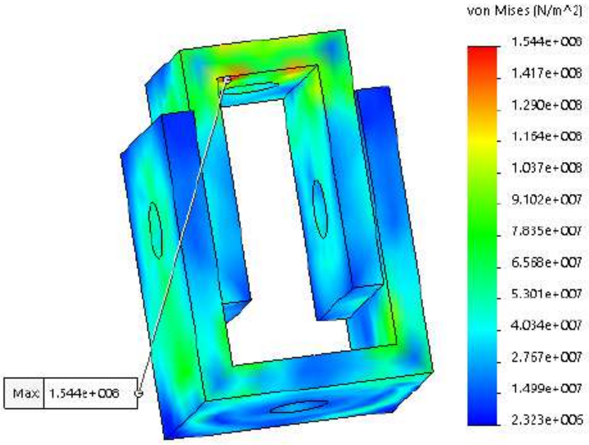

Figure D.9: Stress distribution in the angle of attack adjustment mechanism

Appendix E

Technical Drawings

In this appendix, several pages with technical drawings of the mechanical components that were designed will be presented.

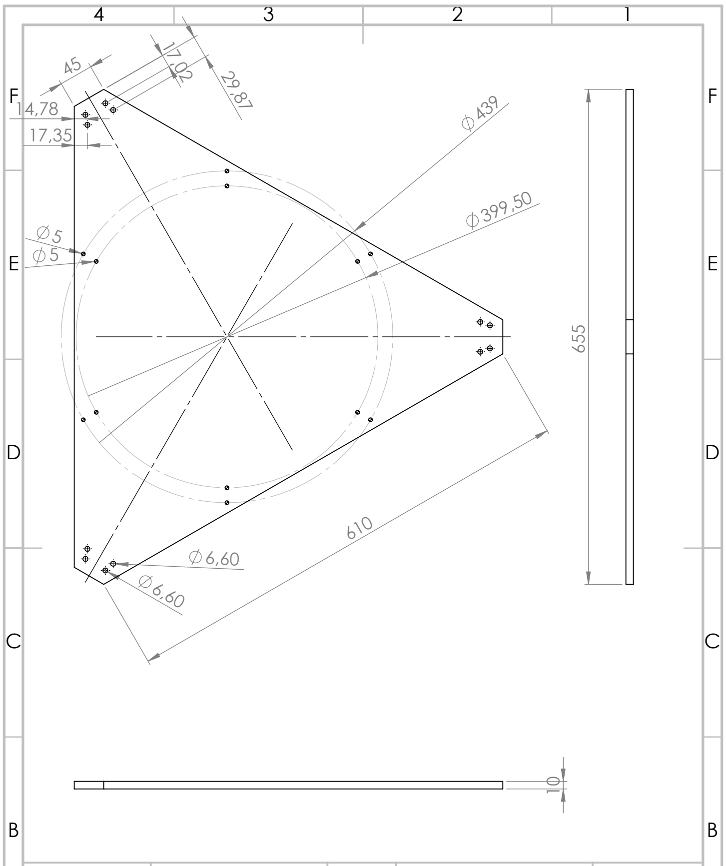

UNLESS OTHERWISE SPECIFIED:
DIMENSIONS ARE IN MILLIMETERS
SURFACE FINISH:
TOLERANCES:
LINEAR:
ANGULAR:

FINISH:

DEBURR AND
BREAK SHARP
EDGES

DO NOT SCALE DRAWING

REVISION

	NAME	SIGNATURE	DATE
DRAWN	João Fernandes		13/05/2018
CHK'D			
APPV'D			
MFG			
Q.A			

TITLE:
FixedPlatform

MATERIAL:
Steel

DWG NO.
1

A4

WEIGHT:

SCALE:1:5

SHEET 1 OF 1

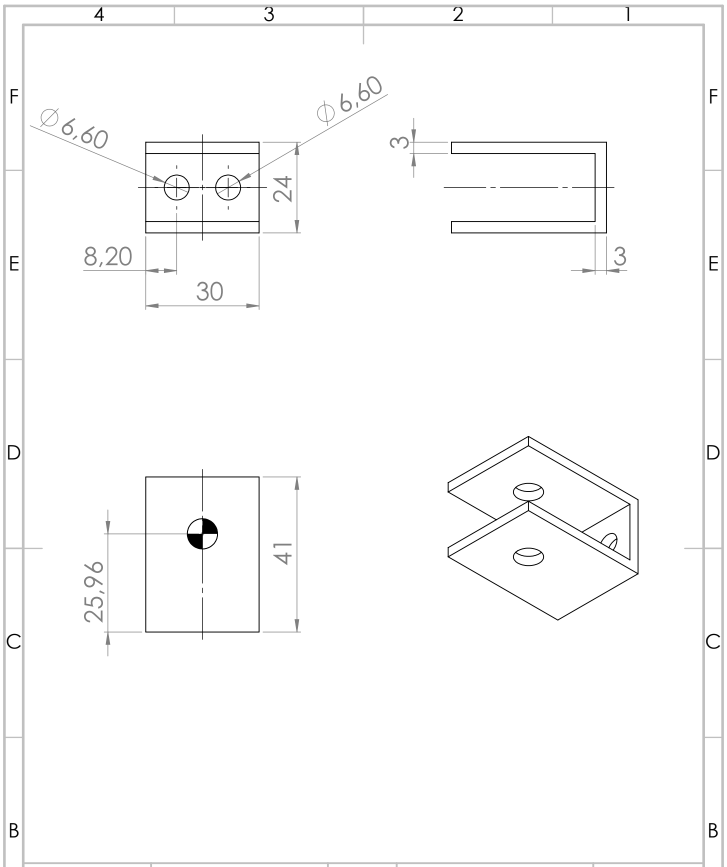

UNLESS OTHERWISE SPECIFIED:
DIMENSIONS ARE IN MILLIMETERS
SURFACE FINISH:
TOLERANCES:
LINEAR:
ANGULAR:

FINISH:

DEBURR AND
BREAK SHARP
EDGES

DO NOT SCALE DRAWING

REVISION

	NAME	SIGNATURE	DATE
DRAWN	João Fernandes		13/05/2018
CHK'D			
APPV'D			
MFG			
Q.A			

TITLE:
Coupler

MATERIAL:
Steel

DWG NO.
2

A4

WEIGHT:

SCALE:1:1

SHEET 1 OF 1

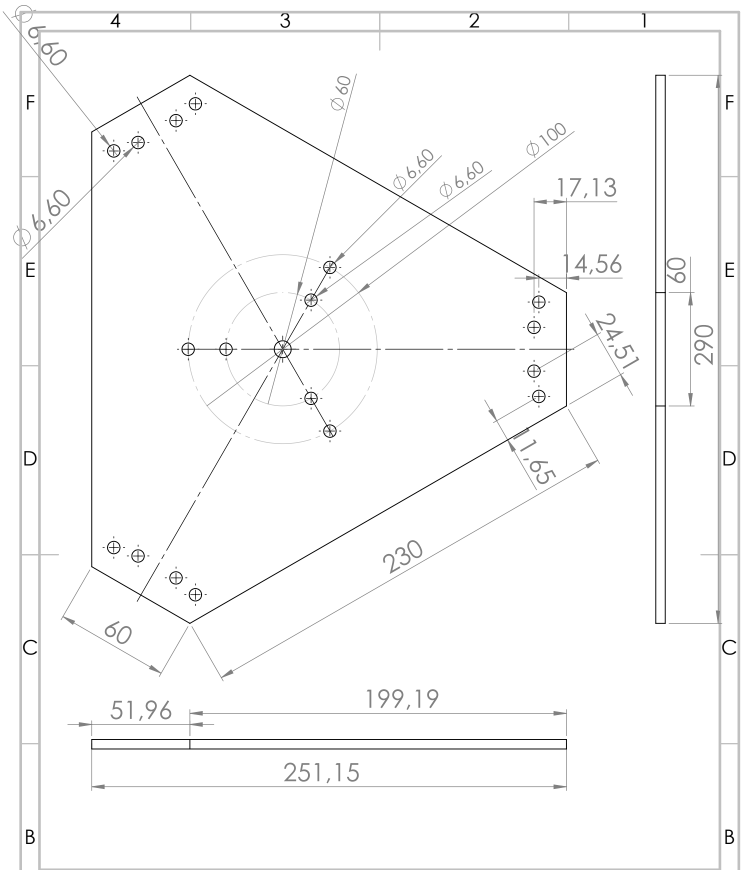

UNLESS OTHERWISE SPECIFIED:
DIMENSIONS ARE IN MILLIMETERS
SURFACE FINISH:
TOLERANCES:
LINEAR:
ANGULAR:

FINISH:

DEBURR AND
BREAK SHARP
EDGES

DO NOT SCALE DRAWING

REVISION

	NAME	SIGNATURE	DATE
DRAWN	João Fernandes		13/05/2018
CHK'D			
APPV'D			
MFG			
Q.A			

TITLE:
MovingPlatform

MATERIAL:
Composite plate

DWG NO.
4

A4

WEIGHT:

SCALE:1:5

SHEET 1 OF 1

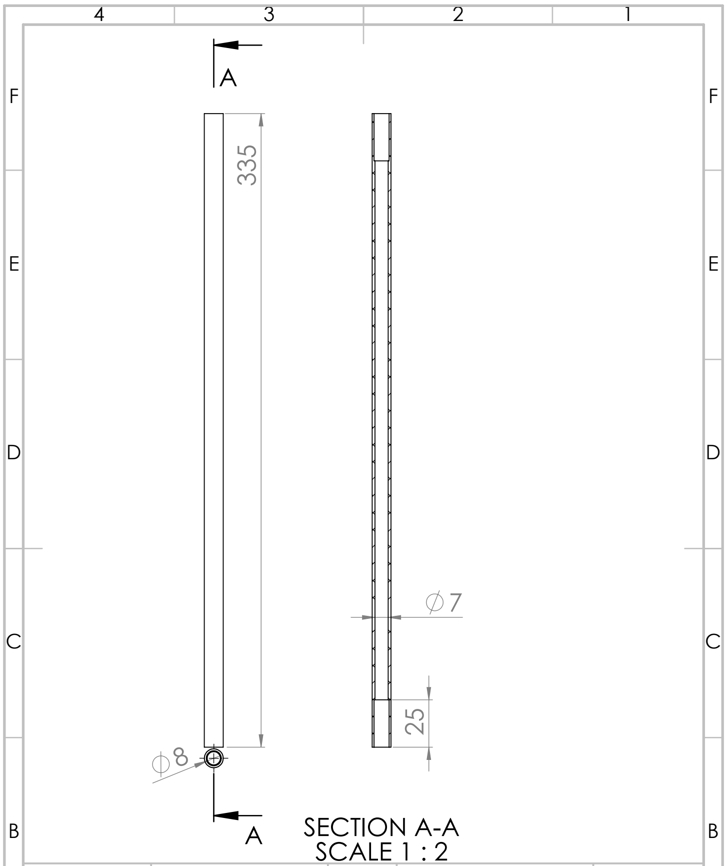

UNLESS OTHERWISE SPECIFIED:
DIMENSIONS ARE IN MILLIMETERS
SURFACE FINISH:
TOLERANCES:
LINEAR:
ANGULAR:

FINISH:

DEBURR AND
BREAK SHARP
EDGES

DO NOT SCALE DRAWING

REVISION

	NAME	SIGNATURE	DATE
DRAWN	João Fernandes		13/05/2018
CHK'D			
APPV'D			
MFG			
Q.A			

TITLE:
SensingBar

MATERIAL:

DWG NO.
6

A4

WEIGHT:

SCALE:1:5

SHEET 1 OF 1

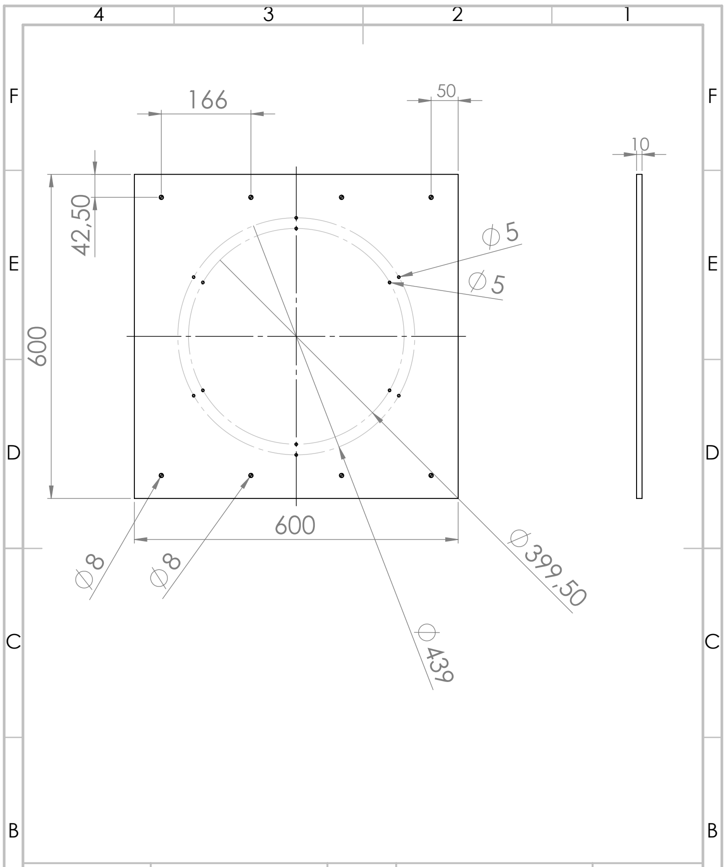

UNLESS OTHERWISE SPECIFIED:
DIMENSIONS ARE IN MILLIMETERS
SURFACE FINISH:
TOLERANCES:
LINEAR:
ANGULAR:

FINISH:

DEBURR AND BREAK SHARP EDGES

DO NOT SCALE DRAWING

REVISION

	NAME	SIGNATURE	DATE
DRAWN	João Fernandes		13/05/2018
CHK'D			
APPV'D			
MFG			
Q.A			

TITLE:
Table

MATERIAL:
Steel

DWG NO.
8

A4

WEIGHT:

SCALE:1:10

SHEET 1 OF 1

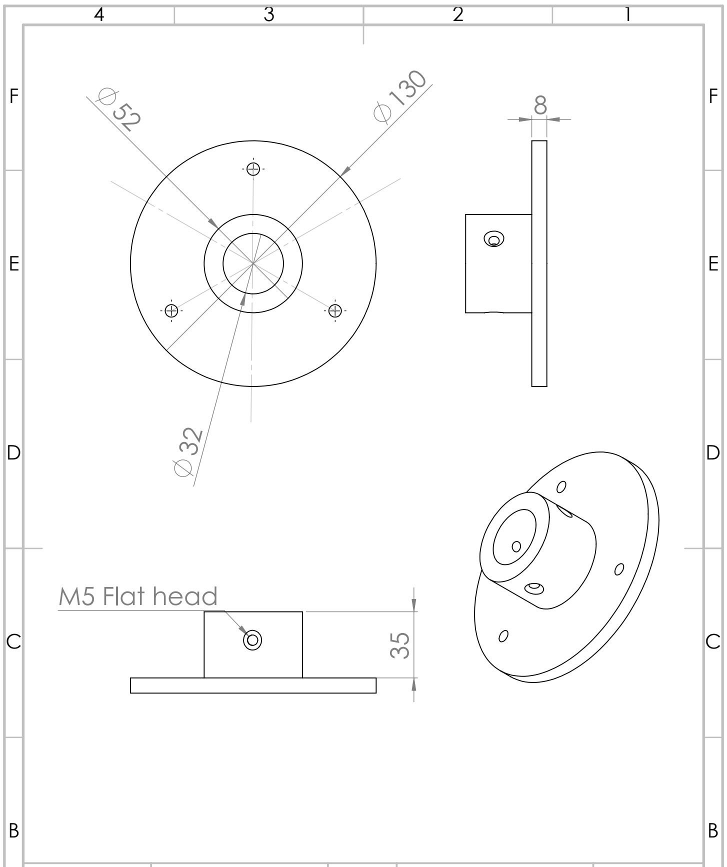

UNLESS OTHERWISE SPECIFIED:
DIMENSIONS ARE IN MILLIMETERS
SURFACE FINISH:
TOLERANCES:
LINEAR:
ANGULAR:

FINISH:

DEBURR AND BREAK SHARP EDGES

DO NOT SCALE DRAWING

REVISION

	NAME	SIGNATURE	DATE
DRAWN	João Fernandes		13/05/2018
CHK'D			
APPV'D			
MFG			
Q.A			

TITLE:
Flange

MATERIAL:
Aluminium

DWG NO.
9

A4

WEIGHT:

SCALE:1:2

SHEET 1 OF 1

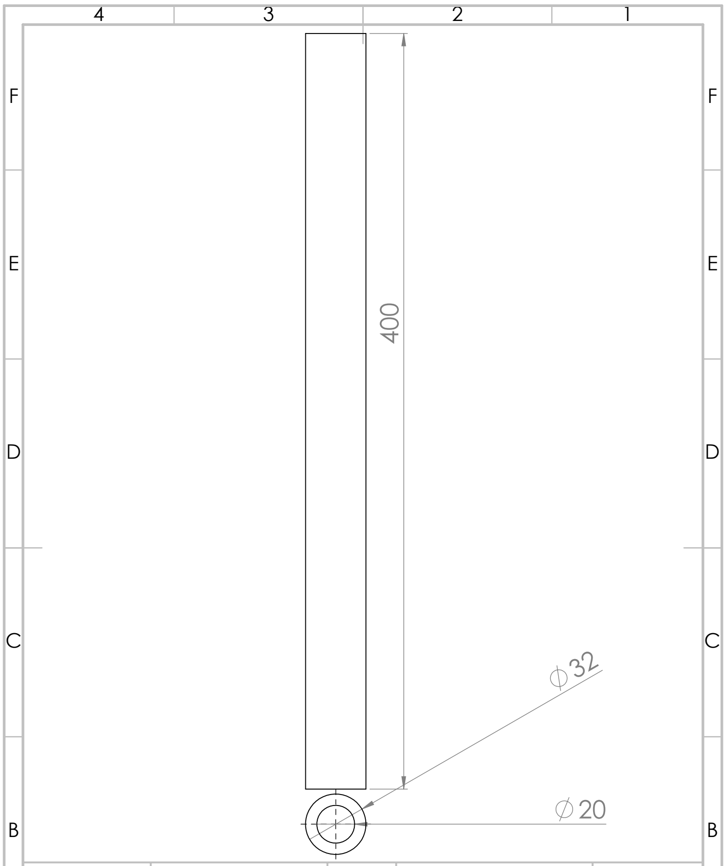

UNLESS OTHERWISE SPECIFIED:
DIMENSIONS ARE IN MILLIMETERS
SURFACE FINISH:
TOLERANCES:
LINEAR:
ANGULAR:

FINISH:

DEBURR AND BREAK SHARP EDGES

DO NOT SCALE DRAWING

REVISION

	NAME	SIGNATURE	DATE
DRAWN	João Fernandes		13/05/2018
CHK'D			
APPV'D			
MFG			
Q.A			

TITLE:
Strut(aircraft)

MATERIAL:

DWG NO.
10

A4

WEIGHT:

SCALE:1:5

SHEET 1 OF 1

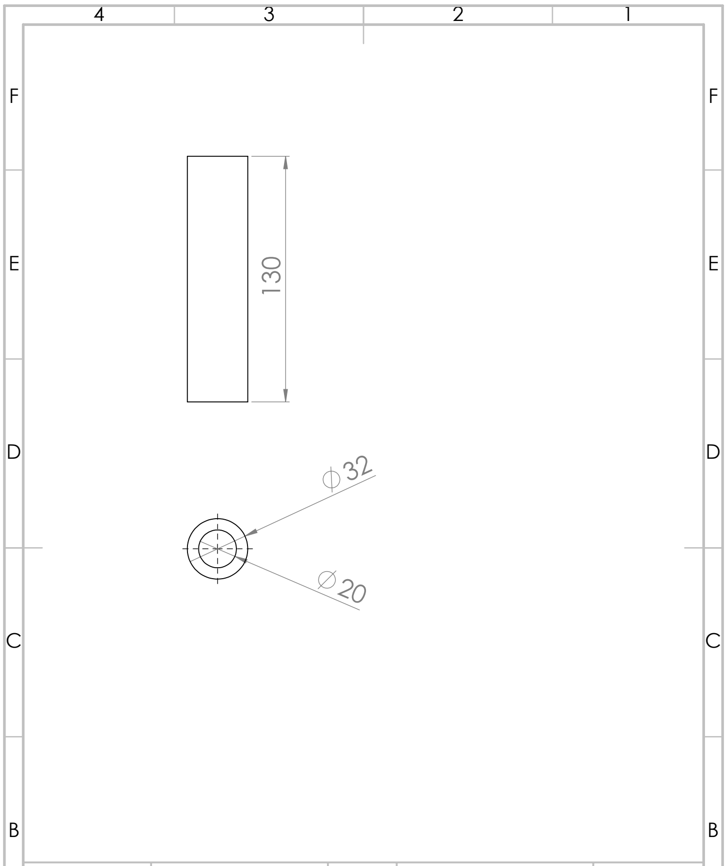

UNLESS OTHERWISE SPECIFIED:
DIMENSIONS ARE IN MILLIMETERS
SURFACE FINISH:
TOLERANCES:
LINEAR:
ANGULAR:

FINISH:

DEBURR AND BREAK SHARP EDGES

DO NOT SCALE DRAWING

REVISION

	NAME	SIGNATURE	DATE
DRAWN	João Fernandes		13/05/2018
CHK'D			
APPV'D			
MFG			
Q.A			

TITLE:
Strut(half-wing)

MATERIAL:
Aluminium

DWG NO.
10

A4

WEIGHT:

SCALE:1:2

SHEET 1 OF 1

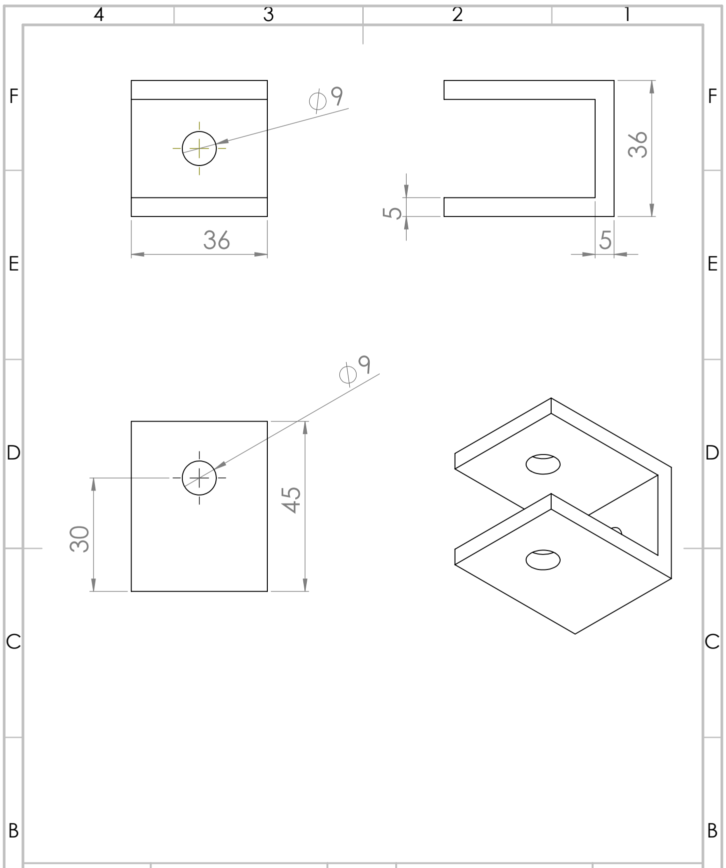

UNLESS OTHERWISE SPECIFIED:
DIMENSIONS ARE IN MILLIMETERS
SURFACE FINISH:
TOLERANCES:
LINEAR:
ANGULAR:

FINISH:

DEBURR AND
BREAK SHARP
EDGES

DO NOT SCALE DRAWING

REVISION

	NAME	SIGNATURE	DATE
DRAWN	João Fernandes		13/05/2018
CHK'D			
APPV'D			
MFG			
Q.A			

TITLE:
alphaAdjustment_1

MATERIAL:
Aluminium

DWG NO.
11

A4

WEIGHT:

SCALE:1:1

SHEET 1 OF 1

A

4 3 2 1

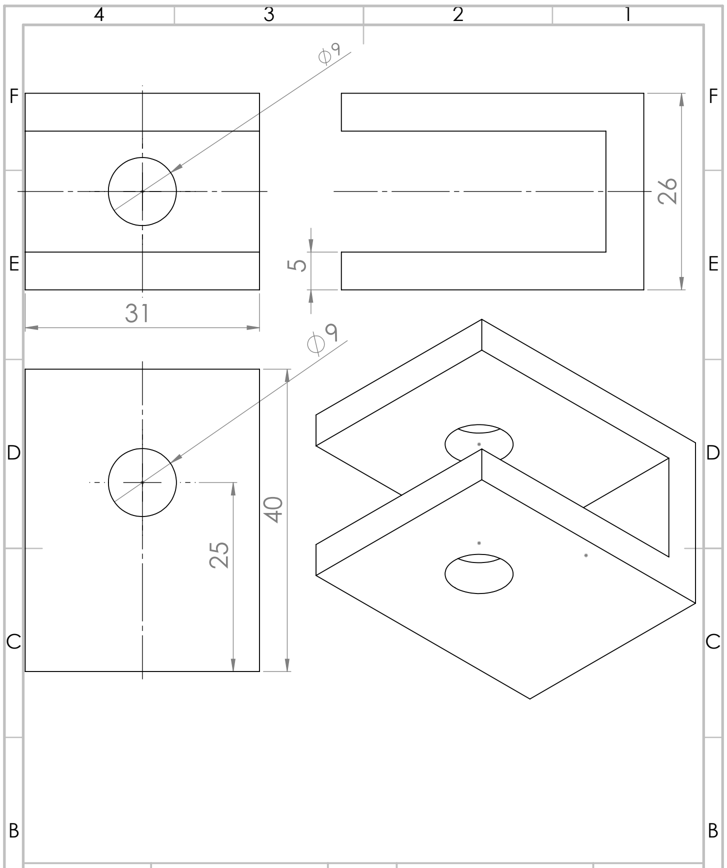

UNLESS OTHERWISE SPECIFIED:
DIMENSIONS ARE IN MILLIMETERS
SURFACE FINISH:
TOLERANCES:
LINEAR:
ANGULAR:

FINISH:

DEBURR AND
BREAK SHARP
EDGES

DO NOT SCALE DRAWING

REVISION

	NAME	SIGNATURE	DATE
DRAWN	João Fernandes		13/05/2018
CHK'D			
APPV'D			
MFG			
Q.A			

TITLE:
alphaAdjustment_2

MATERIAL:
Aluminium

DWG NO.
12

A4

WEIGHT:

SCALE:2:1

SHEET 1 OF 1

A

4 3 2 1